People’s and Democratic Republic of Algeria
Ministry of Higher Education and
Scientific Research
University M’Hamed BOUGARA – Boumerdes
Faculty of Engineering

Department of Electronics and Electrical Engineering

Report Presented in Partial Fulfilment of the Requirement

of the Degree of

Magister

In Electronics

Option: *Telecommunication*

Title:

Analysis of Small Microstrip Patch Antennas for Mobile Communication

By:

MOUHOUCHE Faïza

Examiner Board:

AKSAS Rabia	Professeur, ENP	Président
AZRAR Arab	Maître de Conférences / A, UMBB	Rapporteur
TRABELSI Mohamed	Professeur, ENP	Membre
NOURREDDINE Mohamed	Professeur, UMBB	Membre
DAHIMENE Abdelhakim	Maître de Conférences / B, UMBB	Membre

Abstract

This work presents the analysis and design of small microstrip patch antennas that can be used in mobile communication using Finite Difference Time Domain (FDTD) method. The formulation of the FDTD algorithm is described along with its fundamental properties. At the beginning, the method is applied to the arbitrary shaped patch; and the radio-electric properties of the considered microstrip patch antennas are formulated. The method is then applied to some known structure shapes working in high microwave frequency bands; the shapes include rectangular (dipole), annular-ring and semi-ring patches. Different feeding methods (Microstrip line feed and coaxial line feed) are used to energize the considered antennas. The input impedance (VSWR), the return loss, and the far field radiation patterns calculated with the aid of FDTD method and compared with the results obtained with the HFSS simulator.

Due to the nature of the chosen method, a new shape of patch is designed and analyzed. The new structure is named Berber-Z patch antenna taken from "TIFINAGH" Berber alphabet. The obtained results are Validated the HFSS simulator.

تصميم وتحليل هوائيات الشرائح الصغيرة للاتصالات المتنقلة

ملخص

هذا العمل يقدم تحليلا وتصميم هوائيات الشرائح الصغيرة التي يمكن استخدامها في الاتصالات المتنقلة باستخدام طريقة محدود فارق التوقيت المجال (FDTD). ويرد وصف لصياغة الخوارزمية (FDTD) مع خصائصه الأساسية. في البداية ، يتم تطبيق الطريقة لشرائح ذات ا شكال تعسفية ، وخصائص الراديو والكهرباء لشرائح الهوائيات الصغيرة. ثم يتم تطبيق هذه الطريقة على بعض الأشكال المعروفة هيكل العاملة في نطاقات التردد العالي الميكروويف ، وتشمل الشرائح الشكل المستطيل (ثنائي القطب) ، حلقية الدائري و نصف حلقية الدائري. وتستخدم أساليب مختلفة للتغذية و لتفعيل هوائيات (Microstrip سطر تغذية ومحوري خط تغذية) . مقاومة الإدخال (VSWR) ، وفقدان العودة ، والإشعاع مجال أنماط تحسب بمساعدة طريقة(FDTD) الأسلوب وبالمقارنة مع النتائج التي تم الحصول عليها باستخدام برنامج متطوريسمى محاكي التصميمات عالية التردد(HFSS).

ونظرا لطبيعة الطريقة المختارة، شكل جديد من الشرائح الهوائيات الصغيرات تم تصميمها وتحليلها. يدعى الهيكل الجديد البربرية التي اتخذت من "تيفيناغ الأبجدية البربرية"(البربر-Z). يتم التحقق من صحة النتائج التي تم الحصول عليها من جهاز(HFSS).

Résumé

Ce travail présente l'analyse et la conception de petites antennes micro-ruban patch qui peut être utilisé dans la communication mobile à l'aide 'Finite Difference Time Domain' (FDTD) méthode. La formulation de l'algorithme FDTD est décrite avec ses propriétés fondamentales. Au début, la méthode est appliquée à la pièce en forme arbitraire, et les propriétés radioélectriques de la micro-ruban antennes patch considérée sont formulées. La méthode est ensuite appliquée à une structure connue des formes de travail dans les bandes de fréquence micro-ondes de haute; les formes sont rectangulaires (dipôle), annulaires cycliques et le correctif semi-anneau. Différentes méthodes d'alimentation (ligne micro-ruban et ligne coaxiale) sont utilisées pour alimenter les antennes en considération. L'impédance d'entrée (VSWR), la perte de retour, et les modèles jusqu'à un champ de rayonnement calculées à l'aide de la méthode FDTD et comparés avec les résultats obtenus avec le simulateur HFSS.

En raison de la nature de la méthode choisie, une nouvelle forme de patch est conçue et analysé. La nouvelle structure porte le nom berbère antenne patch-Z extrait de "Tifinagh" alphabet berbère. Les résultats obtenus sont validés le simulateur HFSS.

Acknowledgements

I would like to thank everybody who has helped me during my graduate school years and while I was working on my report.

I would like to express my sincere gratitude to Dr. AZRAR Arab, my work advisor, for his support and guidance during my graduate studies, research work and report preparation. This thesis would not have been possible without his continuous help. I also express my gratitude to Mr. DEHMAS for his help and assistance for the accomplishment of this work. By the opportunity, I would like to express my sympathy to my colleagues and friends of the department of electrical and electronics (DGEE, university of Boumerdès).

My warmest thanks go to my parents they were also very important to me in this entire process. They always stood behind me and encouraged me to follow my interests. They made me feel that no matter what the outcome of this process, their love for me would never change.

I am also forever grateful to my husband, for his invaluable patience, understanding and whose support I, could not have done this without his. I dedicate this work to them.

Table of contents

Chapter I: Generalities

Chapter II: concepts and mathematical formulation

Chapter III: Numerical results and discussion

List of figures

Aucune entrée de table des matières n'a été trouvée.

Introduction

Often described as one of the most exciting developments in antenna and electromagnetic history, the microstrip patch antenna has matured into probably the most versatile solutions to many systems requiring a radiating element. The microstrip antenna is a very good common element in telecommunication and radar applications since it provides a wide variety of designs, can be planar or conformal, and can be fed in many different methods [1], [2]. Currently, the use of microstrip antennas has grown due to the advantages of these kinds of structures. It is well known that microstrip antennas have several shapes and can perform in different ways, depending on the application.

Several mobile communication handset terminals today use variants of the microstrip patch antenna (MSA) as their radiator. Because of its characteristics; low profile, small size, low cost, and conformability to mounting hosts , MSAs are very promising candidates for satisfying this design consideration. There are various shapes of patch antennas meeting those requirements (low cost and low profile) for examples annular-ring, rectangular, semi-ring and Berber-Z (Z in "*TIFINAGH*" writing). Feeding mechanism plays an important role in the design of microstrip patch antennas.

The microstrip patch is a relatively complicated radiator. Over the years there have been several analytical /numerical methods proposed and used to analyze this radiator. The Finite Difference Time Domain (FDTD) method is one of the full wave methods that are used in the analysis of microstrip antennas. FDTD has been widely used to simulate various electromagnetic Problems (with complex geometry) because of its flexibility and versatility.

This work presents the analysis and design of microstrip patch antenna using the Finite-Difference Time-Domain (FDTD) method. The FDTD method principle is described in some detail that allows an understanding of the way of applying the algorithms to microstrip structure. At the beginning, the method is applied to the arbitrary shaped patch; and the radio-electric properties of microstrip patch antennas are formulated. The method is then applied to some known structure shapes working in high microwave frequency bands, the shapes include, rectangular (dipole), annular-ring and semi-ring patches.

Due to the nature of the chosen method, a new shape of patch is composed, designed and analyzed. The new structure is named Berber-Z patch antenna having the shape of the letter corresponding to the consonant ‘Z’ in *Tamazight* language alphabet written using the *Tifinagh* transcription. The obtained results are compared with simulated by High Frequency Structure Simulator (HFSS) simulator, the report consists of three chapters organized as follows:

Chapter 1,in which we present an overview of microstrip patch antenna and its characteristics, the different feeding/excitation methods, method of analysis of microstrip antennas, a brief description of FDTD method and its advantages over other methods and an overview of HFSS simulator that is used to compare the obtained results.

In chapter 2, the main theoretical concepts and formulas of FDTD method are used to analyze the different shapes of microstrip antennas. Provides some fundamental concepts of FDTD and introduces the Yee's FDTD (Maxwell’s curl equations) formulation and its implementation in microstrip antenna. The absorbing boundary conditions (ABCs), formulation of Mur’s absorbing boundary condition, excitation source, Antenna Feed Models and the near field to far field transformation.

Chapter three discusses the simulation steps and the design procedure of four shapes of microstrip patch antennas and, different feeding techniques using Finite Difference Time Domain (MATLAB program) and, compares the obtained results with HFSS simulator based on the Finite Element method (FEM). To get the physical characteristics of antennas (the return loss (S_{11}), gain, input impedance (VSWR) and far fields radiation patterns).

The work ends with a conclusion that summarizes the whole work; and some appendices.

Chapter I

Generalities

This chapter provides background description of microstrip patch antennas as well as some features of the numerical method used in this work.

1.1. Background

Microstrip Antennas (MSAs) was first introduced in the 1950's, and it became very popular in 1970's for space borne applications [1]. Since then, a massive amount of research and development efforts have been directed to them. Microstrip patch antennas have found widespread use due to many desirable features over other antenna structures, including their low profile and conformity to planar and non-planar surfaces, light weight, low cost production, robust nature; they can be designed to operate over a large range of frequencies (1-50GHz) [3]. Moreover, they can easily be combined to form linear or planar arrays, and they can generate linear, dual, and circular polarizations. These antennas are inexpensive to fabricate using printed circuit board etching, which makes them very useful for integrated active antennas in which circuit functions are integrated with the antenna to produce compact transceivers. They are also very versatile in terms of resonance frequency, polarization, radiation pattern and impedance. We can find MSAs on the surfaces of high-performance aircraft, spacecraft, satellites, missiles, cars and new held mobile telephone, where size, weight, cost, performance and ease of installation are important factors.

However, Microstrip patch antennas also have some limitations to conventional microwave antennas such as narrow bandwidth, relatively poor radiation efficiency resulting from surface wave excitation, conductor and dielectric losses and difficulty of prediction the performance of this form of radiator.

1.1.1. Microstrip antenna

A microstrip antenna is a resonant style radiator. It consists of a radiating patch on one side of a dielectric substrate which has a ground plane on the other side as shown in figure 1.1; microstrip antenna is referred to as **patch antenna.**

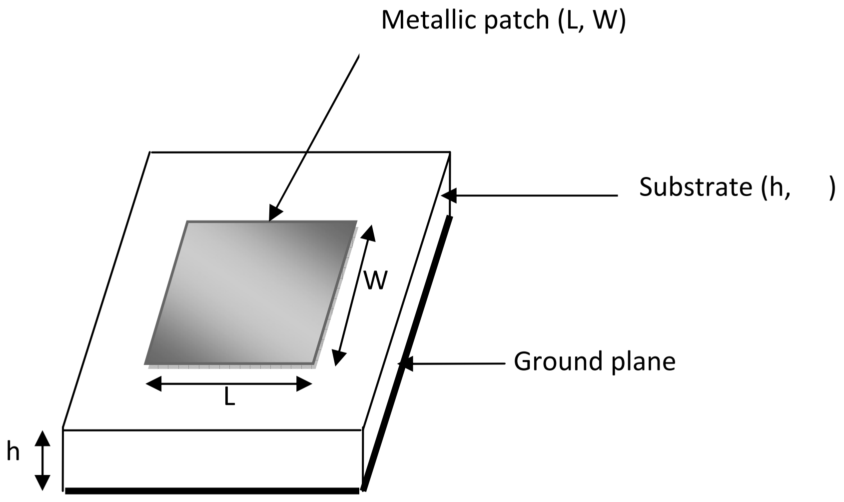

Fig. 1.1 Microstrip patch antenna configuration

The patch ger ld and it is the source of radiation where electromagnetic energy fringes off the edges of the patch and into the substrate. The length L of the patch is usually $0.333\lambda_0 \le L \le 0.5\lambda_0$ (λ_0 is the free space wavelength). The patch is selected to be very thin such that $t << \lambda_0$ (t is the patch thickness) [4].

The ground plane acts as a perfectly reflecting ground plane, bouncing energy back through the substrate and into free space.

The patch and the ground plane are separated by a dielectric sheet (referred to as the substrate). There are numerous substrates materials that can be used for the design of microstrip antennas and their dielectric constant is usually in the range $2.2 \le \varepsilon_r \le 12$ suitable for operation at frequencies ranging from 1 to 100 GHz [4].

Over the years there have been many conductor shapes proposed and investigated for a microstrip patch antenna, schematic diagrams of these are shown in the figure1.2.

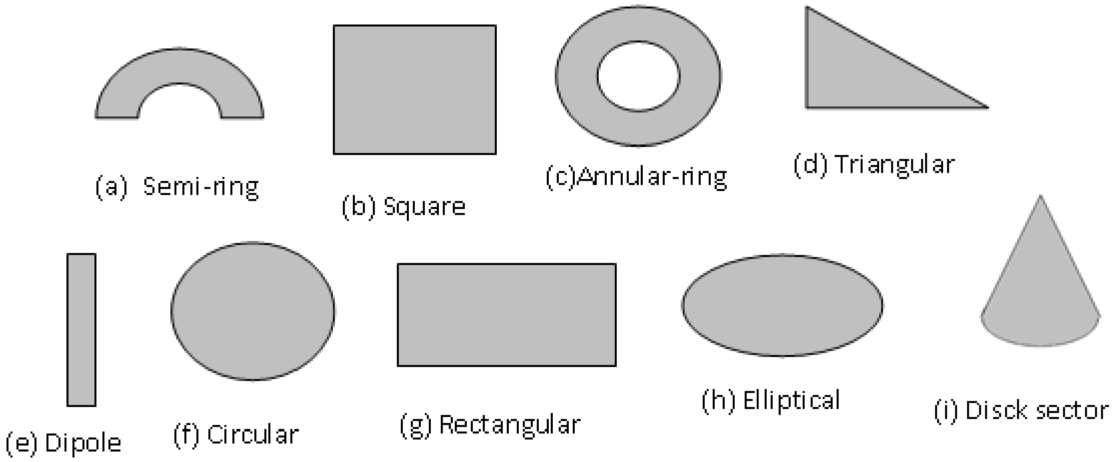

Fig. 1.2 Examples of conductor shapes for microstrip patches antennas [4]

1.1.2. Radiated Fields of Microstrip Antenna

The field structure within the substrate and between the radiating element and the ground plane is shown in figure 1.3 (a) and 1.3 (b). The electromagnetic wave traveling along the microstrip feed line spreads out under the patch. Hence, the resulting reflections at the open circuit set standing-wave pattern. From the figure 1.3(b), it can be clearly seen that the radiated fields undergo a phase reversal along the length of the structure, but is approximately uniform along the width of the structure.

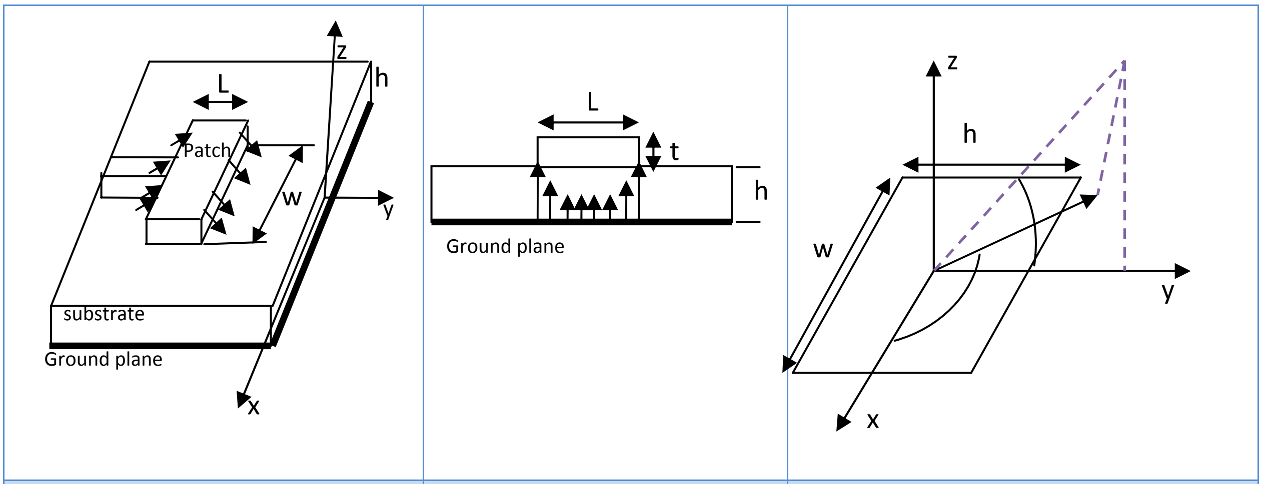

(a) Microstrip antenna

(b) Side view

(c) Coordinate system for aperture

Fig. 1.3 Microstrip antenna and coordinate system [5]

The antenna consists of two slots, separated by a very low impedance parallel-plate transmission line which acts as a transformer [5]. The length of the transmission line has to be approximately $\lambda_g/2$ (where λ_g is a guide wavelength) in order for the fields at the aperture of the two slots to have opposite polarization. The components of the field from each slot add in phase and provide a maximum radiation normal to the element. As for the electric field at the aperture of each slot, it can be categorized into x and y components, as shown in figure 1.3(c). The y components are out of phase and hence, their contributions will cancel out each other.

Due to the fact that the thickness of the microstrip is normally very small, the electromagnetic waves generated within the dielectric substrate (between the patch and the ground plane) undergo considerable reflections when they arrive at the edge of the strip. Hence, only a small fraction of the incident energy is radiated. As a result, the antenna is considered to be very inefficient and it behaves more like a cavity instead of a radiator.

1.1.3. Feeding techniques

There are many configurations that can be used to feed or transmit electromagnetic energy to microstrip antennas. The four most popular feed techniques used are; microstrip feed line, coaxial probe feed, aperture coupling and proximity coupling. These techniques can be classified into two categories; contacting (microstrip line and coaxial probe) and non- contacting (aperture coupling and proximity coupling). In contacting technique the RF power is fed directly to the radiating patch using a connecting element such as microstrip line.

In non-contacting scheme, electromagnetic field coupling is done to transfer power between the microstrip line and the radiating patch.

1.1.3.1. Coaxial feed

The coaxial feed is the simplest feed structure for the microstrip antennas and remains among the most popular one, this is displayed in figure.1.4 and its equivalent circuit.

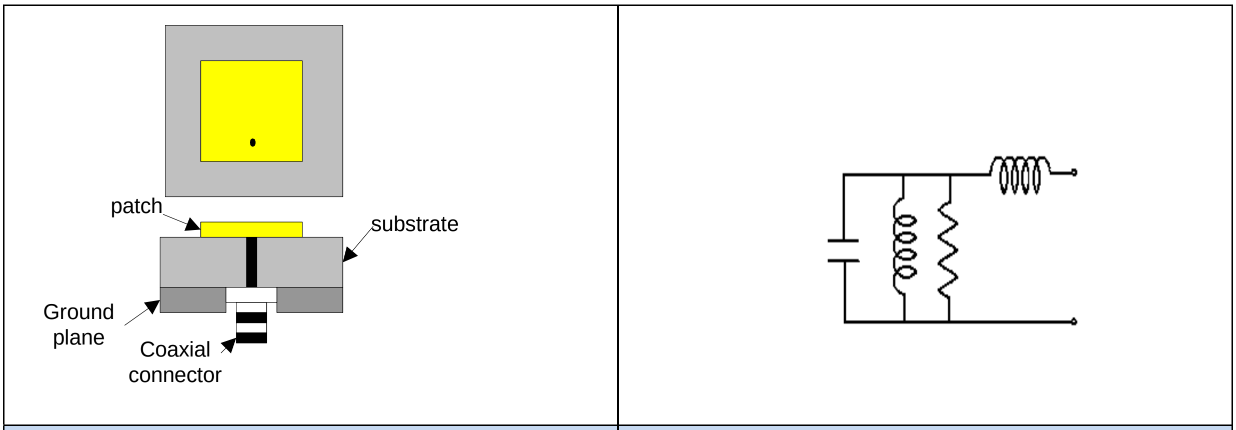

Probe feed

Electrical equivalent circuit

Fig.1.4 Feeding by a coaxial cable [4]

It is also referred as probe feed. It is a quite different way to feed a patch by means of a coaxial line that is set perpendicular to the ground plane. In this case the inner conductor of the coaxial line is attached to the radiating patch while the outer conductor is connected to the ground plane. It has low spurious radiation because the radiating and feeding systems are disposed on the two sides of the ground plane and shielded from each other. It is suitable for antenna array applications. It also has narrow bandwidth and it is more difficult to model, especially for thick substrates$(h > 0.02\lambda_0)$ [4].

1.1.3.2. Microstrip line feed

The simplest way to feed a microstrip patch is to connect a microstrip line directly to the edges of the patch as shown in figure.1.5. In this case both the patch and the lines are located on the same substrate. The conducting strip is smaller in width as compared to the patch and this kind of feed arrangement has the advantage that the feed can be etched on the same substrate to provide a planar structure. The microstrip feed line is easy to fabricate, simple to match by controlling the inset position and rather simple to model [1].

As the substrate thickness increases surface wave and spurious feed radiation increase, which, for practical designs limit the bandwidth (typically 2-5%) [4]. The drawback is the radiation from the feed line, which leads to an increase in the cross-polar level, And, in the millimetre-wave range.

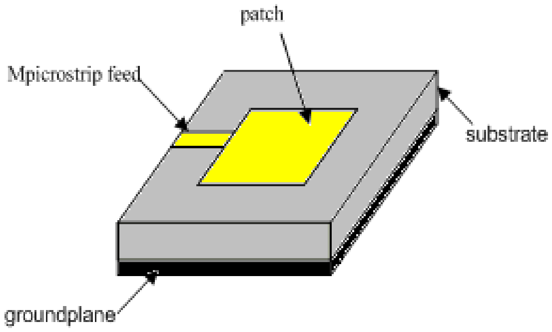	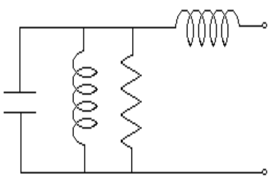
Microstrip line feed	Electrical equivalent circuit

Fig.1.5 Feeding by a microstrip line [4]

1.1.3.3. Proximity coupled feed

Proximity coupled feed is often referred in the literature as (electromagnetic coupling). The proximity coupled feed uses a two layer substrate with a microstrip line on the lower substrate terminating in an open stub below the antenna element which is printed on the upper substrate as illustrated in figure .1.6.

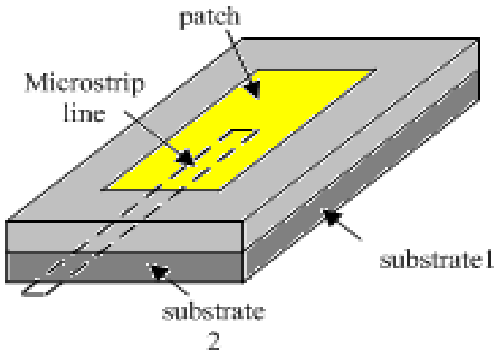	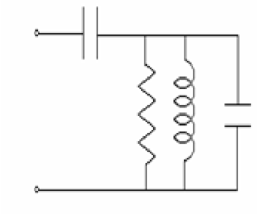
Proximity coupled feed	Electrical equivalent circuit

Fig.1.6 Feeding by proximity [4]

The advantage of this feed is to allow the patch to exist on a relatively thick substrate for improved bandwidth, while the feed line sees on the effectively thinner substrate which reduces spurious radiation and coupling. This scheme also provides choices between two different dielectric media one for the patch and one for the feed line to optimize the individual performance.

The main disadvantage of this feed scheme is that it is difficult to fabricate because of the two dielectric layers which need proper alignment. The length of the feeding stub and the width to line ratio of the patch can be used to control the match. The proximity coupling has the largest bandwidth and it is somewhat easy to model.

1.1. 3.4. Aperture coupling feed

The aperture coupling feeds is the most difficult of all feeds to fabricate, it is somewhat easier to model and, it has narrow bandwidth. It has moderate spurious radiation. The aperture coupling consists of two substrates separated by a ground plane, on the bottom side of the lower substrate there is a microstrip feed line whose energy coupled to the patch through a slot on the ground plane separating the two substrates as shown in figure.1.7. Typically a high dielectric material is used for the bottom substrate and thick low dielectric constant material for the top substrate.

The ground plane between substrates also isolates the feed from the radiating element and minimizes interference of spurious radiation for pattern formation and polarization purity. Typically matching is performed by controlling the width of the feed line and the length of the slot.

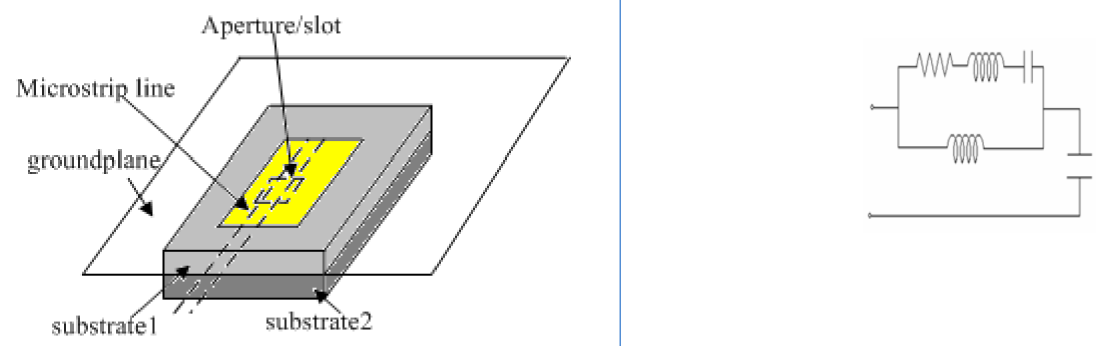

Aperture coupled feed

Electrical equivalent circuit

Fig.1.7 Feeding by aperture [4]

1.2. Small microstrip antennas

One of the trends in mobile terminal technology in the past few years has been to dramatically reduce the size and weight of the terminal. This remarkable reduction in the terminal's size has sparked a rapid evolution of the antennas used for mobile terminals. Hence, the design of antennas for small mobile terminals is becoming more challenging. The antennas are required to be small and yet their performances have to be maintained. However, usually a degradation of the gain and the bandwidth are observed when the antenna's size is reduced.

Microstrip antennas have the attractive features of low profile, small size, low cost, and conformability to mounting hosts. Therefore, MSAs are very promising candidates for satisfying this design consideration. Some of these small patches antennas are discussed below;

1.2.1. Rectangular and square patches

The first and probably the most utilized patch conductor geometry were the rectangular and square shapes. Figure 1.2 (b) and (g) show these geometries. For a rectangular patch, the antenna is excited at some point along the resonant dimension L to generate a mode in this direction. In general, the length of the patch controls the resonant frequency and the width of the patch affects the impedance level at resonance as well as the bandwidth (a second order effect); the larger is the patch width the smaller the input impedance of the antenna This statement is valid only under certain condition (relatively thin substrate material) [6]. As the thickness of the material increases to greater than $0.03\lambda_0$, these relationships are not mutually exclusive and the feeding procedure and location can dramatically change all the measures performance [6].

In general, of all the conductor shapes rectangular patches tend to have the largest impedance bandwidth, simply because they are larger than the other shapes. Squares patches can be designed to generate the dual or the circular polarization.

1.2.2. Circular and elliptical patches

Figure 1.2 (f) and (h) show schematic diagrams of circular and elliptical patch geometries. These shapes are probably the second most common geometry. Circular and elliptical patches are slightly smaller than their rectangular counterpart and as a result have slightly lower gain and bandwidth [6]. The dominant modal distribution on a circular patch is different to that for a rectangular/square patch conductor.

A circular patch, like a square patch only has one degree of freedom in its conductor shape and that's its radius. Thus changing the radius will control the resonant frequency of circular patch. Once again under conservative conditions, the feed position will control the input impedance of the antenna at the chosen resonant frequency.

One of the primary reasons the circular geometry was quite expensively investigated in the past was due to its inherent symmetry. This allowed full-wave analysis tools utilising a spectral domain technique to be written that were computationally more efficient than their rectangular counterpart.

This was important in the early stages of the patch design and development for it allowed performance trends of more complicated structures(such as stacked patches) to be explored and optimized efficiency. Importantly these trends could then be relayed back to other geometries, simply because most of the differences in performances of different conductor shapes are minimal. With the advent of several rigorous, computationally fast full-wave design tolls, such as ensemble and IE3D, systems incorporating circular patch antennas are becoming increasingly rare.

1.2.3. Triangular and disc sector patches

Triangular and disc sector patch geometries are smaller than their rectangular and circular counterparts, although at the expense of further reduction in bandwidth and gain. Figure 1.2 (d) and (i) show schematic diagrams of these conductor shapes. Triangular patches also tend to generate higher cross-polarization levels; due to their lack of symmetry in the configuration. And disc sector patches have a similar number design freedoms as the rectangular patch.

For a disc sector antenna, if the TM_{01} mode is excited, then the radius of the disc controls the resonant frequency and the sector angle controls the bandwidth and impedance [6]. Depending on the aspect of the triangle and the disc sector, dual frequency and dual polarized patches can be developed using either of these conductor shapes, however the bandwidth is typically very narrow [7]. Also for the dual frequency patch, the polarizations for each frequency band are orthogonal.

1.2.4. Annular rings

Annular ring geometries are the smallest conductor shape, once again at the expense of bandwidth and gain. Figure 1.2 (c) shows this conductor shape. One problem associated with an annular ring is that it is not simple process to excite the lowest order mode and obtain input impedance close to 50Ω.in fact, impedance values ranges from 150-250Ω are quite normal [6]. Non-contact forms of excitation are typically required to feed this element at the expense of antenna efficiency. The symmetry issues mentioned for the circular patch cases also apply here.

The annular ring has more design variable than the circular patch and therefore it's response should be easier to control. Both the inner and outer ring dimensions can be used to control the resonant frequency of the printed antenna, which is very advantageous. However, as the inner radius approaches the outer radius dimension, the impedance bandwidth becomes narrower, for more information about annular-ring patch antenna see appendix A.

1.3. Methods of analysis

Microstrip patch antenna generally has a two-dimensional radiating patch on a thin dielectric substrate, therefore may be categorized as a two-dimensional planar component for analysis purposes. The analysis methods for MSAs can be broadly divided into two groups.

In the first group, the methods are based on equivalent magnetic current distribution around the patch edges (similar to slot antennas) [8]. This group includes three popular analytical techniques:

- Transmission line model; [1,2,4]
- Cavity model ;[1,2,4]
- Multiport network model (MNM);[8]

In the second group, the methods are based on the electric current distribution on the patch conductor and the ground plane (similar to dipole antennas, used in conjunction with full-wave simulation/numerical analysis methods) [8]. Some of these numerical methods are:

- Method of Moments (MoM) ;[9;10]
- Finite Element Method (FEM);[11]
- Spectral Domain Technique (SDT);[8]
- Finite Difference Time Domain (FDTD) method which is chosen in this work to analyse various shapes of microstrip patches antennas; [12, 10, 13].

1.4. Finite Difference Time Domain (FDTD) method

The Finite Difference Time Domain (FDTD) method is a full-wave , dynamic, and powerful solution tool for solving Maxwell's equations, introduced by K.S. Yee in 1966 [12]. This method becomes one of the attractive methods due to its programming simplicity and flexibility in analyzing wide range of Electromagnetic structures. The algorithm involves direct discretization of Maxwell's equations by writing the spatial and time derivatives in a central finite difference form. It is based on simple formulations that do not require complex asymptotic or Green's functions.

The first applications of FDTD were scattering and penetration problems [14]. Many researchers have contributed immensely to extend the method to many areas of science and engineering (Taflove 1995, 1998). FDTD method did not become popular until 1975 when Taflove et al. applied the technique for the solution of complex inhomogeneous problem [15]. In 1980, the algorithm became known as the finite difference time domain (FDTD) method in a paper published by Taflove et al [15]. FDTD has been used very successfully in the design of antennas for several applications ranging from simple microstrip antennas to complex phased-array antennas. Some of these antennas are currently being used in mobile communications.

In 1988, X. Zhang and K. K. Mei et al. calculated the dispersive characteristics of microstrip and frequency-dependent characteristics of microstrip discontinuities using FDTD [16]. They compared their results with other published ones and verified that FDTD is a viable method for modelling microstrip components. In 1989 FDTD was first used to analyse microstrip patch antennas by A. Reineix et al. [17] and some frequency-dependent parameters were given using FFT. In 1990, D. M. Sheen et al. [18] presented FDTD results for various microstrip structures, including microstrip rectangular patch antenna, a low-pass filter and a branch-line coupler.

Furthermore, using FDTD, Maxwell's equations are discretized into both time and spatial central finite difference equations. Knowing the initial, boundary and excitation conditions, the fields on the nodal points of the space-time mesh can be calculated in a *leapfrog* time marching manner. FDTD was limited to the modeling of finite space problems. The absorbing boundary conditions (ABCs) permit modeling of infinite problems such as an antenna radiating in free space. ABCs such as Mur, Higdon and perfectly matched layer (PML) are all methods of absorbing the fields radiating from the source as they propagate towards the boundary [12].

The FDTD method has a number of characteristics that really make it stand out when compared with the other techniques commonly used for antenna design and analysis. These characteristics are:

- FDTD is a fully explicit computation: This means that FDTD avoids the difficulties with linear algebra, namely matrix inversion, that limit the size of frequency-domain integral equation (MoM) and finite element electromagnetic models to about 10^6 field unknowns [19]. FDTD simulations have been run with 10^9 field unknowns and this limit only depends on the amount of physical memory available for the computation.
- FDTD naturally calculates the impulse response of an electromagnetic system since it is a time-domain method. Therefore, a single FDTD run can provide ultra wideband temporal waveforms that can be used to, by means of a discrete Fourier transform (DFT) and obtain the antenna's response over a broad frequency range.
- Ability to model most materials, including lossy dielectrics, magnetic materials, lossy metals and unconventional materials, including anisotropic plasmas and magnetized ferrites.
- Ability to model nonlinear materials, since nonlinear behavior can more easily be treated in time domain than in the frequency-domain.
- FDTD, unlike methods that rely on integral equations, does not require the calculation of structure dependent Green's functions the specification of a new structure for analysis just requires the generation of a new mesh. Although the problem of mesh generation can be quite complex, since the majority of FDTD codes currently available use Cartesian meshes (hexahedral cells), the problem of mesh generation is considerably simpler than that of mesh generation for FEM codes (which use tetrahedral elements).
- Although powerful visualization capabilities exist for all methods, FDTD can provide field visualization in both time and frequency-domain, which provides more insight to the problem under analysis.
- FDTD is easier to understand and to implement than MoM and FEM. Additionally, the FDTD marching-in-time field update procedure is relatively easy to parallelize in order to take advantage of multiple CPUs or even multiple computers to speed up the simulation of complex problems.

In this technique, spatial as well as time grid for the electric and magnetic fields are generated over which the solution is required. The spatial discretization along three Cartesian coordinates is taken to be same. The E cell edges are aligned with the boundary of the configuration and H-fields are assumed to be located at the center of each E cell. Each cell contains information about material characteristics. The cells containing the sources are excited with a suitable excitation function, which propagates along the structure. The discretized time variations of the fields are determined at desired locations. Using a line integral of the electric field, the voltage across the two locations can be obtained. The current is computed by a loop integral of the magnetic field surrounding the conductor, where the Fourier transform yields a frequency response.

The above numerical techniques, which are based on the electric current distribution on the patch conductor and the ground plane, give results for any arbitrarily shaped antenna with good accuracy, but they are time consuming. These methods can be used to plot current distributions on patches but otherwise provide little of the physical insight required for antenna design.
Figure 1.8 illustrate and summarize the basic flow of implementing FDTD scheme on a computer.

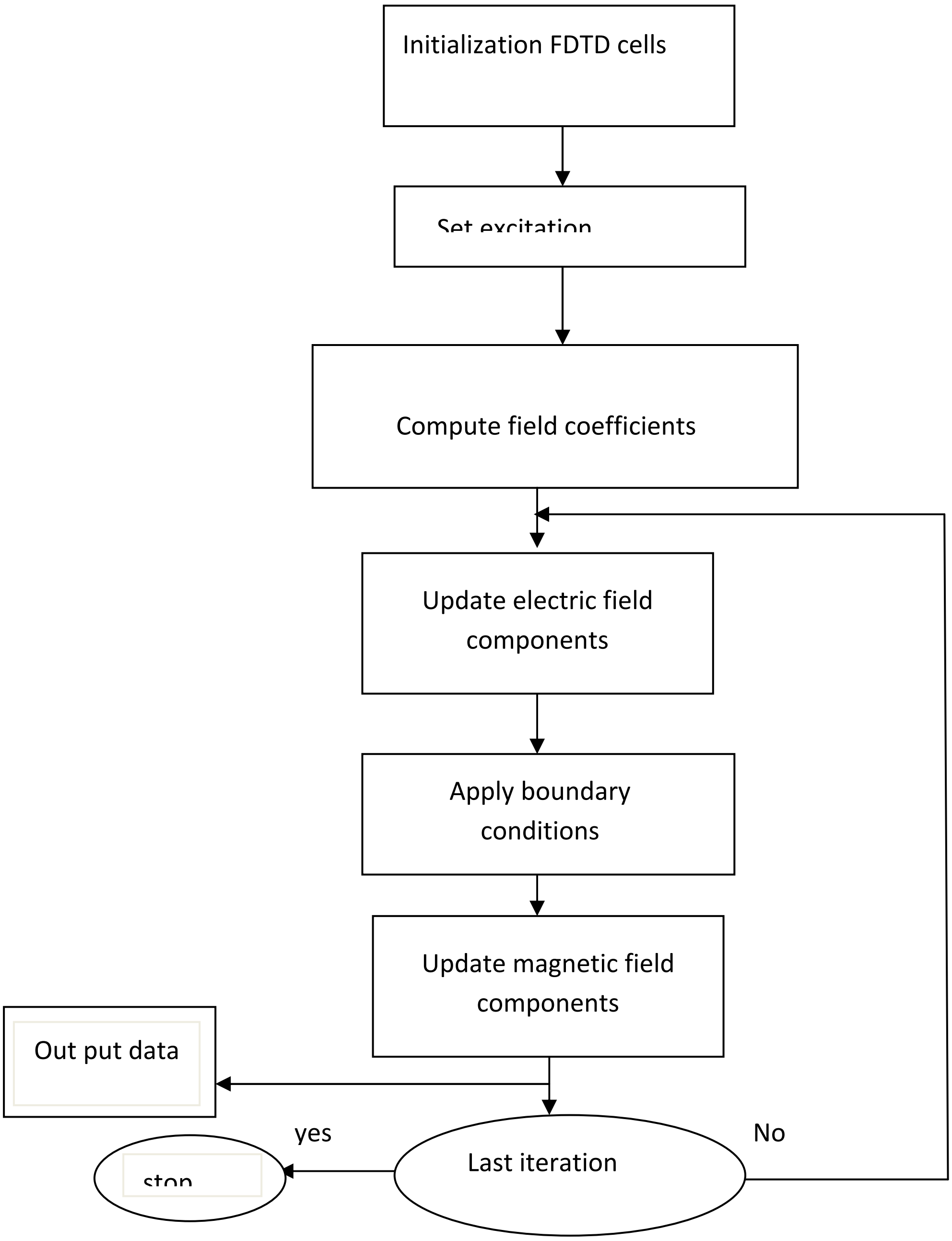

Fig. 1.8 Flow chart of FDTD algorithm [7]

Due to the advantages of FDTD method aforementioned, it is applied in this research for the analysis of microstrip patch antenna structures. HFSS simulator is used in this work to compare with the result obtained with FDTD method, Ansoft HFSS simulator is based on finite element method (FEM).

1.5. Overview of HFSS simulation

The name HFSS stands for High Frequency Structure Simulator. HFSS is a high-performance full-wave electromagnetic (EM) field simulator for arbitrary three dimension (3D) volumetric passive device modeling that takes advantage of the familiar Microsoft Windows graphical user interface. The software gained instant popularity because; it brought the power of finite element method (FEM) to design engineers. It integrates simulation, visualization, solid modeling, and automation in an easy-to-learn environment where solutions to 3D EM problems are quickly and accurately obtained. Ansoft HFSS employs the Finite Element Method (FEM), adaptive meshing, and brilliant graphics to provide unparalleled performance and insight to all of 3D EM problems. Ansoft HFSS can be used to calculate parameters such as S-parameters, Resonant Frequency and Fields [21].
The applications of HFSS are:

- Package Modeling – BGA, QFP, Flip-Chip
- PCB Board Modeling – Power/Ground planes, Mesh Grid Grounds, Backplanes
- Silicon/GaAs - Spiral Inductors, Transformers
- EMC/EMI – Shield Enclosures, Coupling, Near- or Far-Field Radiation
- Antennas/Mobile Communications – Patches, Dipoles, Horns, Conformal Cell Phone Antennas, Quadrafilar Helix, Specific Absorption Rate(SAR),Infinite Arrays, Radar Cross Section(RCS), Frequency Selective Surfaces(FSS)
- Connectors – Coax, SFP/XFP, Backplane, Transitions
- Waveguide – Filters, Resonators, Transitions, Couplers
- Filters – Cavity Filters, Microstrip, Dielectric

HFSS is an interactive simulation system whose basic mesh element is a tetrahedron. This allows you to solve any arbitrary 3D geometry, especially those with complex curves and shapes, in a fraction of the time it would take using other techniques.

Ansoft pioneered the use of the Finite Element Method (FEM) for EM simulation by developing/implementing technologies such as tangential vector finite elements, adaptive meshing, and Adaptive Lanczos-Pade Sweep (ALPS) [21]. Today, HFSS continues to lead the industry with innovations such as Modes-to-Nodes and Full-Wave Spice™. Ansoft HFSS has evolved over a period of years with input from many users and industries. In industry, Ansoft HFSS is the tool of choice for high-productivity research, development, and virtual prototyping, for more information see appendix C.

Chapter II

This chapter describes basic concepts and formulation of Finite Difference Time Domain (FDTD) and its implementation for the analysis of microstrip antenna.

2.1. Implementation FDTD in microstrip antenna

In order to study the microstrip antennas using finite difference time domain, some theoretical concepts and formulations must be first understood. This section presents the fundamentals of the finite difference time-domain method and the derivation of the algorithm used in this work.

Consider a microstrip antenna with an arbitrary shape separated from the ground plane by a dielectric substrate of height *h* and (ε_r permittivity) as shown in the figure 2.1.

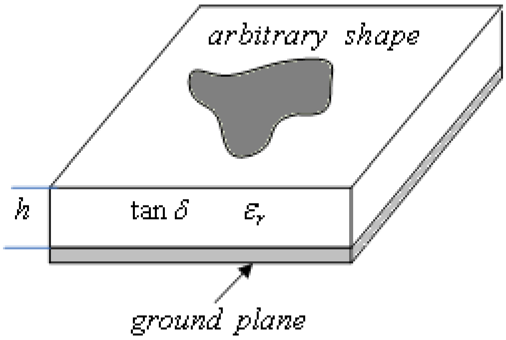

Fig .2.1 Microstrip antenna of arbitrary shape

Formulation of the FDTD method starts by considering the time dependent Maxwell's equations in differential form.

2.1.1. Maxwell’s equations

Propagation of electromagnetic waves can be represented with the time domain Maxwell’s curl equation, as:

$$-\vec{\nabla} \times \vec{E} = \mu \frac{\partial H}{\partial t} \tag{2.1}$$

$$\vec{\nabla} \times \vec{H} = \sigma \vec{E} + \varepsilon \frac{\partial E}{\partial t} \tag{2.2}$$

$$\nabla \cdot B = 0 \tag{2.3}$$

$$\nabla \cdot D = \rho \tag{2.4}$$

Where B=μH , D=εE, $\vec{E}$ is the electric field in vol/meter, $\vec{H}$ is the magnetic field in ampere/meter, ε is the electric permittivity in farad/meter, μ is the magnetic permeability in Henry/meter and σ is the conductivity in (siemens)/m .

Assuming isotropic physical parameters, Maxwell’s equation can be written in rectangular coordinates as:

$$\frac{\partial H_x}{\partial t} = \frac{1}{\mu}\left(\frac{\partial E_y}{\partial z} - \frac{\partial Ez}{\partial y}\right) \tag{2.5a}$$

$$\frac{\partial H_y}{\partial t} = \frac{1}{\mu}\left(\frac{\partial E_z}{\partial x} - \frac{\partial Ex}{\partial z}\right) \tag{2.5b}$$

$$\frac{\partial H_z}{\partial t} = \frac{1}{\mu}\left(\frac{\partial E_x}{\partial y} - \frac{\partial E_y}{\partial x}\right) \tag{2.5c}$$

$$\frac{\partial E_x}{\partial t} = \frac{1}{\varepsilon}\left(\frac{\partial H_z}{\partial y} - \frac{\partial H_y}{\partial x} - \sigma E_x\right) \tag{2.5d}$$

$$\frac{\partial E_y}{\partial t} = \frac{1}{\varepsilon}\left(\frac{\partial H_x}{\partial z} - \frac{\partial H_z}{\partial x} - \sigma E_y\right) \tag{2.5e}$$

$$\frac{\partial E_z}{\partial t} = \frac{1}{\varepsilon}\left(\frac{\partial H_y}{\partial x} - \frac{\partial H_x}{\partial y} - \sigma E_z\right) \tag{2.5f}$$

These equations will govern the field's propagation within the patch antenna structure and the surrounding space. To approximate the partial derivatives in space and time domains by finite differences, the antenna structure and the surrounding space are discretised over a finite three-dimensional computational domain. The spatial and temporal discretization scheme used will determine the nature of the grid and thus the finite difference scheme used. The spatial discretization scheme is usually chosen to fit the geometry of the antenna. Therefore, if the rectangular structure is selected, an orthogonal grid is used, whereas if the structure is spherical, it might be better to opt for a spherical grid. In the case of patch structures orthogonal grids are best suited for rectangular patches and cylindrical grids for circular patches.

However, since various patch shapes were considered, an orthogonal gridding method was used and curved edges were approximated by stair-casing. In uniform orthogonal gridding the structure and the surrounding space are discretised as shown in figure.2.2. The spatial increments Δx ,Δy and Δz can take any value and may not be the same. They are usually chosen to fit the antenna being modelled.

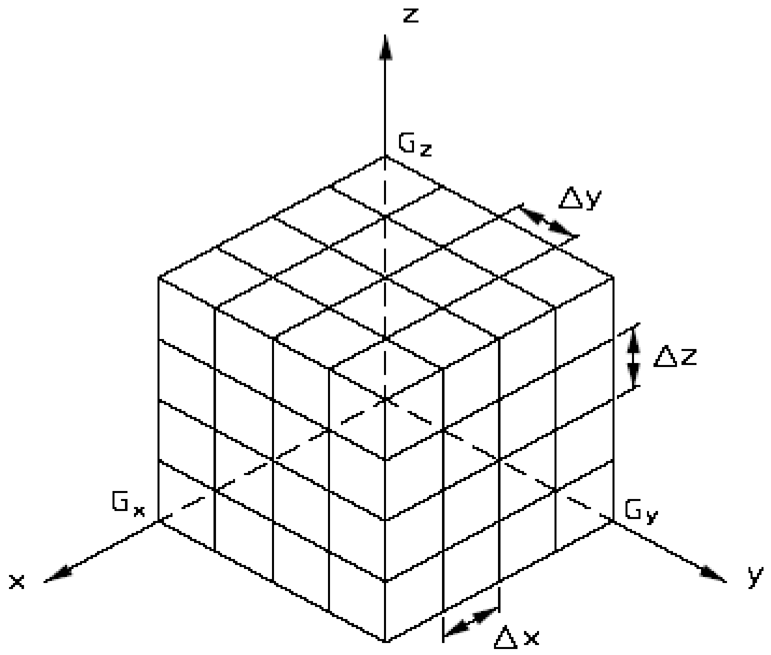

Fig 2.2 The Yee orthogonal grid [22]

The size of the grid is G_x, G_y and G_z in the x, y and z directions respectively. The finer the structural features, the denser the grid, since Δx ,Δy and Δz are smaller. This is particularly an important consideration since the denser the grid, the larger the memory storage and the longer the computational time becomes. The uniform orthogonal grid was first proposed and used by Yee, 1966 [12].

The electric and magnetic field components are located at interleaved points on the spatial grid of figure.2.3. The spatial grid is divided into small cells as shown in figure.2.3 and the electric field components are located on the edges of each cell, while the magnetic field components are located at the centre of the cell faces. Using this arrangement equation (2.1) and (2.2) can then be approximated using central differences in the spatial and temporal domains. However prior to deriving the full finite-difference equations it is useful to define Yee's notation.

1.A point in space is denoted by, (i, j, k) and is located at (iΔx ,j Δy , k Δz) where Δx , Δy and Δz are the spatial increments and i, j, k are integers

2.A function f of space and time is then, $f(i\Delta x, j\Delta y, k\Delta z, n\Delta t) = f\big|_{i,j,k}^{n}$

Where Δt is the time increment and n is the time step. The first partial derivative of a function $f(x)$ with respect to x is expressed in finite central differences as

$$\frac{\partial f(x)}{\partial x} = \frac{f(x_0 + \Delta x/2) - f(x_0 - \Delta x/2)}{\Delta x} + O\left[(\Delta x)^2\right] \qquad (2.6)$$

Where x_0 is the derivative calculation point and Δx is the increment

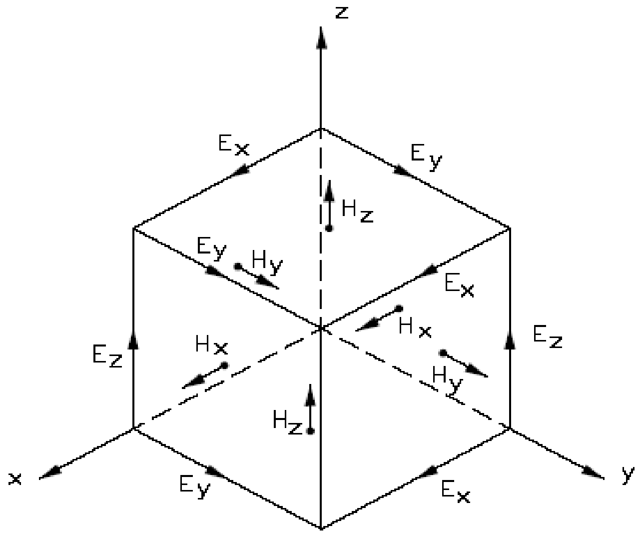

Fig. 2.3 The Yee cell [22]

Using Yee's notation the central spatial finite difference equation is given by

$$\frac{\partial f}{\partial x}(i\Delta x, j\Delta y, k\Delta z, n\Delta t) = \frac{f\big|_{i+1/2,j,k}^{n} - f\big|_{i-1/2,j,k}^{n}}{\Delta x} + O\left[(\Delta x)^2\right] \tag{2.7}$$

For a second-order accurate derivation, the O $[(\Delta x)^2]$ term is considered to be very small, and is discarded.

Considering next equation (2.2) with central time difference yields,

$$\nabla \times H^{n+1/2} = \sigma E^{n+1/2} + \varepsilon\left(\frac{E^{n+1} - E^{n}}{\Delta t}\right) \tag{2.8}$$

$E^{n+1/2}$ can be written as $\left(E^{n+1/2} - E^{n+1/2}\right)/\,2$ and equation (2.8) becomes,

$$\nabla \times H^{n+1/2} = \sigma\left(\frac{E^{n+1} + E^{n}}{2}\right) + \varepsilon\left(\frac{E^{n+1} - E^{n}}{\Delta t}\right) \tag{2.9}$$

Rearranging equation (2.9) yields,

$$\nabla \times H^{n+1/2} = E^{n+1}\left(\frac{\sigma}{2} + \frac{\varepsilon}{\Delta t}\right) + E^{n}\left(\frac{\sigma}{2} - \frac{\varepsilon}{\Delta t}\right) \tag{2.10}$$

And solving for E^{n+1} gives

$$E^{n+1} = \left(\frac{\frac{\varepsilon}{\Delta t} - \frac{\sigma}{2}}{\frac{\varepsilon}{\Delta t} + \frac{\sigma}{2}}\right)E^{n} + \frac{\nabla \times H^{n+1/2}}{\left(\frac{\varepsilon}{\Delta t} + \frac{\sigma}{2}\right)} \tag{2.11}$$

This can also be written as

$$E^{n+1} = \left(\frac{1 - \frac{\Delta t\sigma}{2\varepsilon}}{1 + \frac{\Delta t\sigma}{2\varepsilon}}\right)E^{n} + \left(\frac{\frac{\Delta t}{\varepsilon}}{1 + \frac{\Delta t\sigma}{2\varepsilon}}\right)\nabla \times H^{n+1/2} \tag{2.12}$$

Considering only E_x ,$\nabla \times H$ reduces to,

$$\nabla \times H = \left(\frac{\partial H_z}{\partial y} - \frac{\partial H_y}{\partial z}\right) \tag{2.13}$$

Taking the spatial central difference for equation (2.13),

$$\frac{\partial H_z}{\partial y}-\frac{\partial H_y}{\partial z}=\frac{H_z\big|_{i,j+1/2,k}^{n+1/2}-H_z\big|_{i,j-1/2,k}^{n-1/2}}{\Delta y}-\frac{H_y\big|_{i,j,k+1/2}^{n+1/2}-H_y\big|_{i,j,k-1/2}^{n-1/2}}{\Delta z} \tag{2.14}$$

and substituting equation(2.14) into(2.12) results in,

$$E_x\big|_{i,j,k}^{n+1}=\left(\frac{1-\frac{\Delta t\sigma}{2\varepsilon}}{1+\frac{\Delta t\sigma}{2\varepsilon}}\right)E_x\Big|_{i,j,k}^{n}+\left(\frac{\frac{\Delta t}{\varepsilon}}{1+\frac{\Delta t\sigma}{2\varepsilon}}\right)\left(\frac{H_z\big|_{i,j+1/2,k}^{n+1/2}-H_z\big|_{i,j-1/2,k}^{n-1/2}}{\Delta y}-\frac{H_y\big|_{i,j,k+1/2}^{n+1/2}-H_y\big|_{i,j,k-1/2}^{n-1/2}}{\Delta z}\right) \tag{2.15}$$

Equation (2.15) shows that the value of E_x depends on its previous value and on the magnetic field surrounding the electric field. Similarly, a magnetic field component depends on its previous value and on the electric field surrounding it. The difference equations for E_y, E_z,H_x, H_y, H_z are derived in the same manner. These equations are called the field update equations and are solved in a *leapfrog* manner, instead of solving them for either the electric field alone or the magnetic field alone as is done with a wave equations. In a finite difference scheme, there are three aspects that must be considered [22]:

(a) The continuous derivative must be accurately approximated.
(b) The method must be stable, i.e. numerical errors must not grow as the simulation proceeds.
(c) Numerical dispersion should be small.

The central difference approximates the first derivative to second order in Δ. Therefore high accuracy is obtained for waveforms which change slowly in the period Δ. Third and higher order derivatives are small in the period Δ and are ignored, (equation 2.5). Therefore, for fast moving waves, Δ should be smaller. Since all the derivatives are approximated by central differences, then the error is always second order in time and space. This implies that accuracy depends on the choice of Δx ,Δy , Δz and $c\Delta t$, which should be small compared to the wavelength.

The chosen values for the spatial increments should therefore ensure linearity in the fields and should be small enough so as to follow all the structural features of the patch antenna. The time step Δt is also restricted due to stability reasons. Instability arises when the numerical errors tend to grow exponentially.

For the central difference scheme stability is ensured by enforcing the Courant limit [11], which is an upper bound for Δt ,so that;

$$\Delta t_{\max} \leq \frac{1}{v_{\max}\sqrt{\frac{1}{\Delta x^2}+\frac{1}{\Delta y^2}+\frac{1}{\Delta z^2}}} \tag{2.16}$$

Where $\Delta t_{\max}$ is the maximum time step,

Δx , Δy , Δz are the dimensions of one cell, and

$v_{\max}$ is the maximum velocity of the waves in the media.

Equation (2.14) is known as *Courant-Friedrich-Levy criterium.*

Basically stability is ensured by limiting the distance travelled by the wave in one time step. In this work, we assume $v_{\max} = c$, since the patch antenna structure is always partly situated in free-space. Some structures will permit the use of a larger time step and so the computational time is reduced. However since the patch antenna is highly resonant the time step is set to $0.95\,\Delta t_{\max}$ to ensure stability all the time [22].

Finite difference scheme causes numerical dispersion, i.e. the phase velocity of the wave propagating in the FDTD lattice can differ from the actual value in real material. Numerical dispersion is a function of the spatial discretization and increases as the cell size increases with respect to the wavelength. Therefore the higher frequency components are affected most. When the discretization is about 20 points per wavelength, phase velocity errors are less than 0.5%, [22]. This is adequate for the considered structures studied because the discretization is usually 40 to 80 points per wavelength. A full treatment of numerical stability in finite difference schemes and numerical dispersion is deeply investigated in [12].

In such cases, the numerical errors are not due to numerical dispersion but essentially due to differences between the meshed version of the structure and its real geometry. For a cartesian grid, these errors are generally associated with its inability to conform to curved surfaces or boundaries not aligned with its axes, and are called stair-casing errors. An example of stair-casing is shown in figure. 2.4. Therefore, an even finer mesh might be necessary if the structure being simulated has very fine geometrical features.

It is also important to mention that errors in numerical phase velocity are cumulative and, as a consequence, the simulation of electrically large structures in FDTD may require a sampling density that increases with the size of the structure under analysis.

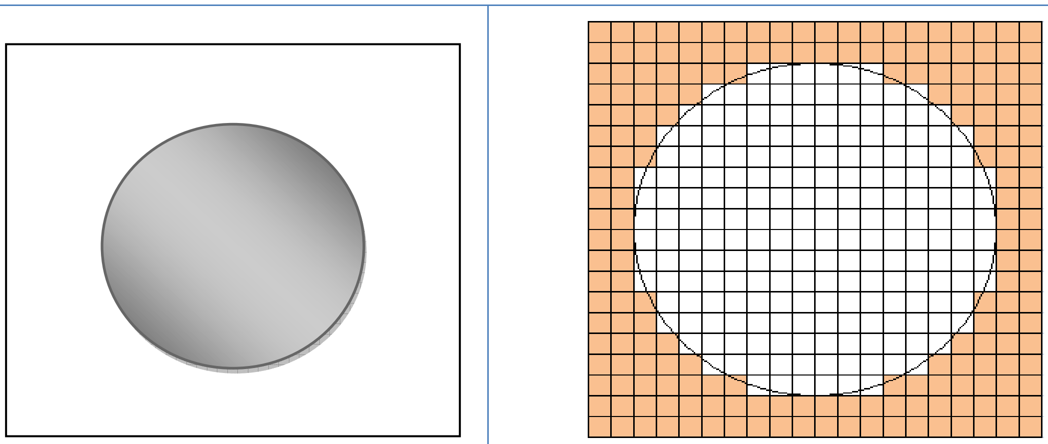

A circular metallic patch

its meshed version where the stair-cased approximation of the curved boundary can be observed

Fig .2.4 Stair-cased approximation [19].

2.1.2. Interface between Media

The FDTD equations derived in section 2.1.1 are valid only for homogeneous regions. However, in many simulations, however, multiple dielectric materials are used. In microstrip patch antenna structure consists of three materials: free space, dielectric material of the substrate and metal plates. Within the various dielectric regions the standard FDTD equations may be applied, but some cases must be considered at the dielectric interfaces. Figure 2.5 shows a group of four cells depicting a non-conducting region where four different dielectrics meet. We see that the E_x field component lies along the four dielectric interfaces.

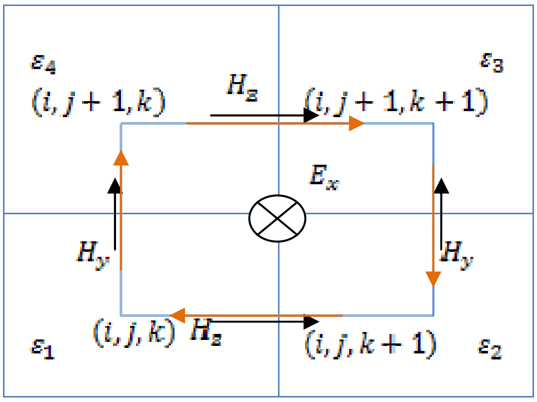

Fig.2.5 Dielectric interface [23]

From the integral form of Ampere's Law:

$$\frac{\partial}{\partial t}\iint_s (D.d\hat{S}) = \oint_c (H.d\hat{l}) - \iint_s (J_e.d\hat{S}) \qquad (2.17)$$

Upon applying this formula to the four-cell structure (Figure 2.5) along the dotted curve, and assuming, that there is no conduction current. The following equation applies:

$$\left(\frac{\varepsilon_1+\varepsilon_2+\varepsilon_3+\varepsilon_4}{4}\right)\left(\frac{\partial}{\partial t}E_x\Big|_{i+\frac{1}{2},i,k}^{n+\frac{1}{2}}\right) = \left(\frac{H_z\Big|_{,+\frac{1}{2},j,k}^{n+\frac{1}{2}} - H_{z|}\Big|_{i+\frac{1}{2},j-\frac{1}{2},k}^{n+\frac{1}{2}}}{\Delta y} - \frac{H_z\Big|_{i+\frac{1}{2},j,k+\frac{1}{2}}^{n+\frac{1}{2}} - H_y\Big|_{i+\frac{1}{2},j,k-\frac{1}{2}}^{n+\frac{1}{2}}}{\Delta z}\right) \qquad (2.18)$$

We notice that this is merely equation (2.15), with an equivalent dielectric constant equal to the average of the four dielectric constants;

$$\varepsilon_{\text{int}ercace} = \frac{\varepsilon_1+\varepsilon_2+\varepsilon_3+\varepsilon_4}{4} \qquad (2.19)$$

In a similar manner, the proper conductivity at the interface can be expressed as

$$\sigma_{\text{int}erface} = \frac{(\sigma_1+\sigma_2+\sigma_3+\sigma_4)}{4} \qquad (2.20)$$

The updating coefficients for the E_x field at the interface can now be calculated.Similar expressions can be found for all E and H field components lying on the electric or magnetic material interfaces [23].

2.2. Antenna Feed Models

One of the most important aspects in an FDTD simulation is the modeling of the excitation sources that introduce electromagnetic energy into the computational domain.

This modeling comprises the choice of the signal used to excite the antenna and how this signal is to be applied on the field components of the FDTD grid. This section describes the excitation signals used in FDTD algorithm and two kinds of antenna feed models; Improved simple feed and gap feed source models [12].

2.2.1. Excitation Signals

The FDTD antenna model can be excited by any time domain waveform. It is important to consider the introduction of electromagnetic wave excitations into the FDTD mesh. These excitations are associated with time domain signals that take different shapes.

There are two types of sources, the hard source and the soft source. If a source is assigned a value to E, it is referred to as a hard source. If a value is added to E at a certain point, it is referred to as a soft source. With a hard source, a propagating pulse will see that value and be reflected, because a hard value of E looks like a metal wall to the FDTD but, with a soft source, a propagating pulse will just pass through [20].

A Gaussian pulse is desirable as the excitation because its frequency spectrum is also Gaussian and provides frequency-domain information from dc to the desired cut off frequency by adjusting the width of the pulse [14]. It can be represented by the following formula:

$$g(t) = e^{-(t-t_0)^2/T^2} \tag{2.21}$$

Its Fourier Transform is also Gaussian pulse in the frequency domain:

$$G(f) = \sqrt{\pi} T e^{-\pi^2 T^2 f^2} e^{-j2\pi f t_0} \tag{2.22}$$

The parameters T & t_0 should be chosen so that

- The Gaussian pulse can provide relatively high signal levels within the frequency range of interest to ensure good numerical accuracy.
- The Gaussian pulse can provide small signal levels for high frequency components with wavelengths are comparative to the step size for reducing noise and instability.
- The Gaussian pulse must be wide enough to contain enough space divisions for a good resolution after the space discretization interval Δ has been chosen to be fine enough to represent the smallest dimension of the geometry structure and the time
- Discretization interval Δt has been selected small enough to meet the stability criterion.
- The spectrum of the pulse must be wide enough (i.e. the pulse width must still be narrow enough) to maintain a substandard value within the frequency value of interest.

If the last two conditions can not be met simultaneously, the space discretization interval Δ has to be readjusted.

The pulse width W generally should be greater than 20 space steps [16]. The pulse width is defined as the width between the two symmetric points which have 5 percent of the maximum value of the pulse. It can be estimated using the following formula [16]:

$$W = \frac{2\sqrt{3}\, v\, T}{\Delta} \tag{2.23}$$

Therefore, T is determined from:

$$T = \frac{10\Delta}{\sqrt{3} \cdot v} \tag{2.24}$$

The maximum frequency which can be calculated is [14]:

$$f_{\max} = \frac{1}{2T} = \frac{\sqrt{3} \cdot v}{20 \cdot \Delta} \tag{2.25}$$

Where v is the minimum velocity of pulse in the structure under consideration and;

Δ is the space step. With the spacing Δ $f_{\max}$ is high enough to cover the whole frequency range of interest [16].

The choice of the parameter t_0 should be made so that the initial "turn on" of the excitation will be small and smooth. In the current work, t_0 is set to 3T so that the pulse is down to e^{-9} of its maximum value at the truncation time t = 0 or t = $2t_0$. Since the single precision floating point is used in this study, the choice of t_0 is acceptable [16].

2.2.2. Gap Feed Model

The gap feed model, which turns out to be the simplest one, consists of a feeding structure realized as a voltage generator with an internal resistor placed at a small gap between the patch and ground plane. This model works well assuming that the coaxial probe is very thin.

An added internal resistor can provide an additional loss mechanism to decrease the current amplitude rapidly and then reduce the required simulation steps. A larger resistance can provide more loss and further reduce the time steps required for convergence [7]. However, it has been shown through numerical experiments that the resistance cannot be too large; otherwise the accuracy level is not satisfied, and instabilities might occur because of neglecting the displacement current through the FDTD cell containing the source. The value of the internal source resistance is generally chosen as the system characteristic impedance to physically mimic the system [7]. Because all the microwave equipment is set to 50 Ω, the source resistance is thus chosen to be 50 Ω [7].

The FDTD implementation of this voltage source with an internal resistor can be illustrated by its equivalent circuit representation. A voltage source V_s^n in series with the internal resistor $R_s = 50\Omega$ is located between nodes (i, j, k) and $(i, j, k+1)$ as shown in Figure.2.6. The voltage source waveform can be of the source waveform types presented in section 2.3.1. The voltage at the feed point node $(i, j, k), V_z^n$ is represented in the FDTD simulation by an imposed E_z field at the feed point. The E_z field component is updated based on Ampere's Maxwell's equation, that is,

$$\frac{\partial E_z}{\partial t} = \frac{1}{\varepsilon}\left(\frac{\partial H_y}{\partial x} - \frac{\partial H_x}{\partial y} - \frac{I_{sz}}{\Delta x \Delta y}\right) \tag{2.26}$$

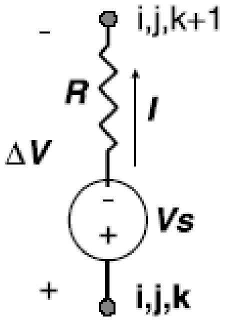

Fig 2.6 A resistive voltage source between nodes (*i*, *j*, *k*) and (*i*, *j*, *k* + 1) [7]

This transforms to the FDTD updating form to

$$\frac{E_z^{n+1}(i,j,k)-E_z^{n}(i,j,k)}{\Delta t}=\frac{1}{\varepsilon(i,j,k)}\left[\begin{array}{l}\dfrac{H_y^{n+1/2}(i,j,k)-H_y^{n+1/2}(i-1,j,k)}{\Delta x}-\dfrac{H_x^{n+1/2}(i,j,k)-H_x^{n+1/2}(i,j-1,k)}{\Delta y}\\ -\dfrac{I_{sz}^{n+1/2}(i,j,k)}{\Delta x\Delta y}\end{array}\right] \tag{2.27}$$

Then, because the voltage between the nodes (*i*, *j*, *k*) and (*i*, *j*, *k* + *1*) is the sum of the voltage drop across the resistance and the source voltage, we get:

$$I_{sz}^{n+1/2}=\frac{\Delta V_z^{n+1/2}-V_s^{n+1/2}}{R}=\frac{\Delta z\left(\dfrac{E_z^{n+1}(i,j,k)+E_z^{n}(i,j,k)+}{2}\right)-V_s^{n+1/2}}{R} \tag{2.28}$$

From Eq. (2.25) and (2.26), the expression for the z component of the electric field at (i, j, k) can be obtained. It is worth to notice that the connecting wire with infinitesimal diameter in this model of the feeding structure is actually modeled in the FDTD problem space by setting to zero the tangential component of the electric field (i.e., E_z).

This simple model can also be used to simulate a microstrip feeding structure. However, because the wire is a non-physical structure for the microstrip feed, a series inductance needs to be removed from the final results during the post processing [7].

Calculation of the input impedance and the scattering parameter:

The input impedance Z_{in} is calculated using the equation:

$$Z_{in} = \frac{V_{in}(f)}{I_{in}(f)} \tag{2.29}$$

The voltage *V* (*f*) and the current *I*(*f*) are Fourier transforms of time-dependent voltage *V* (*t*) and current *I*(*t*) at the feed point (*is, js, ks* + 1/2).

V (*t*) and *I* (*t*) are expressed as follows:

$$V(t) = -E_z^n\left(is,\, js, ks + \frac{1}{2}\right)\Delta x \tag{2.30}$$

$$\begin{aligned} I(t) = &\left\{H_y^{n-\frac{1}{2}}\left(is + \frac{1}{2},\, js, ks + \frac{1}{2}\right) - H_y^{n-\frac{1}{2}}\left(is - \frac{1}{2},\, js, ks + \frac{1}{2}\right)\right\}\Delta y - \\ &\left\{H_x^{n-\frac{1}{2}}\left(is,\, js + \frac{1}{2}, ks + \frac{1}{2}\right) - H_x^{n-\frac{1}{2}}\left(is,\, js - \frac{1}{2}, ks + \frac{1}{2}\right)\right\}\Delta x \end{aligned} \tag{2.31}$$

And

$$S_{11} = \frac{Z_{in} - Z_0}{Z_{in} + Z_0} \tag{2.32}$$

2.2.3. Improved simple feed model

In this model, the one dimensional FDTD grid shown in figure 2.7 is used to represent the transmission line attached to the antenna. The source is modeled by a voltage source of an internal resistance R_s that is connected to a unidimensional virtual transmission line of characteristic impedance also equal to R_s. The line is said to be virtual for the reason that it does not belong to the 3-D computational domain, being rather a numerical model that will be useful to separate the incident and the reflected voltage waves. For practical purposes, this source can be regarded as a lumped voltage source that is placed at the location of a single grid cell located between two metallic objects [12], such as the gap that exists between the arms of a dipole antenna, as shown in figure. 2.7.

The voltages and currents in the line are updated using the following expressions [12]:

$$I_{k+\frac{1}{2}}^{n+\frac{1}{2}} = I_{k+\frac{1}{2}}^{n+\frac{1}{2}} - \left(\frac{1}{Z_0}\right)\left(\frac{\upsilon\Delta t}{\Delta}\right)\left[V_{k+1}^{n} - V_{k}^{n}\right] \qquad (2.33)$$

$$V_{k}^{n+1} = V_{k}^{n} - \left(Z_0\right)\left(\frac{\upsilon\Delta t}{\Delta}\right)\left[I_{k+\frac{1}{2}}^{n+\frac{1}{2}} - I_{k-\frac{1}{2}}^{n+\frac{1}{2}}\right] \qquad (2.34)$$

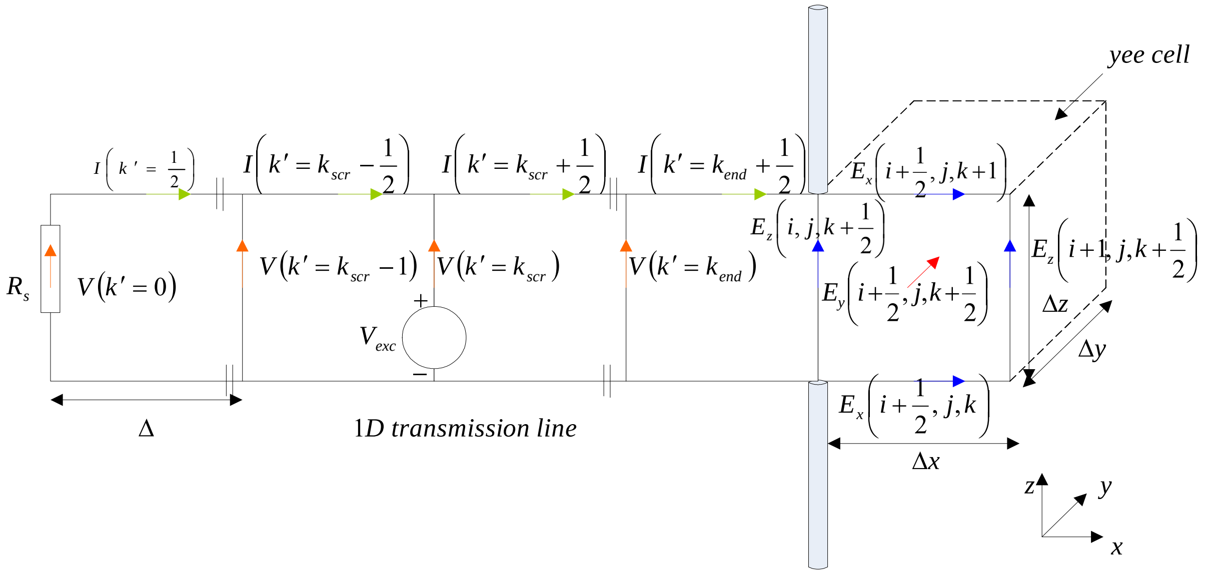

Fig 2.7 Representation of the unidimensional virtual transmission line used to implement the resistive voltage source and coupling to the 3D FDTD grid [19]

Where υ is the phase velocity for the transmission line and;

Δ is the spatial discretization step.

The transmission line is excited at the index $k' = k'_{source}$ source, by adding the value of the excitation signal $V_{exc}(t)$ to the voltage value already present on the line, corresponding to the following update relation:

$$V_{k'_{source}}^{n+1} = V_{k'_{source}}^{n} - Z_0\left(\frac{\upsilon\Delta t}{\Delta}\right)\left[I_{k'_{source}+\frac{1}{2}}^{n+\frac{1}{2}} - I_{k'_{source}-\frac{1}{2}}^{n+\frac{1}{2}}\right] + V_{exc}^{n+1} \qquad (2.35)$$

For the current, it is

$$I^{n+1}_{k'_{source}+\frac{1}{2}} = I^{n}_{k'_{source}+\frac{1}{2}} - \frac{1}{Z_0}\left(\frac{\upsilon\Delta t}{\Delta}\right)\left[V^{n+\frac{1}{2}}_{k'_{source}+1} - V^{n+\frac{1}{2}}_{k'_{source}}\right] + V^{n+1}_{exc} \tag{2.36}$$

The coupling between the virtual transmission line and the FDTD lattice is perfumed as follows: The voltage at the end of the line, which corresponds to index $k_0$end, is converted to an electric field E_{inc} by dividing it by the cell's length along the field's direction, which, for the case in figure. 2.7, is Δz, Then, E_{inc} is introduced into the FDTD update equations in the following ways:

- The source is connected to a thin wire. It is necessary to apply thin-wire model update equations to the circulating H-fields, here exemplified for the H_y component:

$$\begin{aligned} H_y\Big|^{n+\frac{1}{2}}_{i+\frac{1}{2},j,k+\frac{1}{2}} &= H_y\Big|^{n-\frac{1}{2}}_{i+\frac{1}{2},j,k+\frac{1}{2}} + \frac{\Delta t}{\mu\Delta z}\left(E_x\Big|_{i+\frac{1}{2},j,k} - E_x\Big|_{i+\frac{1}{2},j,k+1}\right) + \\ &\frac{2\Delta t}{\mu\Delta x\ln(\Delta x/r_0)}\left(E_x\Big|^{n}_{i+\frac{1}{2},j,k} - E_{inc}\Big|^{n}\right) \end{aligned} \tag{2.37}$$

- The coupling between the FDTD lattice and the virtual transmission line is performed by assigning the current calculated from the local magnetic field values to the current at the end of the transmission line $I_{k'_{end}+\frac{1}{2}}$. The current is calculated using the expression;

$$\begin{aligned} I^{n-\frac{1}{2}} &= \left[H_x^{n-\frac{1}{2}}(i_s, j_s-1, k_s+1) - H_x^{n-\frac{1}{2}}(i_s, j_s, k_s+1)\right]\Delta x \\ &+ \left[H_y^{n-\frac{1}{2}}(i_s, j_s, k_s+1) - H_y^{n-\frac{1}{2}}(i_s-1, j_s, k_s+1)\right]\Delta y \end{aligned} \tag{2.38}$$

Calculation input impedance and scattering parameter:

Since the time-domain current and voltage signals at the terminals of the antenna (or other structure connected to the source) are directly accessible, respectively in $I\Big|_{kend+\frac{1}{2}}$ and $V\big|_{kend}$, the input impedance and admittance are calculated as follows:

$$Z_{in}(f)=\frac{DFT\left\{V\big|_{kend}\right\}}{DFT\left\{I\Big|_{kend+\frac{1}{2}}\right\}} \tag{2.39}$$

And

$$S_{11}=\frac{Z_{in}-50}{Z_{in}+50} \tag{2.40}$$

2.3. Absorbing Boundary Conditions

For many applications that require modeling scattering from an object or a radiating antenna situated in free space, it is desired that the scattered or radiated fields propagate into boundless space. Unfortunately, the FDTD computational space is bounded, and when the scattered or radiated fields arrive at the boundary, they are reflected back into the computation space. Therefore, it is necessary to have an absorbing boundary condition (ABC) that absorbs these fields when they arrive at the limits of the FDTD space such that scattering or radiation into boundless free space is at least approximately simulated. There are many of boundary condition can be used by FDTD method, these boundary conditions are:

2.3.1. Perfect Electric Conductor

The term PEC is an acronym for perfect electric conductor, and is used to model a perfectly conductive metal surface. The boundary conditions at a perfect electric conductor require the tangential electric field components to be zero at the boundary. A perfect electric conductor is modeled by simply setting the tangential electric field components equal to zero at every time step, where the perfect electric conductor is located [20]. For example if there is a PEC on one of the surface of Cube *(i, j, k)* in Figure 2.8, the following E field components will be zero at all time-steps:

$$E^{0}_{x(i,j,k+1)}=E^{0}_{x(i,j+1,k+1)}=E^{0}_{y(i,j,k+1)}=E^{0}_{y(i+1,j,k+1)}=0 \tag{2.41}$$

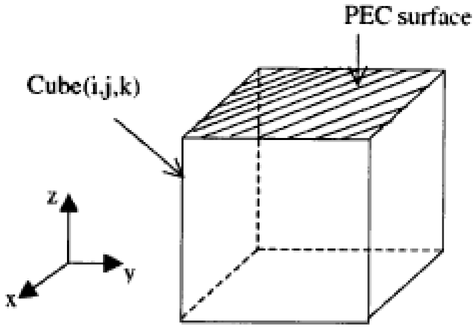

Fig 2.8 PEC on top surface of Cube (i, j, k)[20]

The use of such conditions is used to model conductive surfaces and ground planes.

2.3.2. Mur's Absorbing Boundary Condition

A simple, yet very useful, ABC was proposed by Mur [7]. A first-order Mur condition looks back one step in time and into the space one cell location, while a second-order Mur condition looks back two steps in time and inward two cell locations [7].

Mur's first-order ABC assumes that the waves are normal by incident on the outer mesh walls. This assumption leads to a simple approximate continuous ABC; the tangential fields at the outer boundaries obey the one-dimensional wave equation in the direction normal to the mesh wall.

For the wave normal to the *x* direction

$$\left(\frac{\partial}{\partial x} - \frac{1}{c}\frac{\partial}{\partial t}\right)E_{\tan} = 0 \tag{2.42a}$$

For the wave normal to the *y* direction

$$\left(\frac{\partial}{\partial y} - \frac{1}{c}\frac{\partial}{\partial t}\right)E_{\tan} = 0 \tag{2.42b}$$

For the wave normal to the *z* direction

$$\left(\frac{\partial}{\partial z} - \frac{1}{c}\frac{\partial}{\partial t}\right)E_{\tan} = 0 \tag{2.42c}$$

By considering the E_x and $E_y$components located at $x = i\Delta x$, $j\Delta y$, and $z = nz\ \Delta z$, the first-order Mur estimate at the boundary walls is

$$E_x\Big|_{i,j,nz}^{n+1} = E_x\Big|_{i,j,nz-1}^{n} + \frac{c\Delta t - \Delta z}{c\Delta t + \Delta z}\left(E_x\Big|_{i,j,nz-1}^{n+1} - E_x\Big|_{i,j,nz}^{n}\right) \tag{2.43a}$$

$$E_y\Big|_{i,j,nz}^{n+1} = E_y\Big|_{i,j,nz-1}^{n} + \frac{c\Delta t - \Delta z}{c\Delta t + \Delta z}\left(E_y\Big|_{i,j,nz-1}^{n+1} - E_y\Big|_{i,j,nz}^{n}\right) \tag{2.43b}$$

By considering the E_x and $E_y$components located at $x = i\Delta x$, $y = j\Delta y$, and $z = 0$, the first-order Mur estimate at the boundary walls is

$$E_x\Big|_{i,j,0}^{n+1} = E_x\Big|_{i,j,1}^{n} + \frac{c\Delta t - \Delta z}{c\Delta t + \Delta z}\left(E_x\Big|_{i,j,1}^{n+1} - E_x\Big|_{i,j,0}^{n}\right) \tag{2.43c}$$

$$E_y\Big|_{i,j,0}^{n+1} = E_y\Big|_{i,j,1}^{n} + \frac{c\Delta t - \Delta z}{c\Delta t + \Delta z}\left(E_y\Big|_{i,j,1}^{n+1} - E_y\Big|_{i,j,0}^{n}\right) \tag{2.43d}$$

By considering the E_y and E_z components located at $x = nx\ \Delta x$, $y = j\Delta y$, and $z = k\Delta z$, the first-order Mur estimate at the boundary walls is:

$$E_y\Big|_{nx,j,k}^{n+1} = E_y\Big|_{nx-1,j,k}^{n} + \frac{c\Delta t - \Delta x}{c\Delta t + \Delta x}\left(E_y\Big|_{nx-1,j,k}^{n+1} - E_y\Big|_{nx,j,k}^{n}\right) \tag{2.43e}$$

$$E_z\Big|_{nx,j,k}^{n+1} = E_z\Big|_{nx-1,j,k}^{n} + \frac{c\Delta t - \Delta x}{c\Delta t + \Delta x}\left(E_z\Big|_{nx-1,j,k}^{n+1} - E_z\Big|_{nx,j,k}^{n}\right) \tag{2.43f}$$

By considering the E_y and E_z components located at x = 0, y = jΔy, and z= $k\Delta z$, the first-order Mur estimate at the boundary walls is:

$$E_y\Big|_{0,j,k}^{n+1} = E_y\Big|_{1,j,k}^{n} + \frac{c\Delta t - \Delta x}{c\Delta t + \Delta x}\left(E_y\Big|_{1,j,k}^{n+1} - E_y\Big|_{0,j,k}^{n}\right) \tag{2.43g}$$

$$E_z\Big|_{0,j,k}^{n+1} = E_z\Big|_{1,j,k}^{n} + \frac{c\Delta t - \Delta x}{c\Delta t + \Delta x}\left(E_z\Big|_{1,j,k}^{n+1} - E_z\Big|_{0,j,k}^{n}\right) \tag{2.43h}$$

By considering the $E_x$and E_z components located at $x = i\Delta x$, $y = ny\ \Delta y$, and $z = k\Delta z$, the first-order Mur estimate at the boundary walls is

$$E_x\Big|_{i,ny,k}^{n+1} = E_x\Big|_{i,ny-1,k}^{n} + \frac{c\Delta t - \Delta y}{c\Delta t + \Delta y}\left(E_x\Big|_{i,ny-1,k}^{n+1} - E_x\Big|_{j,ny,k}^{n}\right) \tag{2.43i}$$

$$E_z\Big|_{i,ny,k}^{n+1} = E_z\Big|_{i,ny-1,k}^{n} + \frac{c\Delta t - \Delta y}{c\Delta t + \Delta y}\left(E_z\Big|_{i,ny-1,k}^{n+1} - E_z\Big|_{i,ny,k}^{n}\right) \tag{2.43j}$$

By considering the E_x and E_z components located at $x = i\Delta x$, $y = 0$, and $z = k\Delta z$, the first-order Mur estimate at the boundary walls is

$$E_x\Big|_{i,0,k}^{n+1} = E_x\Big|_{i,1,k}^{n} + \frac{c\Delta t - \Delta y}{c\Delta t + \Delta y}\left(E_x\Big|_{i,1,k}^{n+1} - E_x\Big|_{i,0,k}^{n}\right) \tag{2.43k}$$

$$E_z\Big|_{i,0,k}^{n+1} = E_z\Big|_{i,1,k}^{n} + \frac{c\Delta t - \Delta y}{c\Delta t + \Delta y}\left(E_z\Big|_{i,1,k}^{n+1} - E_z\Big|_{i,0,k}^{n}\right) \tag{2.43l}$$

In other words, the tangential electric field on the artificial boundary wall can be obtained from the previous value of that field, and the field components one node inside of the mesh wall in the current and the next time step.

To implement the first-order Mur ABC, the normal components of the electric field at the boundary walls are obtained using the regular Yee algorithm. The tangential components of the electric field at the intersection of two of the terminating planes (boundary walls) are obtained by taking the average of the values of that component around the specific point.

The second-order absorbing boundary condition for a wave normal to the *x*-constant plane is

$$\left[\frac{1}{c}\frac{\partial^2}{\partial x \partial t} + \frac{1}{c^2}\frac{\partial^2}{\partial t^2}\frac{1}{2}\left(\frac{\partial^2}{\partial x^2} - \frac{\partial^2}{\partial y^2}\right)\right]E_{\tan} = 0 \tag{2.44}$$

Hence, the second-order estimate for E_z at the boundary $x = 0$ is

$$E_z\Big|_{0,j,k}^{n+1} = -E_z\Big|_{1,j,k}^{n-1} + EQ_1 + EQ_2 + EQ_3 + EQ_4 \tag{2.45}$$

where

$$EQ_1 = \frac{c\Delta t - \Delta x}{c\Delta t + \Delta x}\left(E_z\Big|_{1,j,k}^{n+1} + E_z\Big|_{0,j,k}^{n-1} \right) \tag{2.46a}$$

$$EQ_2 = \frac{2\Delta x}{c\Delta t + \Delta x}\left(E_z\Big|_{0,j,k}^{n+1} + E_z\Big|_{1j,k}^{n-1} \right) \tag{2.46b}$$

$$EQ_3 = \frac{\Delta x (c\Delta t)^2}{(c\Delta t + \Delta x)2(\Delta y)^2}\left(C_a + C_b \right) \tag{2.46c}$$

$$EQ_4 = \frac{\Delta x (c\Delta t)^2}{(c\Delta t + \Delta x)2(\Delta z)^2}\left(C_c + C_d \right) \tag{2.46d}$$

and

$$C_a = E_z\Big|_{0,j+1,k}^{n} - 2E_z\Big|_{0,j,k}^{n} + E_z\Big|_{0,j-1,k}^{n} \tag{2.46e}$$

$$C_b = E_z\Big|_{1,j+1,k}^{n} - 2E_z\Big|_{1,j,k}^{n} + E_z\Big|_{1,j-1,k}^{n} \tag{2.46f}$$

$$C_c = E_z\Big|_{0,j,k+1}^{n} - 2E_z\Big|_{0,j,k}^{n} + E_z\Big|_{0,j,k-1}^{n} \tag{2.46g}$$

$$C_d = E_z\Big|_{1,j,k+1}^{n} - 2E_z\Big|_{1,j,k}^{n} + E_z\Big|_{1,j,k-1}^{n} \tag{2.46h}$$

While the second-order estimate for Ez at the boundary $x = n\,\Delta x$ is

$$E_z\Big|_{nx,j,k}^{n+1} = -E_z\Big|_{nx-1,j,k}^{n-1} + EQ_1 + EQ_2 + EQ_3 + EQ_4 \tag{2.47}$$

where

$$EQ_1 = \frac{c\Delta t - \Delta x}{c\Delta t + \Delta x}\left(E_z\Big|_{nx-1,j,k}^{n+1} + E_z\Big|_{nx,j,k}^{n-1} \right) \tag{2.48a}$$

$$EQ_2 = \frac{2\Delta x}{c\Delta t + \Delta x}\left(E_z\Big|_{nx,j,k}^{n+1} + E_z\Big|_{nx-1,j,k}^{n-1} \right) \tag{2.48b}$$

$$EQ_3 = \frac{\Delta x (c\Delta t)^2}{(c\Delta t + \Delta x)2(\Delta y)^2}\left(C_a + C_b \right) \tag{2.48c}$$

$$EQ_4 = \frac{\Delta x (c\Delta t)^2}{(c\Delta t + \Delta x)2(\Delta z)^2}\left(C_c + C_d \right) \tag{2.48d}$$

and

$$C_a = E_z\Big|_{nx,j+1,k}^{n} - 2E_z\Big|_{nx,j,k}^{n} + E_z\Big|_{nx,j-1,k}^{n} \tag{2.48e}$$

$$C_b = E_z\Big|_{nx-1,j+1,k}^{n} - 2E_z\Big|_{nx-1,j,k}^{n} + E_z\Big|_{nx-1,j-1,k}^{n} \tag{2.48f}$$

$$C_c = E_z\Big|_{nx,j,k+1}^{n} - 2E_z\Big|_{nx,j,k}^{n} + E_z\Big|_{nx,j,k-1}^{n} \tag{2.48g}$$

$$C_d = E_z\Big|_{nx-1,j,k+1}^{n} - 2E_z\Big|_{nx-1,j,k}^{n} + E_z\Big|_{nx-1,j,k-1}^{n} \tag{2.48h}$$

The equations needed to determine other field components with second-order Mur estimate at other limiting surfaces of the FDTD space are determined by modification of the proceeding expressions. One important consideration for implementing the second-order Mur ABC is that because the second order estimate requires field values from adjacent Yee cells, it cannot be used for determining electric field values that are adjacent to the intersection of two of the terminating planes (boundary walls).

Therefore, even if second-order Mur is being applied, first-order Mur must be used for field components located at the edges of the problem space. For Mur's ABCs, the farther from the object the outer boundary is located; the better is the absorption of the outward travelling waves. This is because these waves become more like plane waves as they travel farther from the structure that radiates them. However, the number of cells that can be placed between the object and the outer boundary is limited by computer memory. Moving the outer boundary too close to the object may cause instabilities in the absorbing boundary implementation. Also, some fields that are required for an accurate solution may be absorbed if the outer boundary is too close to the object.

2.4. Near-to-Far-Field Transformation

2.4.1. Introduction

The FDTD method accurately computes the electromagnetic field within a computational domain that surrounds the structure of interest, being able to directly calculate near-field quantities such as scattering parameters and impedance/admittance matrices. However, for far-field quantities such as radiation patterns and gain, it is normally impossible to extend the computational domain to the far-field zone, due to the (presently) impractical amount of memory and computer-time required for such a simulation. This difficulty can be overcome quite elegantly by employing a near-to-far-field transformation (NFFT).

There are two well-known near-to-far field transformation techniques: The first one [12] invokes Huygens's principle [24] and uses equivalent magnetic M and electric J currents tangential to a virtual surface that completely encloses the antenna, but is inside the computational domain. Then the equivalent currents are integrated with the free-space Green's function weighting to obtain far-field quantities. The second technique [19] also relies on the use of a virtual surface enclosing the antenna, but the far-field quantities are obtained by means of the primitive Kirchhoff's surface integral representation, avoiding the use of the equivalent currents M and J. For this work, the first approach was chosen because, although both techniques yield good results, the first is better documented and has already been successfully used in numerous applications.

The chosen near-to-far field transformation has two versions: one for time-domain and other for frequency-domain, each with its advantages and limitations. On the one hand, the time-domain version allows the obtaining of the full transient far-field waveforms at a reduced number of observation points, which can then be transformed to the frequency-domain with a FFT to obtain broadband frequency results. On the other hand, the frequency-domain version allows the calculation of the far-fields for a reduced number of frequencies at a number of points sufficiently large to produce a radiation pattern with good resolution in either two- or three-dimensions. In this work we use the frequency domain.

2.4.2. Frequency-Domain Transformation

The frequency domain near to far field transformation uses equivalent magnetic M and electric J currents in phasor form lying on a virtual surface enclosing the antenna to calculate the far fields. Since the computational domain is discretized using cartesian cells, and because

the virtual surface can have an arbitrary shape to enclose the antenna, as shown in Figures 2.9 and 2.10.

2.4.2.1. Equivalent principle

Schelkunoff states the equivalent principle as [15]: "a distributed of electric and magnetic currents on a given surface S can be found such that outside S, it produces the same field as that produced by given sources inside S; and also the field inside S is the same as that produced by given sources outsider S. One of these systems of sources can be identically zero".

The application of the equivalence principle in an FDTD mesh and calculation of the far field radiation characteristics is shown in figure, whereby the radiating antenna and scatters are contained within a virtual box which is fully contained within the FDTD simulation space.

The equivalent surface currents induced on this surface are calculated at each time step during the FDTD simulation. These may be either in the time-domain or frequency-domain, depending on the method used for the far field transformation. Generally, the FDTD ABC is a few cells distant from the virtual box boundaries to reduce, if not eliminate any interactions with the ABC [20].

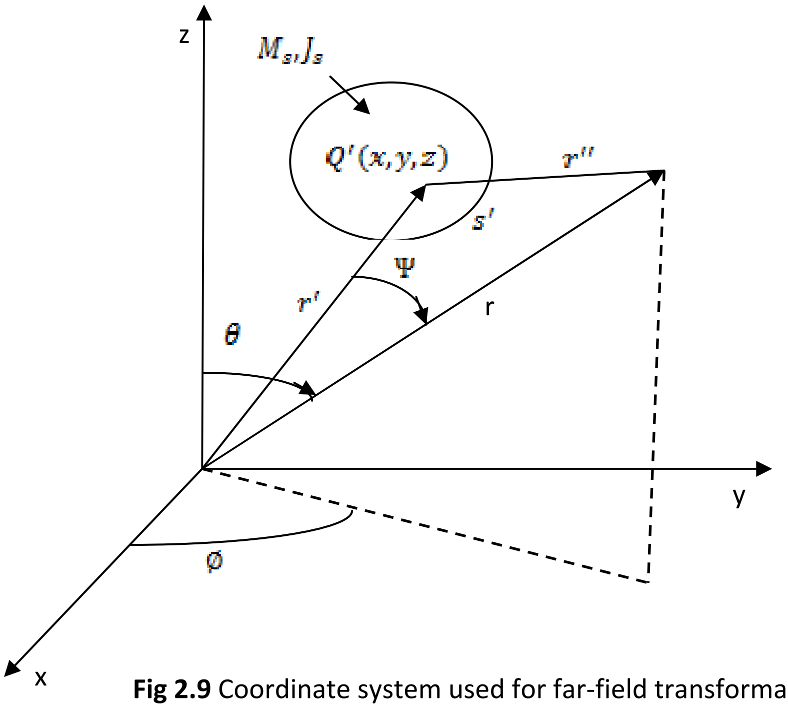

Fig 2.9 Coordinate system used for far-field transformation [19]

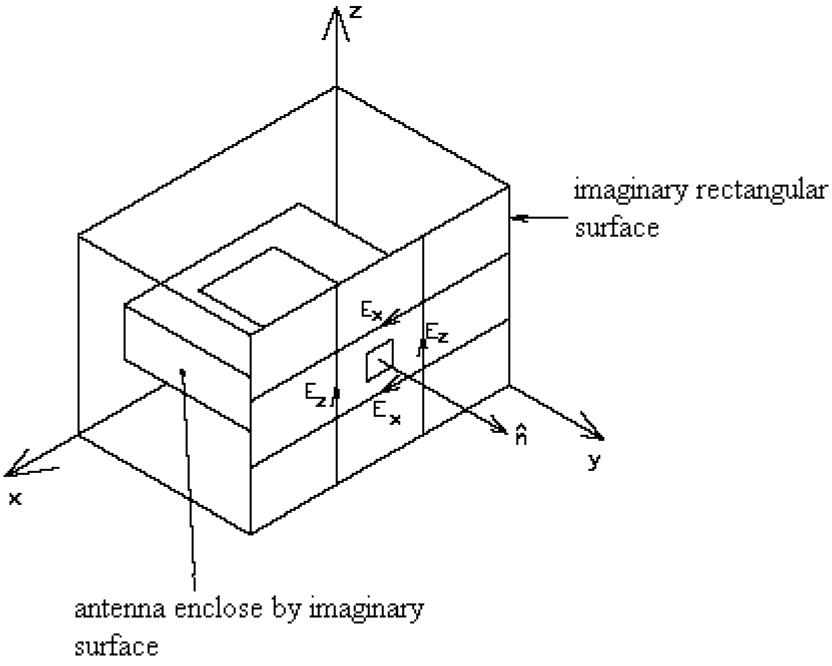

Fig 2.10 FDTD model for a patch antenna mounted on a small ground plane and enclosed in an imaginary surface [22]

2.4.2.2. Analytical expressions for the transformation

To obtain the far-field information from the equivalent currents, it is necessary to integrate them over each of the six faces of the virtual box, here designated by surface S. This integration can be done by using the following pair of vector potentials [19]:

$$\overline{A} = \frac{\mu_0}{4\pi} \iint_s \overline{J}_S \frac{e^{-jkR}}{R} dS \cong \frac{\mu_0 e^{-jkr}}{4\pi r} \overline{N} \tag{2.49}$$

$$\overline{F} = \frac{\varepsilon_0}{4\pi} \iint_s \overline{M}_S \frac{e^{-jkR}}{R} dS \cong \frac{\varepsilon_0 e^{-jkr}}{4\pi r} \overline{L} \tag{2.50}$$

Where

$$\overline{N} = \iint_s \overline{J}_S e^{jkr' \cos\psi} dS \tag{2.51}$$

$$\overline{L} = \iint_s \overline{M}_S e^{jkr' \cos\psi} dS \tag{2.52}$$

and

$\overline{r} = r\hat{r} \equiv$ Position of the observation point (x, y, z)

$\overline{r'} = r'\hat{r}' \equiv$ Position of the source point on $S(x_0, y_0, z_0)$

$\overline{R} = R\hat{R} \equiv \overline{r} - \overline{r'}$

$\psi \equiv$ Angle between $\overline{r}$ and $\overline{r'}$

R is given by the law of cosines in the far-field as

$$R = [r^2 + (r')^2 2rr'\cos\psi]^{-1/2} \cong \{\begin{cases} r - r'\cos\psi & \text{for phase variations} \\ r & \text{for amplitude variation} \end{cases} \qquad (2.53)$$

The $\overline{E}$ and $\overline{H}$ fields due to the vector potentials (2.47) and (2.48) are given by

$$\overline{E} = -jw\left[\overline{A} + \frac{1}{k^2}\nabla(\nabla \cdot \overline{A})\right] - \frac{1}{\varepsilon_0}\nabla \times \overline{F} \qquad (2.54)$$

$$\overline{H} = -jw\left[\overline{F} + \frac{1}{k^2}\nabla(\nabla \cdot \overline{F})\right] + \frac{1}{\mu_0}\nabla \times \overline{A} \qquad (2.55)$$

Since observations are made in the far-field, the dominant variation is of the order $1/r$ and thus the terms in (2.52) and (2.53) that have variations of the order $1/r^2, 1/r^3$, $1/r^4$, etc. can be neglected in order to simplify the expressions. Moreover, taking into account that in the far-field region only the θ and ϕ components are dominant, the E-field and H-field components are given, in spherical coordinates, by

$$\overline{E_\theta} \cong -jw\left(\overline{A_\theta} + \eta_0 \overline{F_\phi}\right) = -\frac{jke^{-jkr}}{4\pi r}\left(\overline{L_\phi} + \eta_0 \overline{N_\theta}\right) \qquad (2.56)$$

$$\overline{E_\phi} \cong -jw\left(\overline{A_\phi} - \eta_0 \overline{F_\theta}\right) = +\frac{jke^{-jkr}}{4\pi r}\left(\overline{L_\theta} - \eta_0 \overline{N_\phi}\right) \qquad (2.57)$$

$$\overline{H_\theta} \cong +\frac{jw}{\eta_0}\left(\overline{A_\phi} - \eta_0 \overline{F_\theta}\right) = +\frac{jke^{-jkr}}{4\pi r}\left(\overline{N_\phi} - \frac{\overline{L_\theta}}{\eta_0}\right) \qquad (2.58)$$

$$\overline{H_\phi} \cong -\frac{jw}{\eta_0}\left(\overline{A_\theta} + \eta_0 \overline{F_\phi}\right) = -\frac{jke^{-jkr}}{4\pi r}\left(\overline{N_\theta} + \frac{\overline{L_\phi}}{\eta_0}\right) \qquad (2.59)$$

Where $\eta_0 = \sqrt{\mu_0 / \varepsilon_0}$ is the intrinsic impedance of free space.

The θ and ϕ components of the vector phasors $\overline{N}$ and $\overline{L}$ are given by:

$$\overline{N_\theta} = \iint_S \left(\overline{J_x}\cos\theta\cos\phi + \overline{J_y}\cos\theta\sin\phi - \overline{J_z}\sin\theta\right)e^{jkr'\cos\psi}\,dS \qquad (2.60)$$

$$\overline{N_\phi} = \iint_S \left(-\overline{J_x}\sin\phi + \overline{J_y}\cos\phi\right) e^{jkr'\cos\psi}\, dS \qquad (2.61)$$

$$\overline{L_\theta} = \iint_S \left(\overline{M_x}\cos\theta\cos\phi + \overline{M_y}\cos\theta\sin\phi - \overline{M_z}\sin\theta\right) e^{jkr'\cos\psi}\, dS \qquad (2.62)$$

$$\overline{L_\theta} = \iint_S \left(-\overline{M_x}\sin\phi + \overline{M_y}\sin\phi\right) e^{jkr'\cos\psi}\, dS \qquad (2.63)$$

These integral expressions can be numerically evaluated for each of the six faces that form the virtual box S. Considering, for instance, that S is a rectangular box of side dimensions $2x_0$, $2y_0$, $2z_0$ centered in the origin of the coordinate system, the integrals (2.60),(2.61),(2.62) and (2.63) can be particularized for each pair of opposite faces as follows:

- **Faces at :** $x = \pm x_0$ **:**

- Nonzero components of: $\overline{J}_s and \overline{M}_s : \overline{J}_y, \overline{J}_z, \overline{M}_y$ and $\overline{M}_z$

- Exponential phase term:

$$r'\cos\psi = r'\cdot\hat{r}$$

$$= \left(\pm x_0\hat{x} + y\hat{y} + z\hat{z}\right)\cdot\left(\hat{x}\sin\theta\cos\phi + \hat{y}\sin\theta\sin\phi + \hat{z}os\theta\right)$$

$$= \pm x\sin\theta\cos\phi + y\sin\theta\sin\phi + zos\theta$$

- Integration limits : $-y_0 \le y \le y_0, -z_0 \le z \le z_0, dS = dydz$

- **Faces at :** $y = \pm y_0$ **:**

- Nonzero components of: $\overline{J}_s and \overline{M}_s :\ \overline{J}_x, \overline{J}_z, \overline{M}_x$ and $\overline{M}_z$

- Exponential phase term:

$$r'\cos\psi = r'\cdot\hat{r}$$

$$= \left(\pm x\hat{x} + y_0\hat{y} + z\hat{z}\right)\cdot\left(\hat{x}\sin\theta\cos\phi + \hat{y}\sin\theta\sin\phi + \hat{z}os\theta\right)$$

$$= x\sin\theta\cos\phi \pm y_0 \sin\theta\sin\phi + zos\theta$$

- Integration limits: $-x_0 \le y \le x_0, -z_0 \le z \le z_0, dS = dxdz$

- **Faces at :** $z = \pm z_0$ **:**

- Nonzero components of : $m\Delta f., \overline{J}_x, \overline{J}_y, \overline{M}_x$ and $\overline{M}_y$

- Exponential phase term:

$$r'\cos\psi = r'\cdot\hat{r}$$

$$= (x\hat{x} + y\hat{y} \pm z_0\hat{z})\cdot(\hat{x}\sin\theta\cos\phi + \hat{y}\sin\theta\sin\phi + \hat{z}os\theta)$$

$$= x\sin\theta\cos\phi + y\sin\theta\sin\phi \pm z_0 os\theta$$

- Integration limits: $-x_0 \le x \le x_0, -y_0 \le y \le y_0, dS = dxdy$

The time-averaged Pointing vector’s radial component at a point (r,θ,ϕ) is given by:

$$S_{av}(r,\theta,\phi) = \frac{1}{2}\mathrm{Re}\left(\overline{E}_\theta \overline{H}_\phi^*\right) + \frac{1}{2}\mathrm{Re}\left(-\overline{E}_\phi \overline{H}_\theta^*\right)$$

$$= \frac{k^2}{32\pi^2\eta_0 r^2}\left(\left|\overline{L}_\phi + \eta_0\overline{N}_\theta\right|^2 + \left|\overline{L}_\theta - \eta_0\overline{N}_\phi\right|^2\right) \tag{2.64}$$

which can be used to calculate the gain $G(\theta,\phi)$ as:

$$G(\theta,\phi) = 4\pi r^2\frac{S_{av}}{P_{in}} = \frac{k^2}{8\pi\eta_0 P_{in}}\left(\left|\overline{L}_\phi + \eta_0\overline{N}_\theta\right|^2 + \left|\overline{L}_\theta - \eta_0\overline{N}_\phi\right|^2\right) \tag{2.65}$$

where P_{in} is the antenna input power at the frequency for which the near-to-far-field transformation is being calculated.

2.4.2.3. Calculation of the equivalent M_S and J_S currents

The equivalent currents are calculated from the tangential E and H components at the virtual surface, using the following expressions:

$$\vec{J}_S = \hat{n}\times\vec{H} \tag{2.66a}$$

$$\vec{M}_S = -\hat{n}\times\vec{E} \tag{2.66b}$$

where $\hat{n}$ is the surface normal pointing outside of S. The application of (2.64a) to each of the faces of the box yields:

- Face at $i = i_{\min} : J_y = H_z, J_z = -H_y, M_y = -E_z, M_z = E_y$ (2.67a)
- Face at $i = i_{\max} : J_y = -H_z, J_z = H_y, M_y = E_z, M_z = -E_y$ (2.67b)
- Face at $j = j_{\min} : J_x = -H_z, J_z = H_x, M_x = E_z, M_z = -E_x$ (2.67c)
- Face at $j = j_{\max} : J_x = H_z, J_z = -H_x, M_x = -E_z, M_z = E_x$ (2.67d)
- Face at $k = k_{\min} : J_x = H_y, J_y = -H_x, M_x = -E_y, M_y = E_x$ (2.67e)
- Face at $k = k_{\max} : \quad J_x = -H_y, J_y = H_x, M_x = E_y, M_y = -E_x$ (2.67f)

The i, j, k indices correspond to the actual indices where each virtual surface is located in the Cartesian grid. It is worth to mention that during the implementation of this near-to-far-field transformation it was concluded that the enclosing virtual box should be placed as close as possible to the structure without, however, intersecting it, in order to minimize errors resulting from numerical dispersion.

2.4.2.4. Tangential surface fields

Tangential surface currents on the surface of the virtual box must be averaged in order to obtain the electric or magnetic field in the centre of each respective cell face. This is simple for the electric field, where only two components are required. However, for the magnetic field, four neighbouring field components must be used in order to obtain an accurate approximation in the centre of the cell face. Once these averaged field values are known for each cell face, a DFT is applied to obtain electric and magnetic field phasors on the surface of the virtual box [15].

2.4.2.5. Averaging the electric and magnetic fields

The averaging procedure for each cell face is now discussed. Essentially, three sets of equations are obtained; one set for each virtual box surface normal to the x, y and z axes respectively.

The x axis averaging equations for $X_{\min}$ and $X_{\max}$ for E_y, E_z, H_z and H_y are:

$$E_{yavg} = \frac{E_y(i,j,k) + E_y(i,j,k+1)}{2} \tag{2.68}$$

$$E_{zavg} = \frac{E_z(i,j,k) + E_z(i,j+1,k)}{2} \tag{2.69}$$

$$H_{yavg} = \frac{H_y(i,j,k) + H_y(i,j+1,k) + H_y(i-1,j,k) + H_y(i-1,j+1,k)}{4} \tag{2.70}$$

$$H_{zavg} = \frac{H_z(i,j,k) + H_z(i,j,k+1) + H_z(i-1,j,k) + H_z(i-1,j,k+1)}{4} \tag{2.71}$$

The y axis averaging equations for $Y_{\min}$ and $Y_{\max}$ for E_x, E_z, H_z and H_x are:

$$E_{xavg} = \frac{E_x(i,j,k) + E_x(i,j,k+1)}{2} \tag{2.72}$$

$$E_{zavg} = \frac{E_z(i,j,k) + E_z(i+1,j,k)}{2} \tag{2.73}$$

$$H_{xavg} = \frac{H_x(i,j,k) + H_x(i+1,j,k) + H_x(i,j-1,k) + H_x(i+1,j-1,k)}{4} \tag{2.74}$$

$$H_{zavg} = \frac{H_z(i,j,k) + H_z(i,j,k+1) + H_z(i,j-1,k) + H_z(i,j-1,k+1)}{4} \tag{2. 75}$$

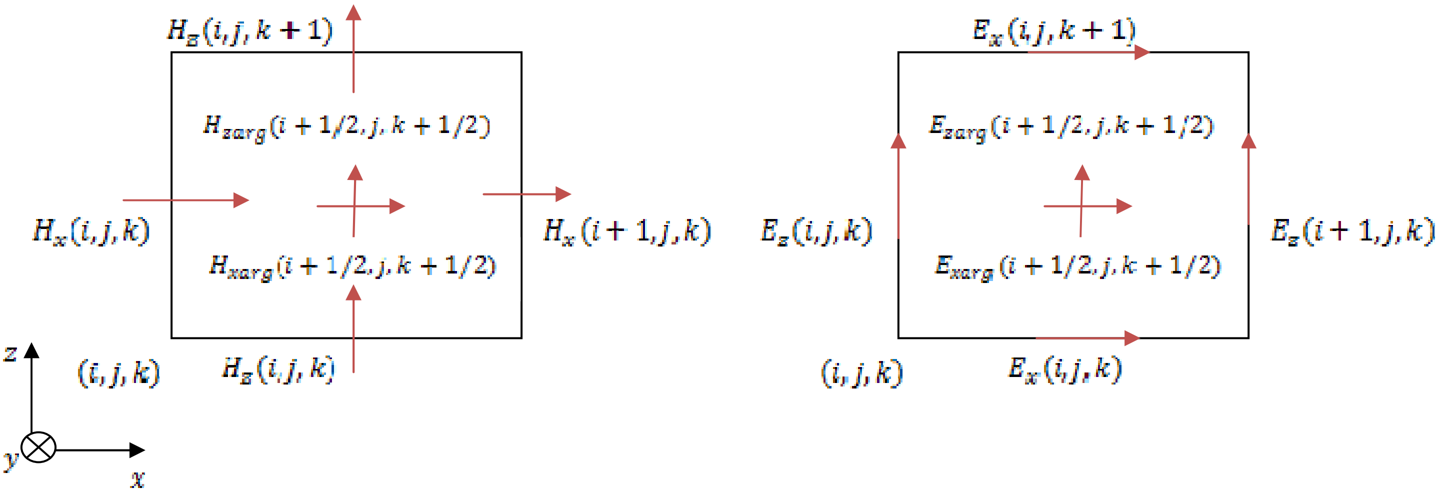

(a) Tangential magnetic fields

(b) Tangential electric fields

Fig 2.12: Averaging of tangential fields on the surface of the virtual box [15]

The z axis averaging equations for $Z_{\min}$ and $Z_{\max}$ for E_x, E_y, H_y and H_x are:

$$E_{xavg} = \frac{E_x(i,j,k) + E_x(i,j+1,k)}{2} \quad (2.76)$$

$$E_{yavg} = \frac{E_y(i,j,k) + E_y(i+1,j,k)}{2} \quad (2.77)$$

$$H_{xavg} = \frac{H_x(i,j,k) + H_x(i+1,j,k) + H_x(i,j,k-1) + H_x(i+1,j,k-1)}{4} \quad (2.78)$$

$$H_{yavg} = \frac{H_y(i,j,k) + H_y(i,j+1,k) + H_y(i,j,k-1) + H_y(i,j+1,k-1)}{4} \quad (2.79)$$

2.5. Discrete Fourier transforms

A running discrete Fourier transform equation is used to obtain the tangential field phasors in the frequency domain on the surface of the virtual box surrounding the scatter. Furse and Gandhi [15] demonstrate that the DFT can be significantly more efficient than a standard FFT in terms of computer resource requirements. The electric field and magnetic field vectors on the surface of the box are recorded at each time step. After the fields have reached steady state values, the time stepping is stopping .the frequency-domain electric field and magnetic field phasors $E(\omega)$ and $H(\omega)$ are then converted into surface currents and $M(\omega)$ the DFT is defined as:

$$F(m\Delta f) = \Delta t \sum_{n=0}^{N_{DFT}-1} g(n\Delta t) e^{\left[\frac{-j2\pi mn}{N_{DFT}}\right]} \qquad m = 0,1,2,.....N_{DFT} - 1 \quad (2.80)$$

$F(m\Delta f)$is the phasors of an equivalent sinusoidal signal at frequency $m\Delta f$. The signal of interest in the time domain is $g(n\Delta t)$.m is the frequency index.

2.6.Copolarization and cross-polarization field components

An antenna is said to have a good polarization purity if the level of the cross-polarization component noted E_{cross} is at least -20 dB lower than the co-polar component, noted E_{co} . The polarization components (cross-polarization and co-polarization) are determined using the Ludwig definition [25].in our case see figure 2.13, that is,

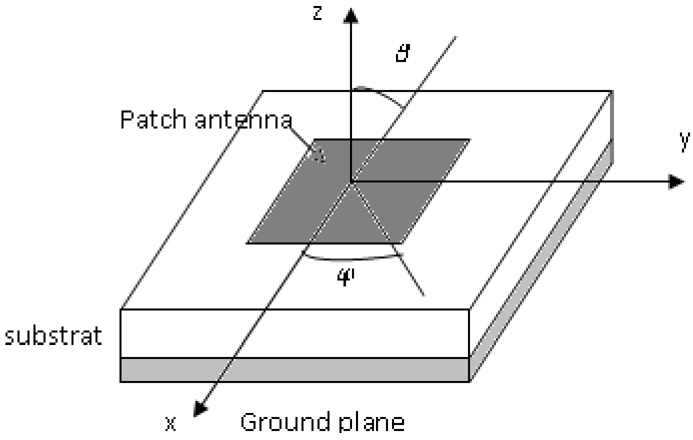

Fig .2.13 typical geometry of microstrip patch antenna

$$E_x = E_{co} = E_\theta \sin\phi - E_\phi \cos\phi \tag{2.81}$$

$$E_y = E_{cross} = E_\theta \sin\phi + E_\phi \cos\phi \tag{2.82}$$

For **E-plane**

In the E-plane (xz plane), defined by $\phi = \frac{\pi}{2}$, the copolarized and the crosspolarized field components become;

$$E_{eco} = E_\theta = -\frac{jke^{-jkr}}{4\pi r}\left(\overline{L_\phi} + \eta_0 \overline{N_\theta}\right) \tag{2.83}$$

$$E_{cross} = -E_\phi = -\frac{jke^{-jkr}}{4\pi r}\left(\overline{L_\theta} - \eta_0 \overline{N_\phi}\right) \tag{2.84}$$

For **H-plane**

In the H-plane (yz plane), defined by $\phi = 0$, the copolarized and the crosspolarized field components become;

$$E_{eco} = E_\theta = -\frac{jke^{-jkr}}{4\pi r}\left(\overline{L_\phi} + \eta_0 \overline{N_\theta}\right) \tag{2.85}$$

$$E_{cross} = E_\phi = \frac{jke^{-jkr}}{4\pi\, r}\left(\overline{L_\theta} - \eta_0 \overline{N_\phi}\right) \tag{2.86}$$

2.7. Bandwidth

The bandwidth of antennas is difficult to define in general terms. Most antenna characteristics, including gain, beam-width, side-lobe level, polarization, and impedance, are functions of frequency, and the variation of each of these parameters may limit the useful frequency band of an antenna designed for a specific purpose. Frequently, the used measures of an antenna bandwidth are the impedance bandwidth, which indicates the frequency band over which the SWR at the circuit port of the antenna remains below a given value.

For the microstrip antennas cases, which are resonant structures, we select the above definition by considering the value of the VSWR to be 2. The determination of the bandwidth is done either by drawing the locus of the normalized impedance as a function of frequency on the Smith chart and noting the intersecting frequencies f_1 and f_2 with the circle SWR=2 or by drawing the VSWR as a function of frequency and reading f_1 and f_2 . The normalizing impedance should be chosen judiciously [26]. Thus, the bandwidth is expressed directly as a function of f_1 and f_2 by the relation [26].

$$B = 200 \times \frac{f_2 - f_1}{f_2 + f_1} \quad \text{(in \%)} \qquad (2.87)$$

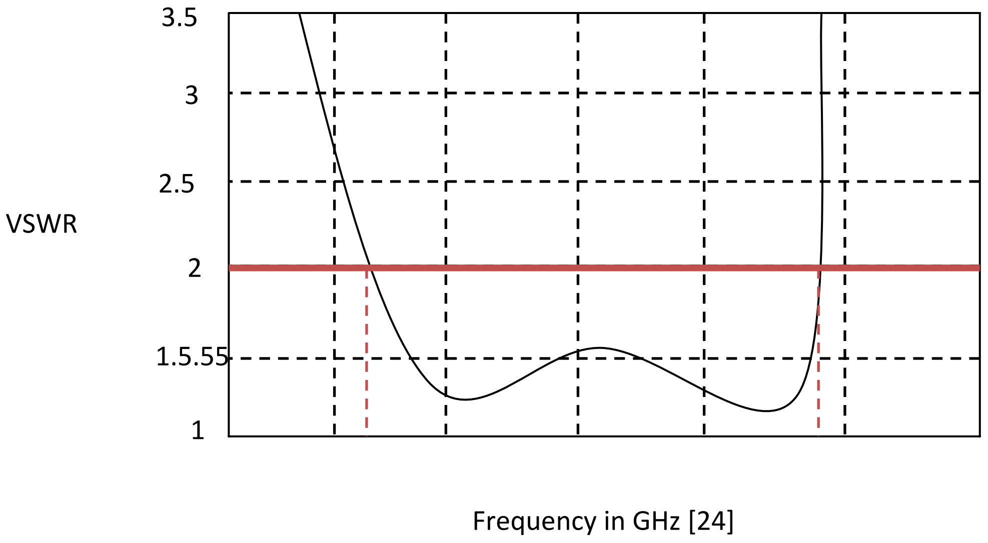

Fig.2.14 Graphical determination of the impedance frequency bandwidth [26]

Chapter III

Numerical results and discussion

3.1. Introduction

In this chapter, the FDTD method is applied to different shapes of microstrip antennas working at relatively high microwave frequencies. From the calculated time domain waveforms of the considered structures, the frequency dependent characteristics of the structures are determined as shown in the coming sections.

3.2. Rectangular microstrip patch antenna

In this section, the analysis of a line-fed rectangular microstrip antenna using FDTD method is discussed. Line-fed microstrip antennas are of interest because they are very easily fabricated. The actual antenna under consideration is shown in the figure 3.1. This patch is of dimensions $8\,mm \times 5\,mm$ on a substrate of thickness $h = 1.59\,mm$ and relative permittivity $\varepsilon_r = 2.32$.

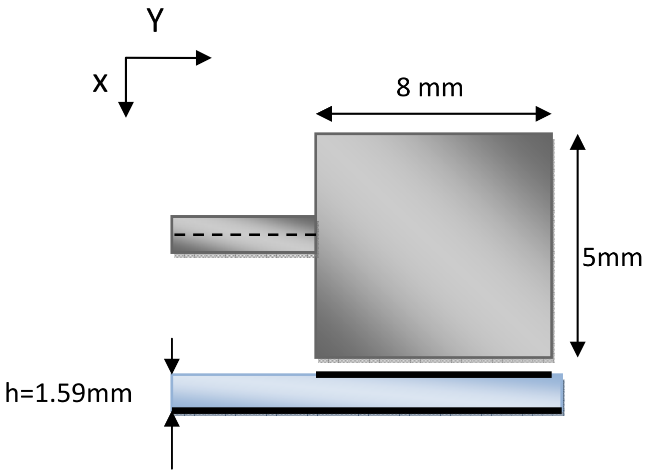

Fig.3.1 Line fed rectangular patch antenna

The space steps used in the FDTD formulation are $\Delta x = 0.1562$ mm, $\Delta y = 0.2$ mm and $\Delta z = 0.53$mm and the size of free space is 50 Δx ×100 Δy × 16 Δz. The time step is taken to be $\Delta t = 0.39998$ *pec* to satisfy the Courant stability condition. The size of the ground plane and the: fed patch are 50 Δx ×100 Δy (7.8125×20 mm) and $30\Delta x \times 40\Delta y$ (8×5 mm), respectively. The length of the microstrip line from the source plane to the front edge of the rectangular patch antenna is $50\ \Delta y$. The reference plane is placed at $40\ \Delta y$ from the edge of the antenna. The microstrip line width is modelled as $6\ \Delta y$. The antenna is excited by a Gaussian pulse with pulse width $T = 15\ psec = 34\ \Delta t$ and is set to be $t_0 = 3\ T$ so that the Gaussian pulse will be:

$$E_z(t) = e^{-\left(\frac{t-180\times10^{-12}}{15\times10^{-12}}\right)^2} (V/m) \tag{3.1}$$

Initially, when t = 0 all fields in the FDTD computational domain are set to zero. The electrical field E is switched ON with a Gaussian pulse which can be launched from approximately 0 underneath the microstrip line at the source plane shown in Figure. 3.1. The Gaussian pulse waveform in time domain is shown in figure 3.2 and will be turned off after it passes the source plane. The number of time steps was chosen such that S_{11}-parameters were settled down and no variations occurred anymore. Simulations were conducted with 3000 time steps.

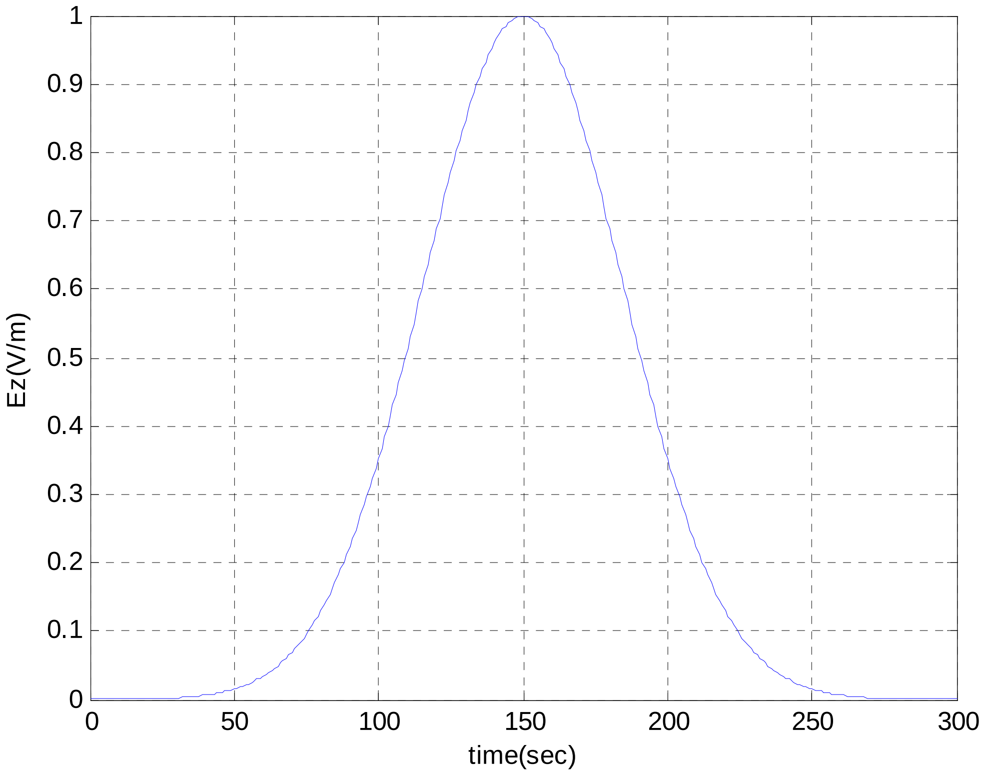

Fig.3.2 Time Domain Gaussian Pulse Waveform used for Excitation of FDTD

The metallization was thought as perfect electric conductors (PEC) and electric fields tangential to the conductors were set as zero. With a dielectric object the boundary condition requires the tangential electric field to be continuous at the boundaries. The value of the dielectric constant at air-substrate interface was calculated as an average of the dielectric constants of the air and dielectric material (as illustrated in chapter II section 2.1.2). The Mur second order absorbing boundary condition was used in the 3D simulation space (boundary of the structure) and the Mur first order in the 1D (feed part, in this section we use improved simple feed model to model transmission line).

Two 1D simulations were run simultaneously. First one simulated the incident field with absorbing boundary conditions (ABC). The second simulation was connected in 3D antenna structures and the reflected voltage signal was stored in memory. The DFT was calculated for both the incident and the reflected signals and the S11-parameter was achieved as a function of frequency by dividing the reflected signal with the incident one.

$$S_{11} = \frac{V_{reflected}}{V_{incident}} \qquad \text{and} \qquad RL = 20\log_{10}|S_{11}| \tag{3.2}$$

3.2.1. Reflection coefficient

The reflection coefficient of rectangular patch antenna using FDTD method and HFSS simulator are depicted together in figure 3.3.

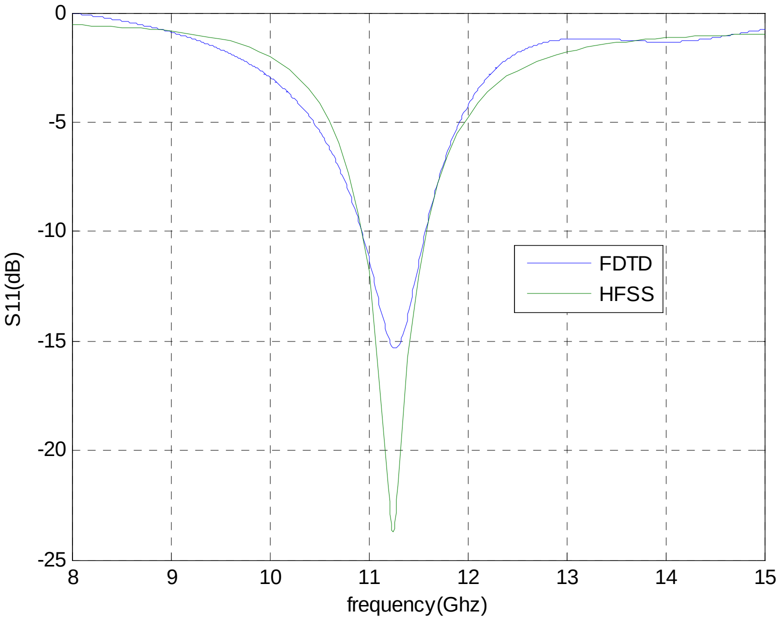

Fig.3.3 Return loss of rectangular patch antenna

W= 5 mm, L = 8 mm, h = 1.59 mm, $\varepsilon_r = 2.32$, the loss tangent $tg(\delta) = 0.002$.

The simulation was stopped at 3500 time steps, It is noticed from the figure 3.3 that the resonance frequency of rectangular patch antenna using FDTD method is 11.20 GHz whereas for HFSS simulator is 11.22 GHz, the difference is about 0.02%, which shows a good result and the capacity of the chosen method in the analysis of the high frequency microstrip radiations structures.

Figure 3.4 shows the real and imaginary part of rectangular patch antenna and the resonant frequency is $f_r = 11.20GHz$. It can be shown that the structure behaves like a tank circuit. And at the resonance, the imaginary part is not null. This may be attributed to the inductance caused by the feeding line which not taken into consideration in the input impedance calculation.

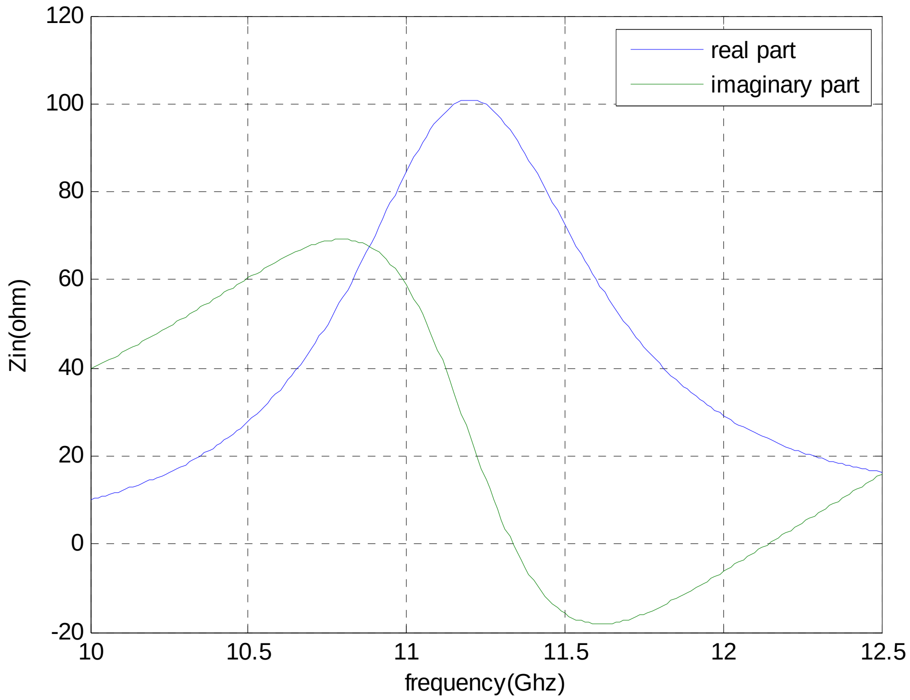

Fig.3.4 The input impedance of rectangular patch antenna using FDTD

3.2.2. Voltage standing wave ratios (VSWR)

The voltage standing wave ratios (VSWR) for rectangular patch antenna using FDTD method is depicted in figure 3.5.

VSWR less than 2 over the frequency interval ranging from 10.85 GHz to 11.65 GHz using FDTD method the calculated bandwidth using equation (2-84) (In chapter II) ,it is found 7.11%; which shows that the structure is narrow band

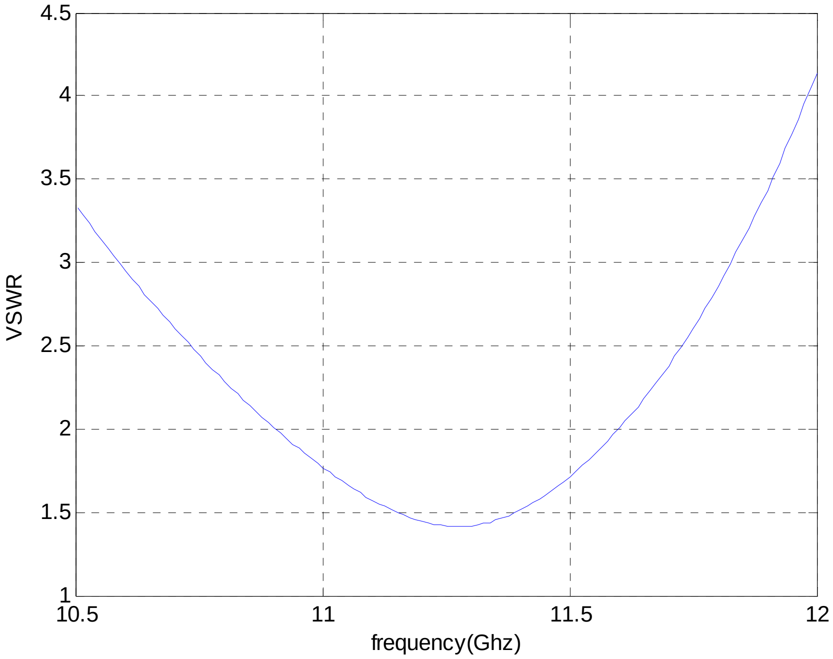

Fig.3.5 The voltage standing wave ratios of rectangular patch antenna using FDTD

. 3.2.3. The far fields

To calculate the radiation pattern of rectangular patch antenna the near field to far field transformation is used (as discussed in chapter II). A sinusoidal excitation at line feed is used, which is given by

$$V(t) = \sin(2\pi f_0 t) \tag{3.3}$$

Where f_0 is the resonant frequency of interest;

Figure 3.6 and 3.7 show the simulated rectangular patch antenna radiation patterns that illustrate far field components (cross and co-polarizations) in E and H planes using FDTD method and compared the obtained results with HFSS simulator at resonance frequency $f_r = 11.20GHz$

In the E-plane co-polarization, the FDTD method and HFSS simulator are similar in shape and symmetric ; as shown in figure 3.6(a), the peak value with FDTD is -0.01 dB at 0°, whereas for HFSS is -0.02 dB at 0°, the difference is 0.01%, this is a good results. The E-plane cross polarization is shown in figure 3.6 (b) ; has a level of -20 dB below the main lobe of the co-polarization field peak value at 0° whereas for HFSS has - 23 dB, the FDTD is broader than HFSS simulator, but it is a good agreement.

For H-plane co-polarization is approximately similar in shape by using FDTD and HFSS simulator as shown in figure 3.7(a), the peak value using FDTD is 0 dB at 0° whereas by using HFSS has -0.01 dB at 0°, which show a good result.

For H-plane cross-polarization is illustrated in figure 3.7(b), the peak value with FDTD is -11.02 dB at 90° and the min is 0 dB at 0.5° whereas for HFSS is -11.20 dB at 90° and min is 0 dB at 0 °. The calculated results (FDTD method) agree well with HFSS simulator results this illustrate that FDTD programs work well.

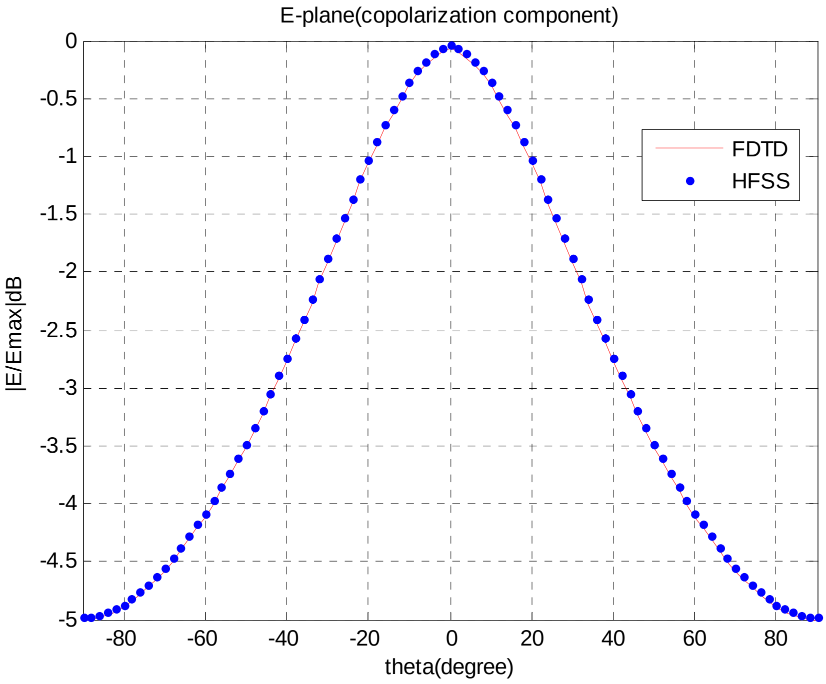

(a)

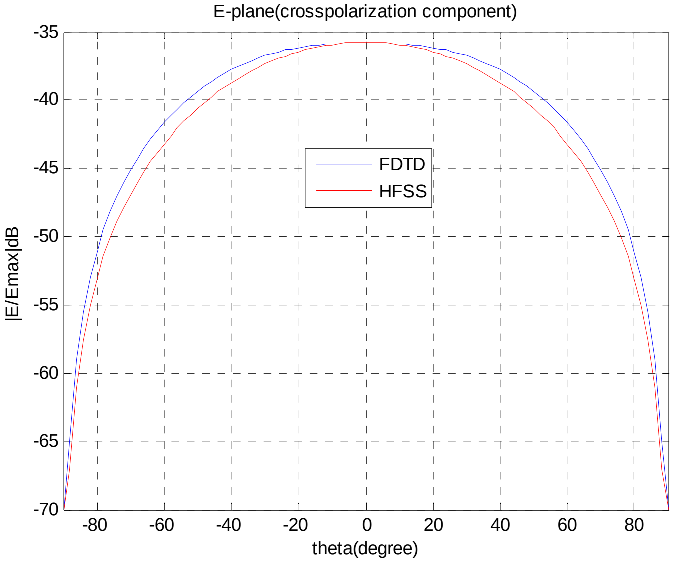

(b)

Fig.3.6 The E-plane radiation pattern of rectangular patch antenna at $f_r = 11.20GHz$

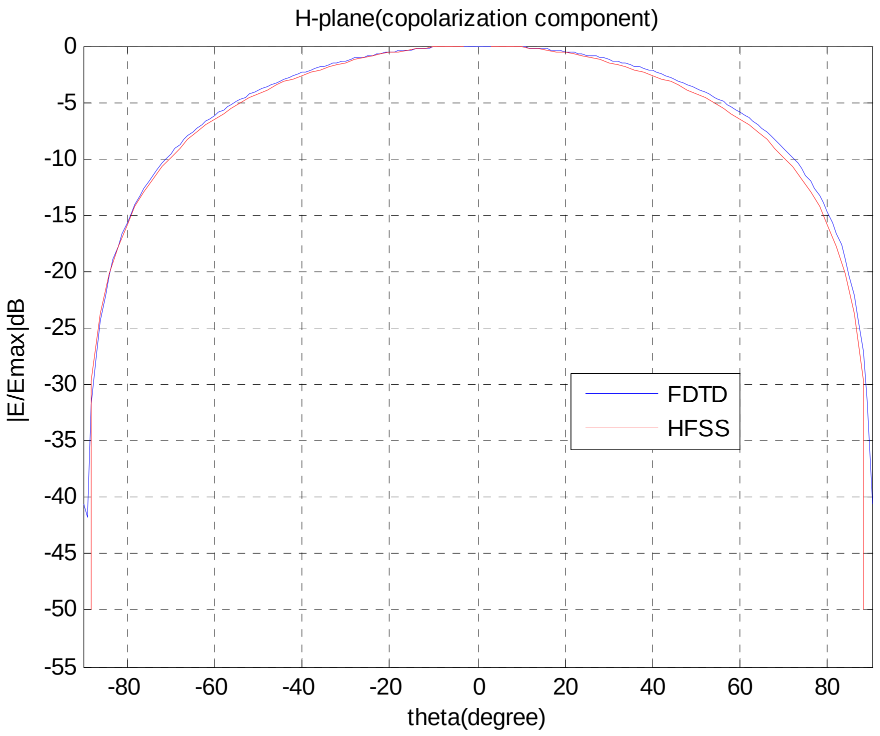

(a)

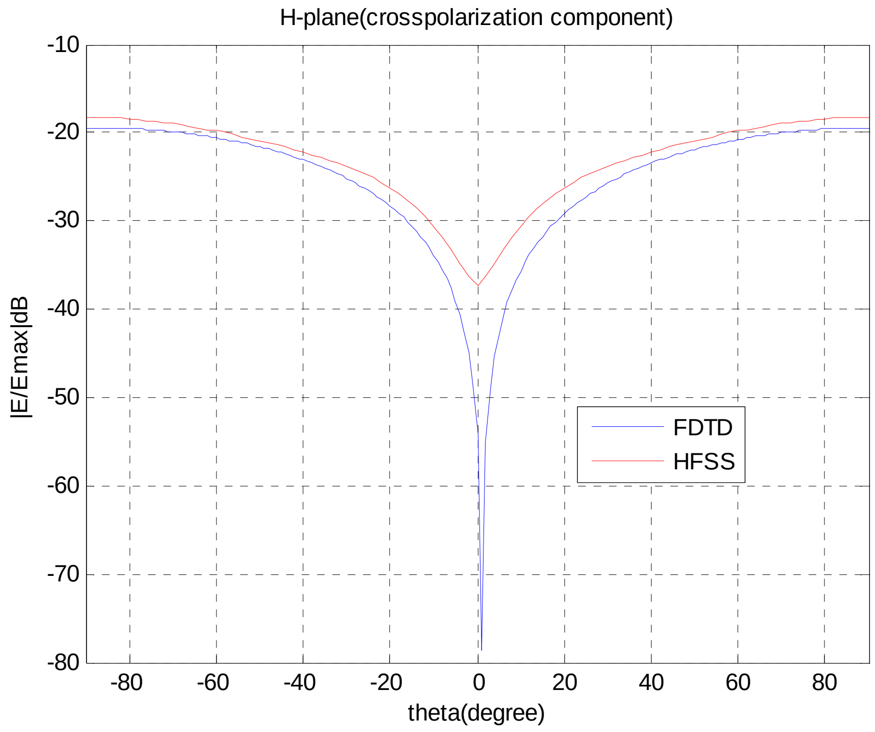

(b)

Fig.3.7 The H-plane radiation pattern of rectangular patch antenna at $f_r = 11.20GHz$

Figure 3.8.shows the total directivity of rectangular patch antenna for $\phi = 0°$ and $\phi = 90°$, at $f_r = 11.20\ GHz$ using HFSS simulator. The directivity is maximum in the $\theta = 0°$ direction and the HFSS shows also the back radiation which is due to imperfections which are not specified to the simulator.

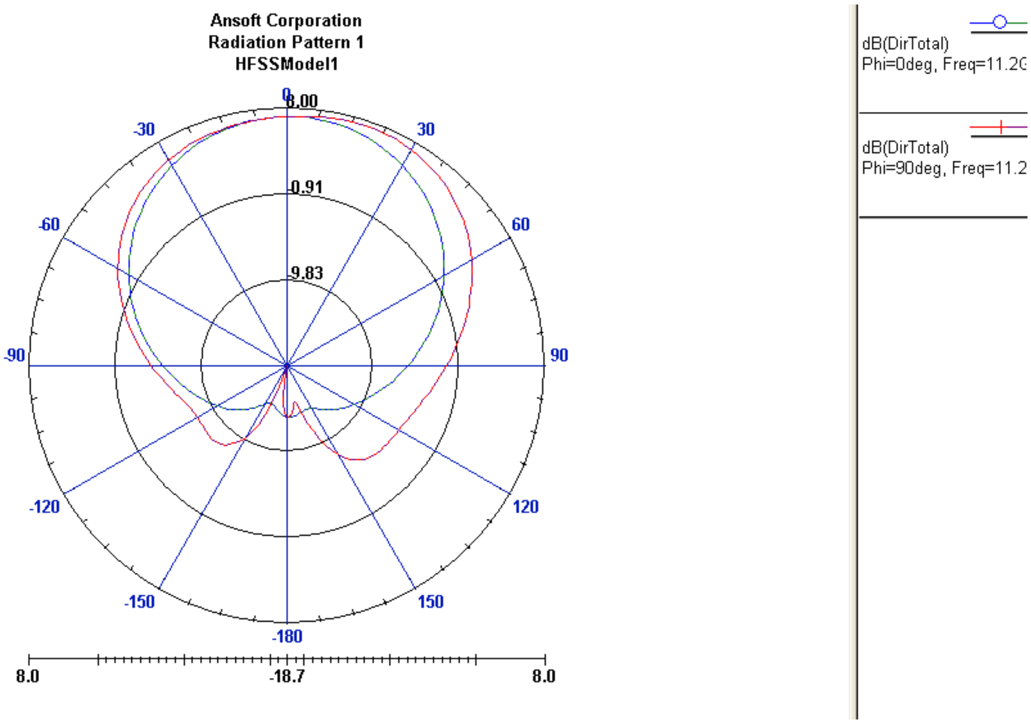

Fig.3.8 Total directivity of rectangular patch antenna at $f_r = 11.20\ GHz$

3.3. Annular ring microstrip patch antenna

In this section, the analysis of a line-fed annular-ring microstrip patch antenna using FDTD method is discussed. This shape is discussed in chapter I and a more detail (see appendix A). This patch is of dimension of outer diameter b = 5 mm and inner diameter a = 2.5 mm on a substrate of thickness h = 1.59 mm and relative permittivity $\varepsilon_r = 2.32$.

The space steps used in the FDTD formulation are $\Delta x = \Delta y = 0.25$ mm and $\Delta z = 0.53$ mm and the size of free space is $60\Delta x \times 75\Delta y \times 20\Delta z$. The time step is taken to be

$\Delta t = 0.55937$ *psec* to satisfy the Courant stability condition. The size of the ground plane and the fed patch are $60\Delta x \times 75\Delta y$ (15 × 18.75 mm) and $40\Delta x \times 40\Delta y$ (10× 10 mm), respectively. The length of the microstrip line from the source plane to the front edge of the annular ring patch antenna is $25\ \Delta y$.

The reference plane is placed at $15\,\Delta y$ from the edge of antenna. The microstrip line width is modelled as $6\,\Delta y\ (1.5\ mm)$. The antenna is excited by a Gaussian pulse with $T = 60\ psec$ and $t_0 = 180\ psec$. The simulation is performed for 4000 time steps.

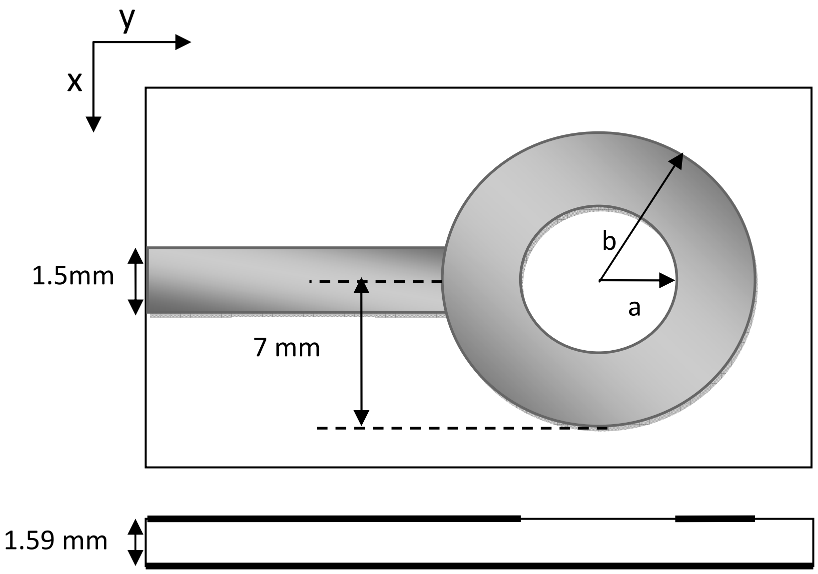

Fig 3.9 line fed annular ring microstrip patch antenna

The boundary conditions are similar to those applied in rectangular patch antenna considered in section (3.2). As it is demonstrated that rectangular gridded FDTD method may be used to accurately analyze curved structures using the stair-step approximation to the curved surfaces [28], analysis of annular-ring patch antenna can be achieved easily. The latter was found to work sufficiently well in this work and did not introduce undesirable distortions in the computed resonance characteristics.

3.3.1. Reflection coefficient and input impedance

Figure 3.10 shows the return loss of annular-ring patch antenna using both FDTD method and HFSS simulator. The resonance frequency obtained with FDTD is 9.30 GHz whereas for HFSS it is 9.35GHz yielding a difference of 0.05% which shows a good agreement.

Figure 3.11 illustrates the real and imaginary parts of the input impedance of the annular-ring patch antenna computed using FDTD method near resonant frequency $f_r = 9.30GHz$. It shows clearly that when the real part is maximum the imaginary part is zero. The maximum real part is $maxR_{in} = 170\ \Omega$. The figure may be explored for matching problem by properly choosing the width of the feeding line. The 170 Ω shows the practical difficulty of matching directly with line width so it is necessary to design either matching network or may be use of probe feed instead of line feed.

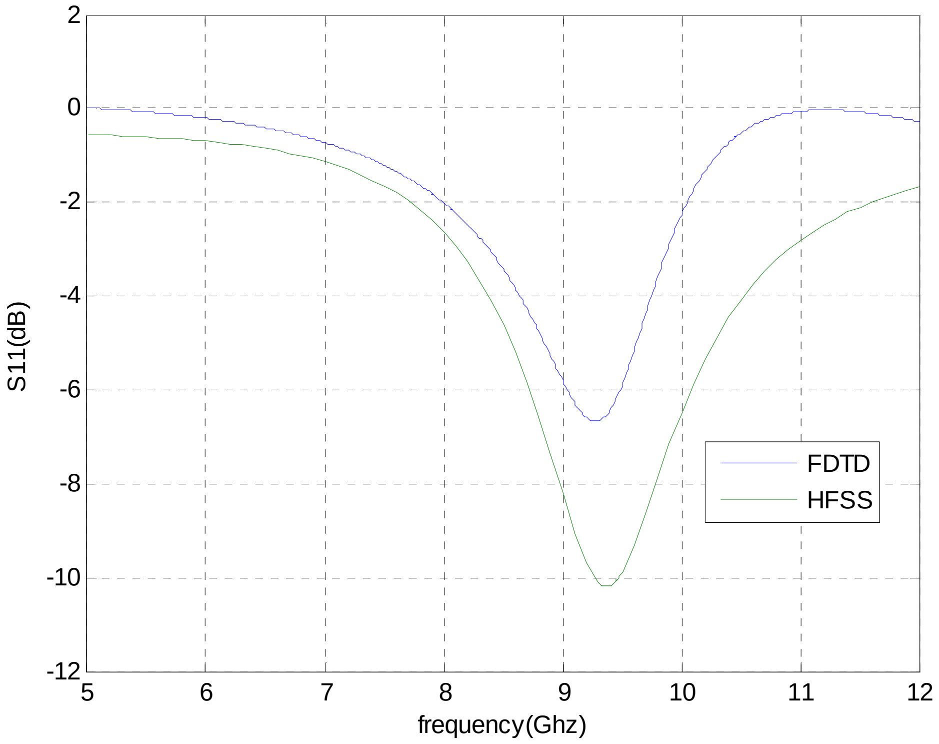

Fig.3.10 Return loss of annular-ring patch antenna

b = 5 mm, a =2.5 mm, h = 1.59 mm, $\varepsilon_r = 2.32$, the loss tangent $tg(\delta) = 0.0002$.

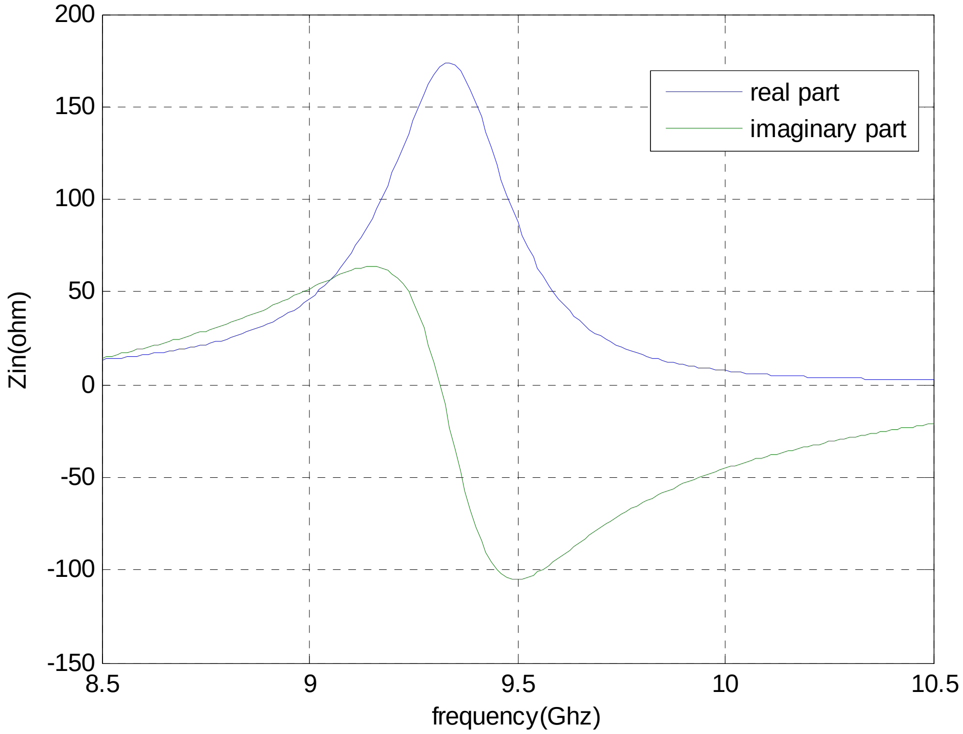

Fig.3.11 The input impedance of annular-ring patch antenna

3.3.2. The voltage wave standing ratio (VSWR)

The voltage standing wave ratios (VSWR) for annular-ring patch antenna using FDTD method is shown in figure 3.16. The bandwidth for which VSWR is less than 2 is over the frequency interval ranging from 8.90 GHz to 9.65GHz (i.e. 8.08%); a bandwidth which may be suitable for various applications.

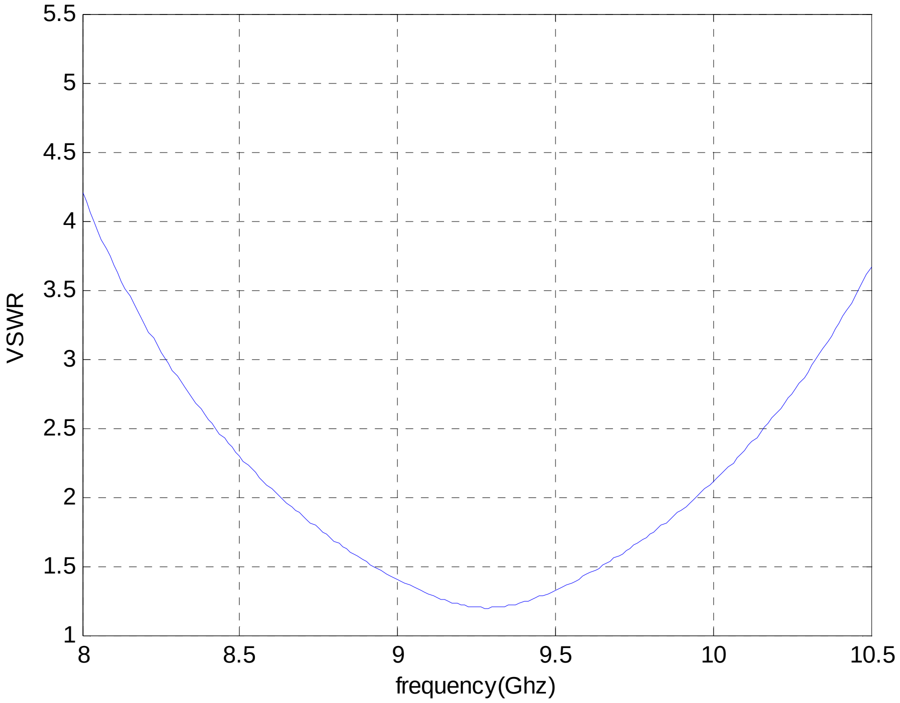

Fig.3.12 The voltage standing wave ratios of annular-ring with FDTD

3.3.3. Electric current distributed on the patch

To further understand the physical mechanism of the annular ring patch antenna, it would be much helpful if we could know the electric field and current distributions. To get the electric current distributions on the patch, a sinusoidal excitation at microstrip line feed is used, which is given by:

$$V(t) = \sin(2\pi f_0 t) \tag{3.3}$$

f_0 is the resonant frequency of interest;

The field distributions are recorded at one instant of time after the steady state has been reached. The electric current distributions J_x and J_y on the metals are obtained by the difference between the tangential magnetic fields above and below the metal interface [18], the electric current distributions on the patch are given by [18]:

$$J_x(i,j,k_s+2) = -[H_y(i,j,k_s+3) - H_y(i,j,k_s+2)] \tag{3.4a}$$

$$J_y(i,j,k_s+2) = -[H_x(i,j,k_s+3) - H_x(i,j,k_s+2)] \tag{3.4b}$$

i, j, k are integer number.

Figure 3.11 shows the current electric on the patch of annular-ring antenna at resonance frequency $f_r = 9.30GHz$ at 400 time step using FDTD method. These current distributions clearly show the resonant conditions at TM_{10} and TM_{01} modes respectively. The current J_y have the largest amplitude than current J_x on the patch. The figure shows clearly the variation of current electric (J_y and J_x) in annular patch shape.

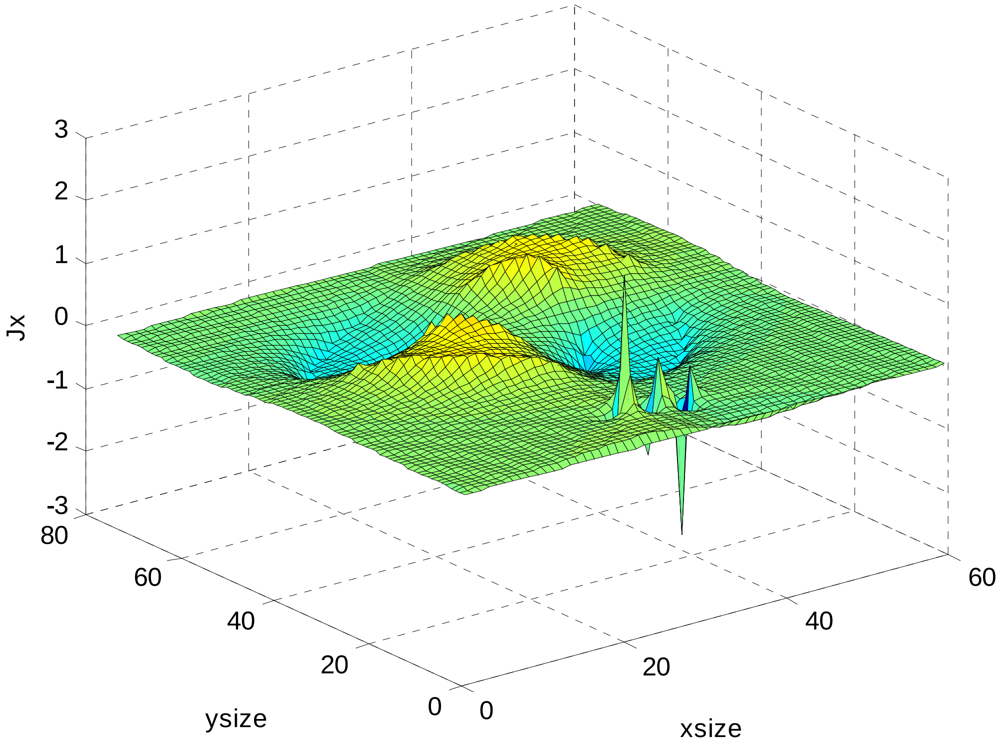

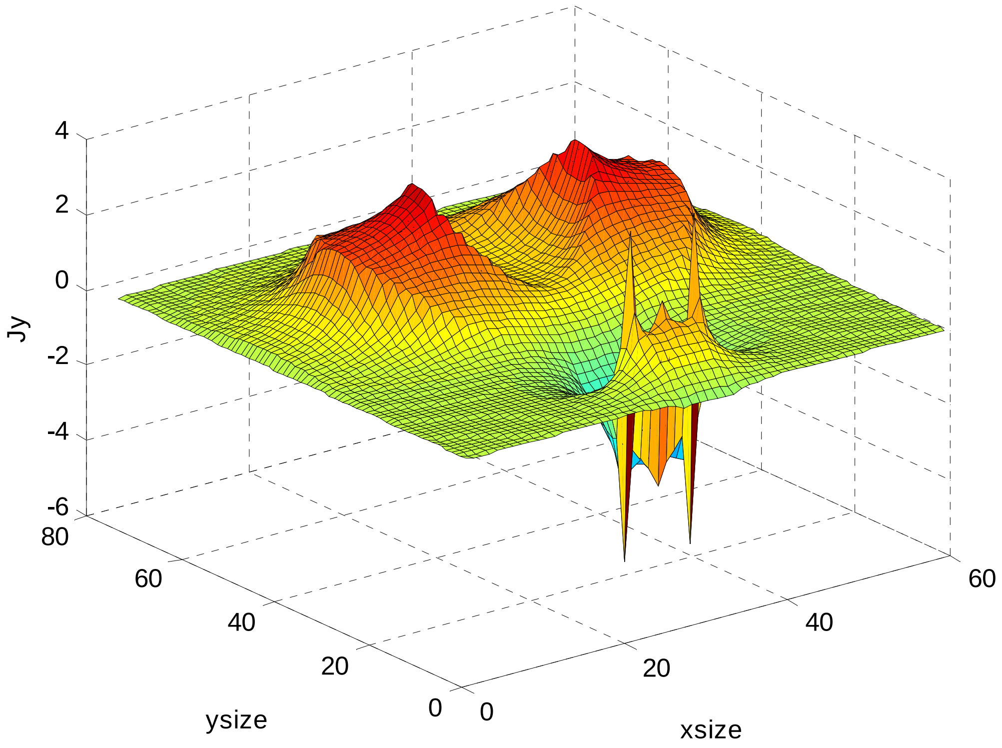

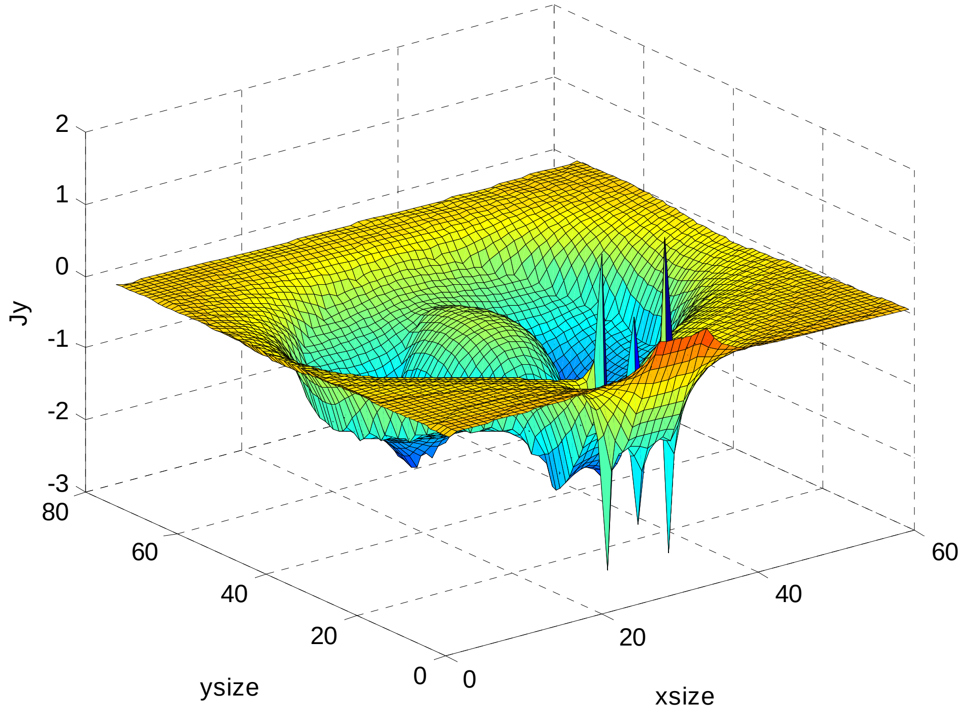

Fig.3.13 Electric current distributions on the annular ring patch antenna at $f_r = 9.30$ GHz

3.3.4. Far fields

Figures 3.14 and 3.15 show the simulated annular-ring radiation pattern that illustrate far field components (cross and co-polarizations) in E and H-planes using FDTD method and HFSS simulator at resonance frequency $f_r = 9.30$ GHz.

For the E-plane is shown in figure 3.14 (a) and (b), in the co-polarization component ,the graph of FDTD and HFSS are identical and symmetric, they have the peak of 0 dB at 0° and the min, FDTD has -5.70 dB whereas for HFSS has -5.75 at 90°. The cross-polarization component has a level of -29.06 dB at 0° below the copolar field for HFSS and for FDTD has -28 dB at 0°.

The H-plane i shown in figure 3.15 (a) and (b), in co-polar which are the same for HFSS simulator and FDTD method (have a peak of 0 dB at 0°), for H-plane cross-polarization has a peak of -6.10 dB at 90° for HFSS simulator, whereas for FDTD method is -5 dB at 90°, and the min FDTD has -28 dB at 0° where for HFSS has -69 dB. For all the results ,it shows a good agreement.

Figure 3.16 shows the total gain of annular-ring patch antenna using HFSS simulator at resonance frequency $f_r = 9.30GHz$ with finite ground plane, at $\emptyset = 0°$ and $\emptyset = 90°$. The total gain is maximum in the $\theta = 0°$ direction and the HFSS shows also the back radiation which is due to imperfections which are not specified to the simulator.

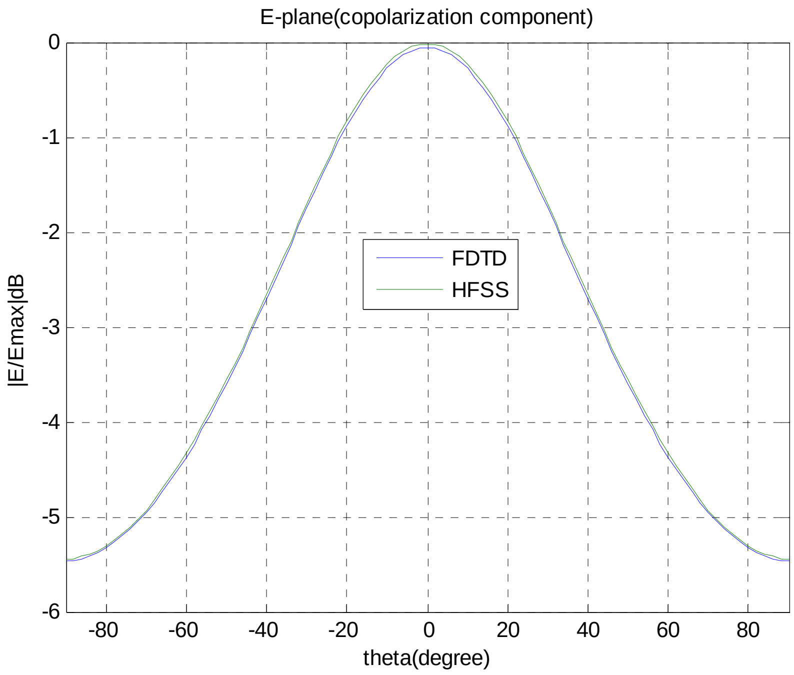

(a)

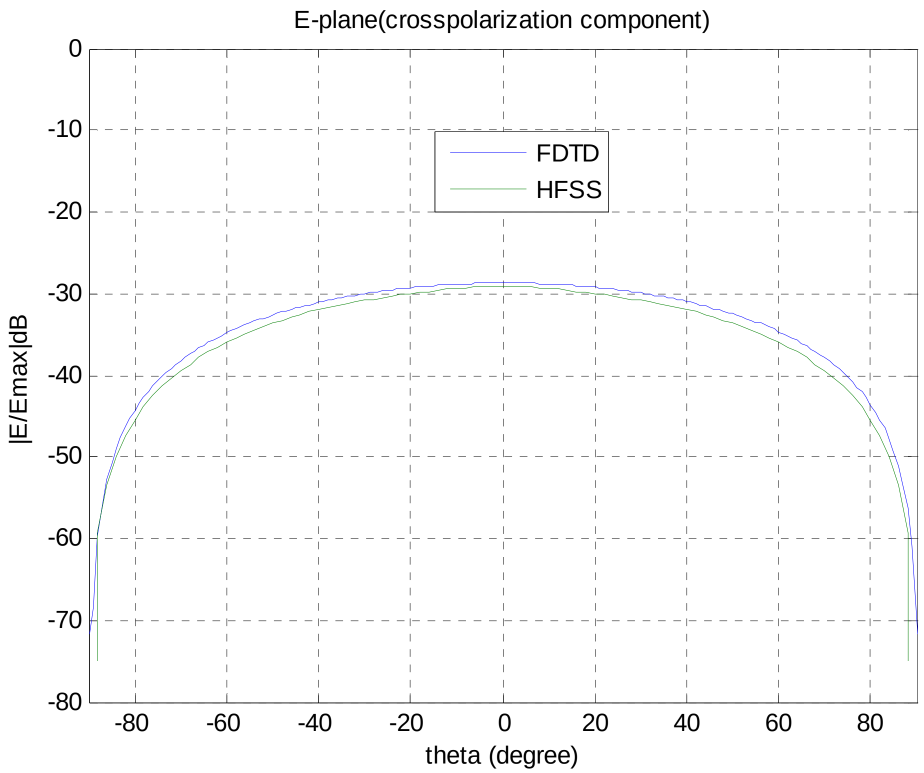

(b)

Fig.3.14 E-plane radiation pattern of annular-ring patch antenna at $f_r = 9.30GHz$

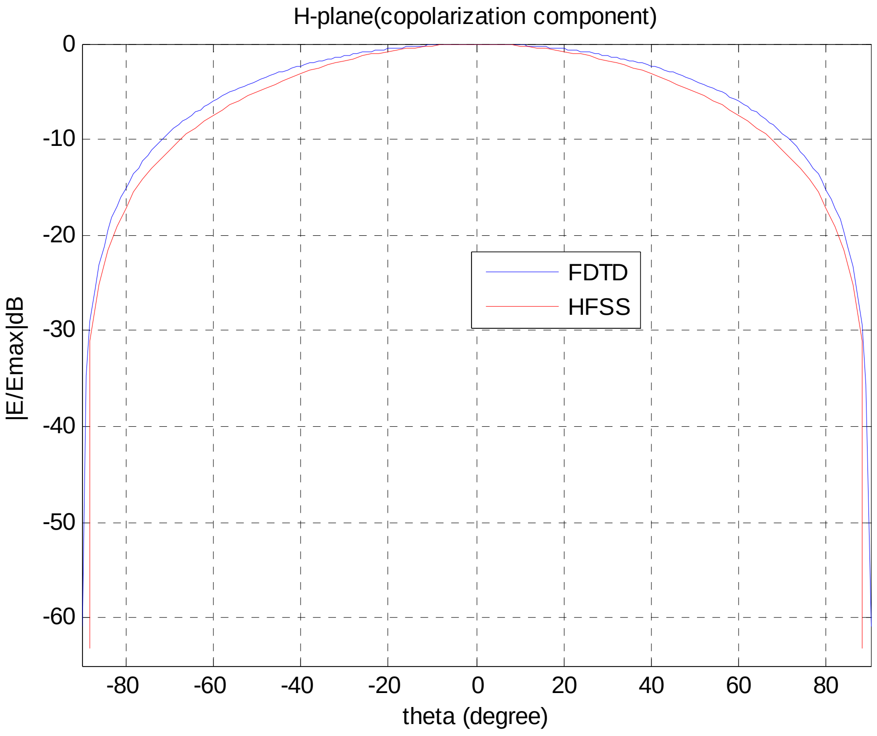

(a)

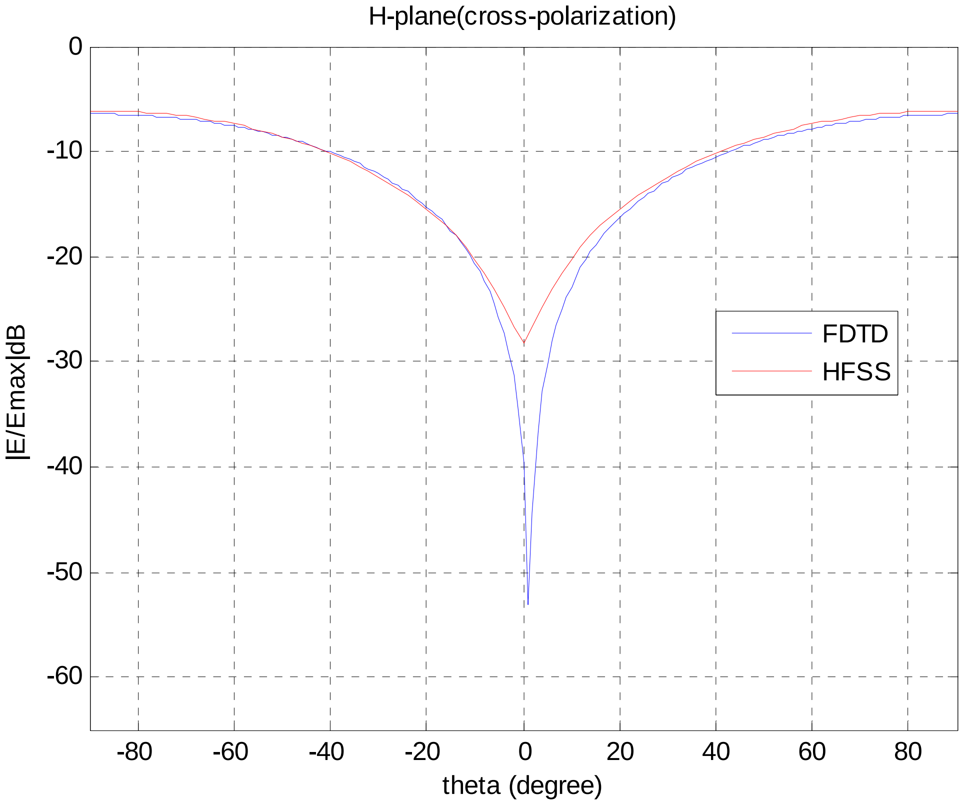

(b)

Fig.3.15 H plane radiation pattern of annular-ring patch antenna at $f_r = 9.30 GHz$

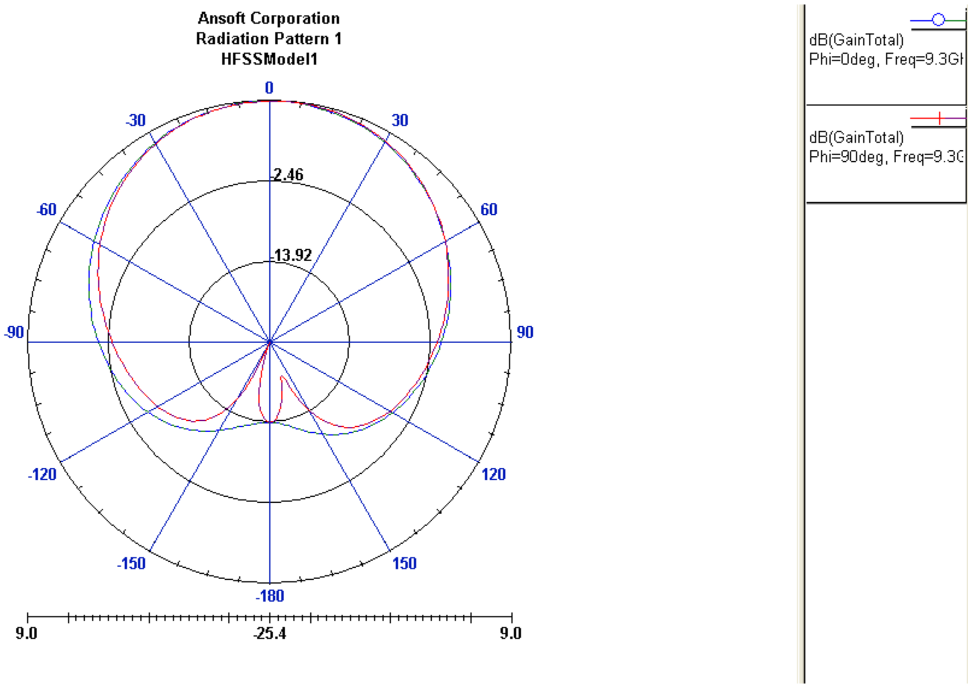

Fig.3.16 Total directivity of annular-ring patch antenna at $f_r = 9.30 GHz$

3. 4.Semi-ring patch antenna

In this section, the analysis of a probe fed semi-ring microstrip patch antenna using FDTD method is discussed. A probe-fed microstrip antenna is very useful because it is easily fabricated, and the location of the probe feeding point can be adjusted to match the impedance of the coaxial line. The specific antenna under consideration is shown in figure 3.17. This antenna is of the dimension of inner diameter a = 3.5 mm and outer diameter b = 7 mm, on the substrate of thickness h =1.59 mm and relative permittivity $\varepsilon_r = 2.2$. The probe is of the diameter 1.27 mm

The FDTD analysis of this antenna used a computational domain of $60\Delta x \times 40\ \Delta y \times 20\ \Delta z$ unit cells in the $x, y, and\ z$ directions, respectively. In the region around the antenna, the grid spacing used are $\Delta x = \Delta y = 0.35\,mm$ and $\Delta z = 0.53\,mm$ .with this grid spacing, the antenna has a diameter $40\Delta x$ on a substrate of total thickness $3\Delta z$. The time step is determined from the smallest grid spacing and must satisfy the stability criterion. For this antenna $\Delta t = 0.74800\,psec$ the probe feed is excited by a Gaussian pulse with $T = 60\ p\sec$ and $t_0 = 180\,p\sec$. The simulation was run for 3000 time-steps,

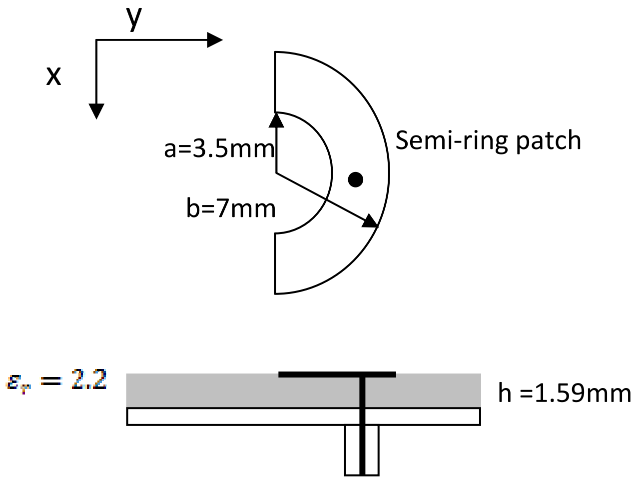

Fig.3.17 Probe-fed **se**mi-ring patch

In this section, the gap feed model is used, which is proposed in chapter II (section 2.5). The feed model is shown in Figure 3.18. In this case the substrate height is equal to 3Δz and the series resistor Rs *is* assumed to be 50Ω. By applying Ampere's circuital law, the current on the feed probe is obtained by taking the line integral of magnetic field around the electric field source location, which is given as [18]:

$$I^{n-\frac{1}{2}} = \left[H_x^{n-\frac{1}{2}}(i_s, j_{s-1}, k_{s+1}) - H_x^{n-\frac{1}{2}}(i_s, j_s, k_{s+1})\right]\Delta x + \left[H_y^{n-\frac{1}{2}}(i_s, j_s, k_{s+1}) -\right.$$

(3.5)

By applying Ohm’s law to the circuit of Figure 3 (a), the electric source field is obtained as

$$E^n(i_s, j_s, k_z) = \frac{V(n\Delta t) + I^{n-\frac{1}{2}} R_s}{3\Delta z} \tag{3.6}$$

Where$k_z = K_s, K_{s+1}, K_{s+2}$ finally, the current and voltage are transformed to the Fourier domain. The input impedance of the antenna is obtained from:

$$Z_{in} = \frac{V(f)}{I(f)} - R_s \tag{3.7}$$

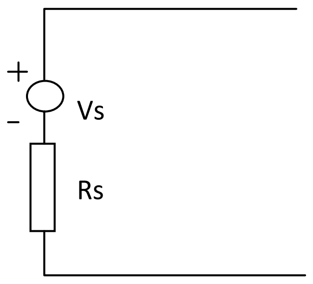

(a)

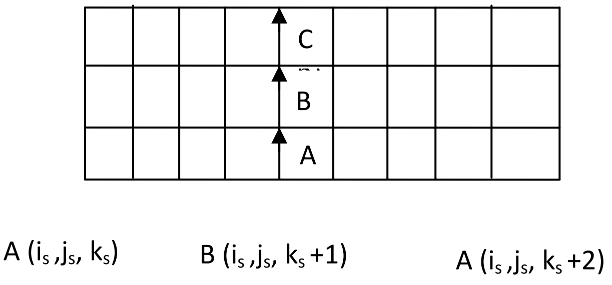

Fig.3.18 The probe feed model.

The absorbing boundary condition for antenna structure and feed is the same as annular-ring patch antenna (The Mur second order absorbing boundary condition was used in the 3D simulation space (boundary of the structure) and the Mur first order in the 1D (feed part).

3.4.1. Reflection coefficient and input impedance

Figure 3.19 shows the S_{11} of semi-ring patch antenna using both FDTD and HFSS simulator,

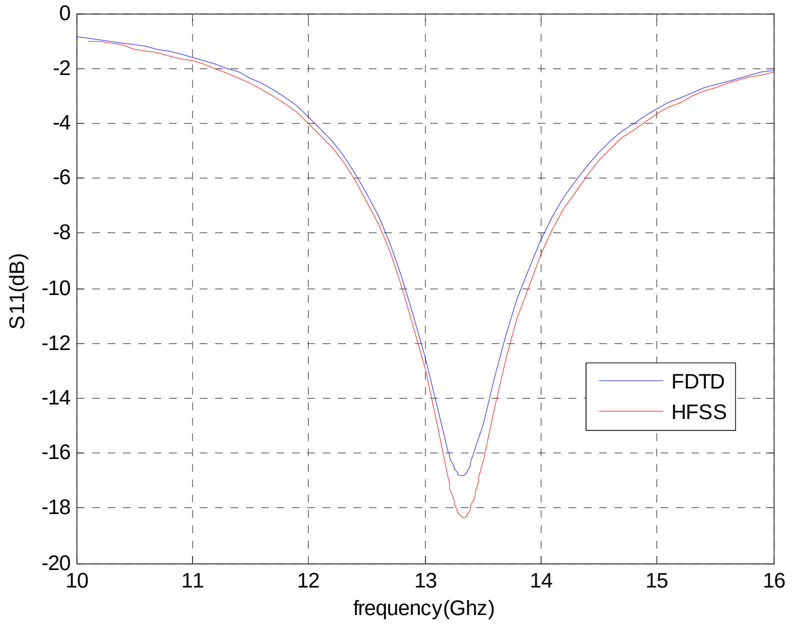

Fig.3.19 The $S_{11}$of semi-ring patch antenna

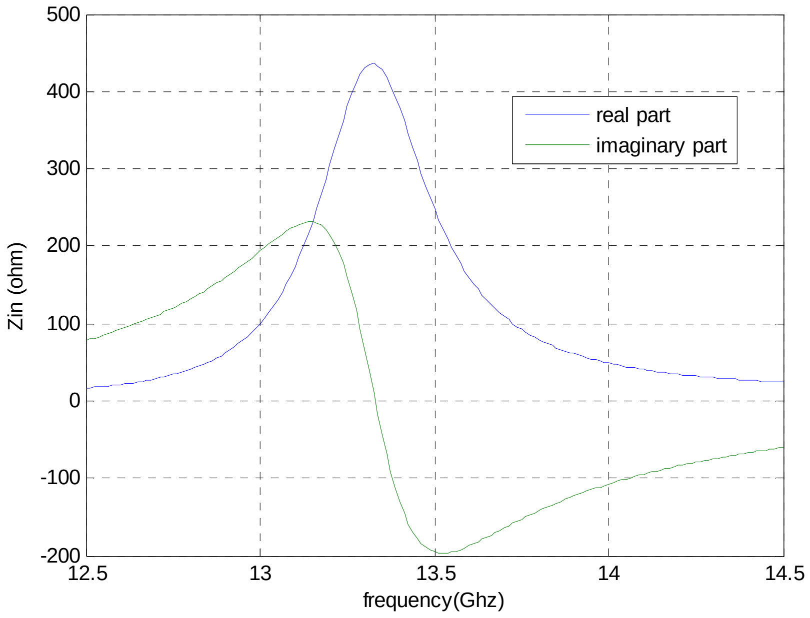

Fig.3.20 Input impedance of semi-ring patch antenna using FDTD method

It is seen from the figure 3.19, that the resonance frequency is 13.30 GHz for FDTD where for HFSS is 13.35GHz, The differences between simulated and FDTD method results are probably related with the less accurate modeling of the semi-ring patch shape. But we can say a good result.

Figure 3.20 shows the real and the imaginary parts of semi-ring patch antenna at resonance frequency $f_r = 13.30GHz$ using FDTD method, in this frequency while the real part is maximum, the imaginary part is zero ,this define the bandwidth for VSWR<2, the maximum of real part is $maxR_{in} = 440\ \Omega$.

3.4.2. The far fields

Figures 3.21 and 3.22 show the simulated semi-ring radiation pattern that show the far field components (cross and co-polarizations) in E and H-planes using FDTD method and compare the result with HFSS simulator at resonance frequency $f_r = 13.30GHz$.

For the E-plane co-polarization, in figure 3.21 (a) the graph of FDTD and HFSS are identical and symmetric. And properly the peak of FDTD is 0.01dB at 0° and 0 dB at 0° for HFSS, the min -5.25 dB for FDTD and -4.92 dB for HFSS at 90°.

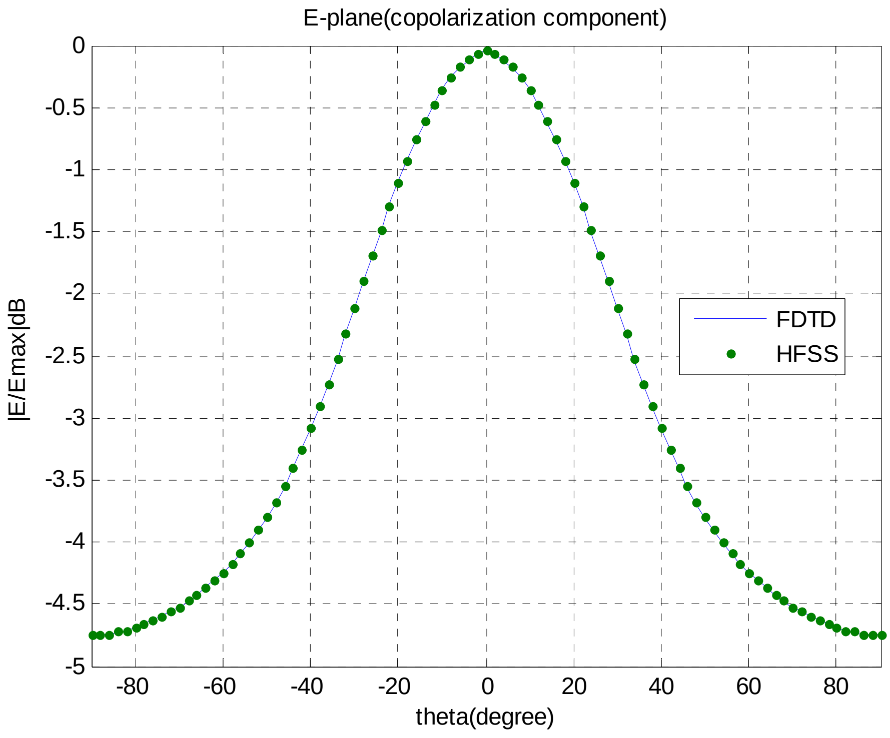

(a)

The E-plane cross-polarization is shown in figure 3.21(b),it has a peak of -29 dB at 0° below the co-polar for FDTD and for HFSS simulator has -29.10dB,the shape are similar and symmetrical.

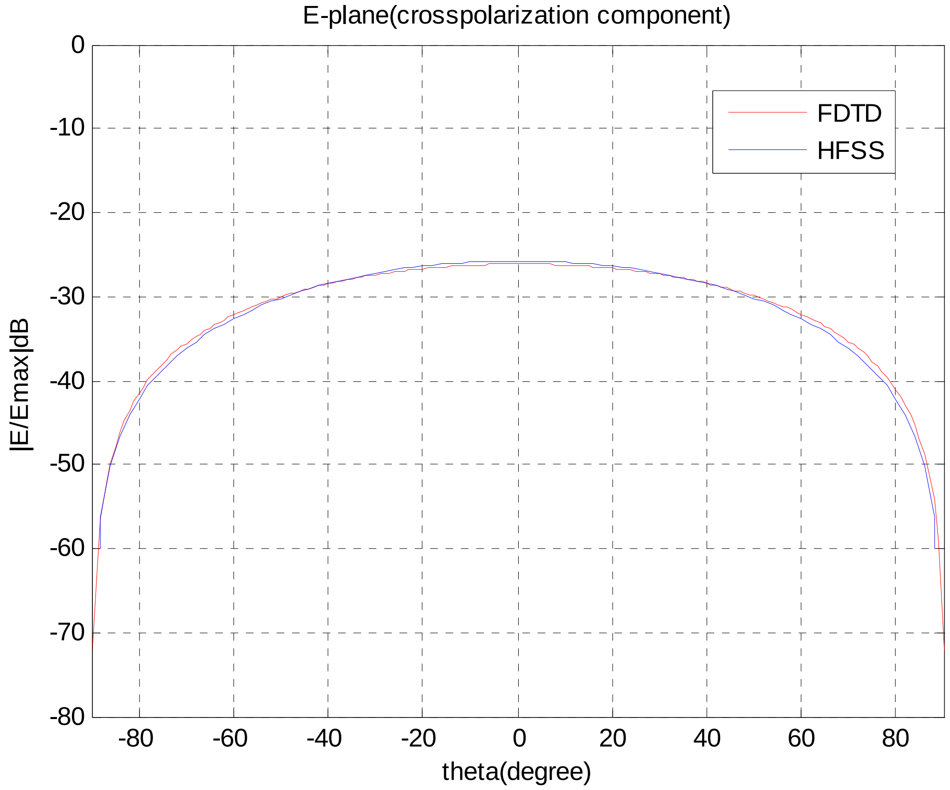

(b)

Fig.3.21 E-plane radiation pattern of semi-ring

The H-plane co-polar is shown in figure.3.22 (a), for FDTD method has a peak value of 0 dB at 0° and also HFSS simulator has a peak of 0 dB at 0°, they are approximately the same, for H-plane cross - polarization illustrated in figure 3.23 (b) has a peak of -5.01 dB at 90° for HFSS simulator, whereas for FDTD method is -5 dB at 90°, which show a good results.

Figure 3.23 shows the total gain of semi-ring patch antenna for $\emptyset = 0°$ and $\emptyset$ = 90° at $f_r = 13.3.0GHz$ using HFSS simulator using finite ground plane. In the upper plane the shape is simmilar for $\emptyset$=0° and $\emptyset$=90°, but in the back plane there is a little difference.

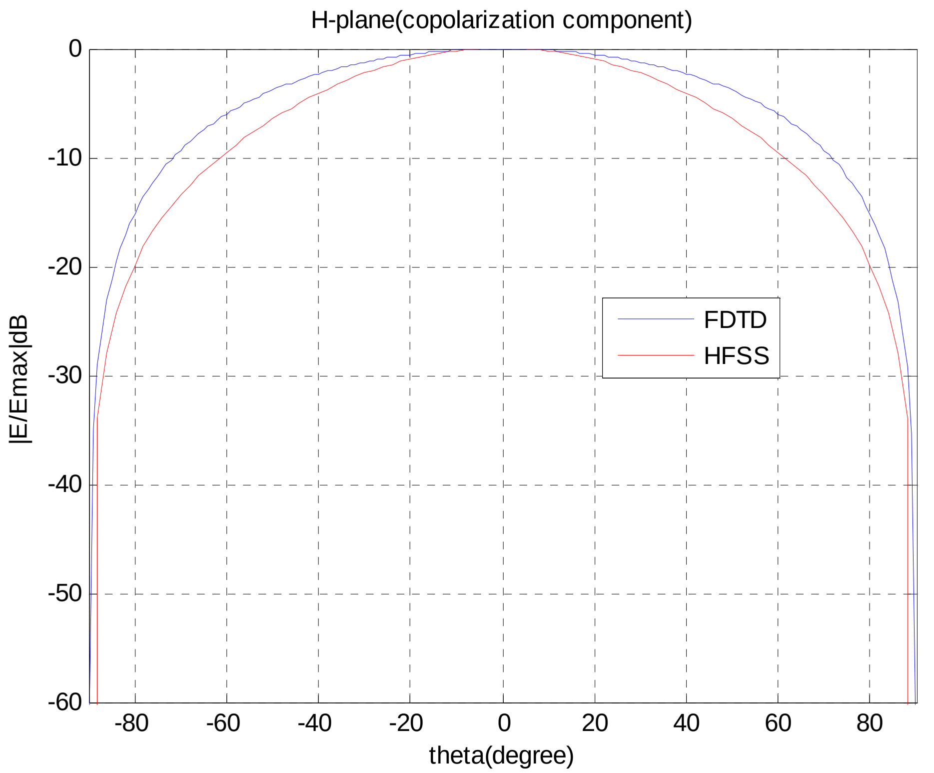

(a)

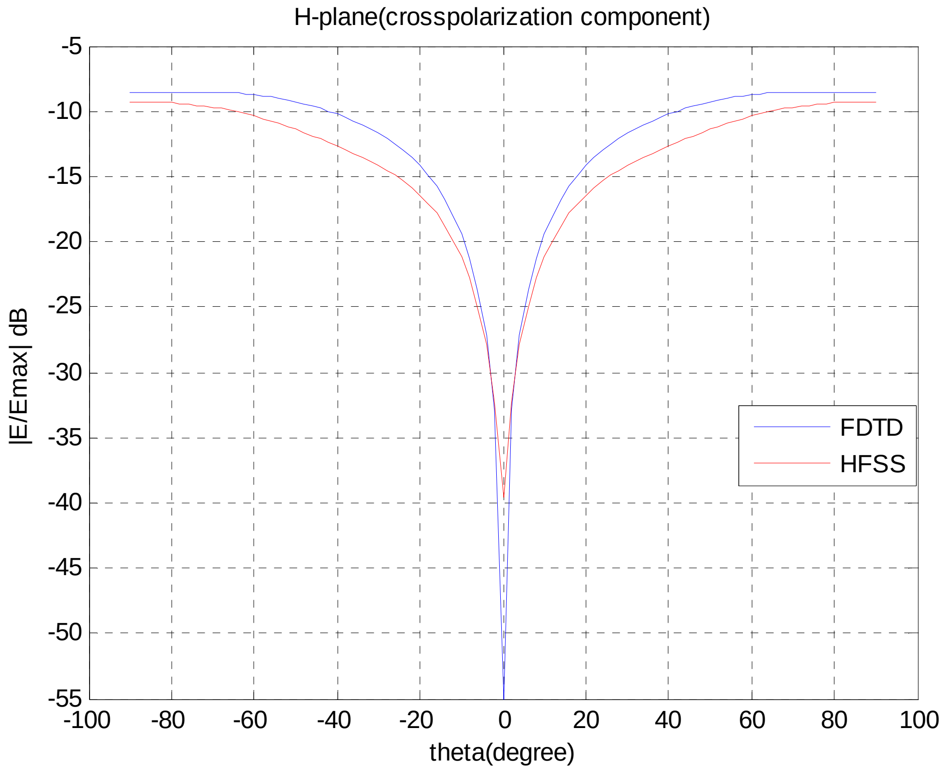

(b)

Fig.3.22 H-plane of semi-ring patch antenna at $f_r = 13.30GHz$

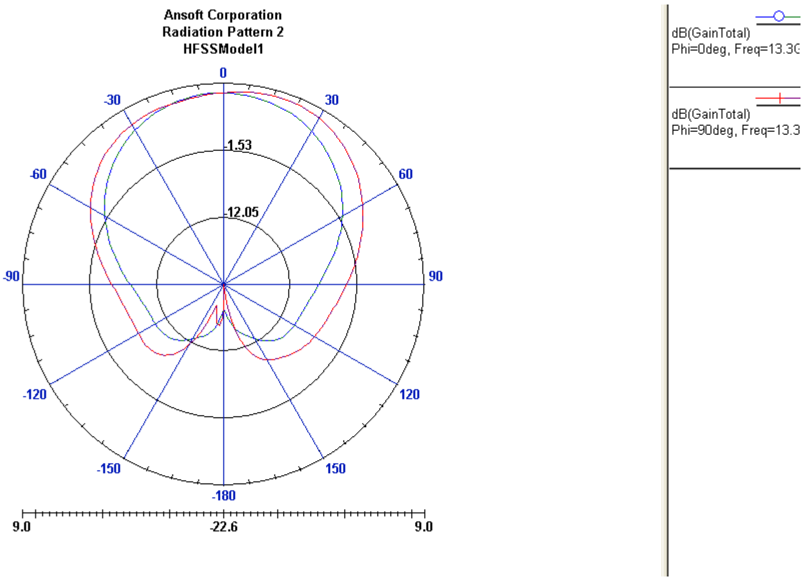

Fig.3.23 Total gain of semi-ring patch antenna at $f_r = 13.3GHz$

3.4.3. Voltage standing wave ratios (VSWR):

The voltage standing wave ratios (VSWR) for semi-ring patch antenna for FDTD method is depicted in figure 3.24. The band of frequencies over which the input voltage standing wave ratio less than 2 is from 12.80 GHz to 13.90 GHz, or 8.24 % which is considerably important.

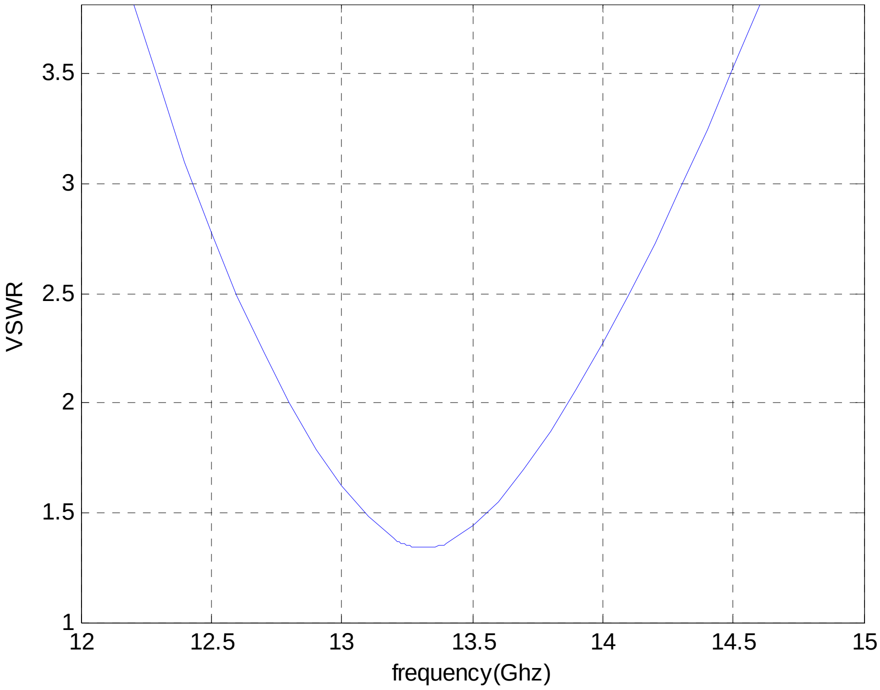

Fig.3.24 The voltage standing wave ratios of semi-ring patch antenna using FDTD method

3.5." Berber-Z" microstrip antenna:

This section describes the analysis of a new shape of patch antenna which is Berber-Z. We want to analyse and see the characteristic of new design. This is achieved by using FDTD method and compares the results with HFSS simulator;

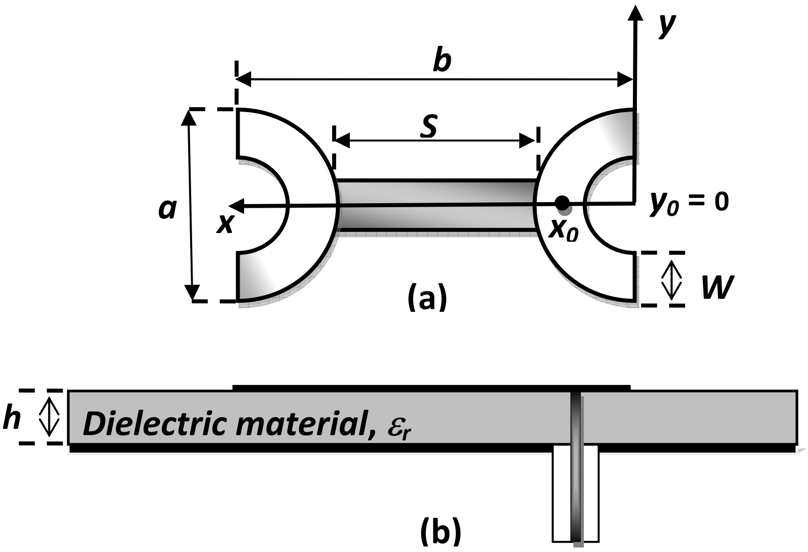

Figure 3.25: *Berber-Z* microstrip patch antenna configuration.

a =14 mm, b=21 mm, S=7mm, w =3.5 mm, h =1.59 mm

(a) Top view, **(b)** Side view

In this section, the analysis of a probe fed Berber -Z microstrip antenna using FDTD method is discussed. Actually, this shape is obtained by combining in cascade two semi-rings at the 2-extrimities and a rectangular like dipole in the middle as shown in figure.3.25. The specific antenna under consideration is shown in figure 3.25. This antenna is of the dimension a = 14 mm and b = 21mm, on the substrate of thickness h = 1.59 mm and relative permittivity $\varepsilon_r = 2.2$. The probe is of the diameter 0.32 mm.

The FDTD analysis of this antenna used a computational domain of $60\Delta x \times 90\Delta y \times 30\Delta z$ unit cells in the $x, y, and\ z$ directions, respectively. In the region around the antenna, the grids spacing used are $\Delta x = \Delta y = 0.35\,mm$ and $\Delta z = 0.53\,mm$. With these grids spacing, the antenna has a dimension of $40\Delta x \times 60\Delta y$ on a substrate of total thickness $3\Delta z$. The time step is determined from the smallest grid spacing and must satisfy the stability criterion. For this antenna $\Delta t = 0.74800psec$. The probe feed is excited by a Gaussian pulse with $T = 60\ psec$ and $t_0 = 180\ psec$. The boundary condition is the same those applied in semi-ring patch antenna (in section 3.5).The simulation time step of Berber- Z patch antenna is 4500 time step.

3.5.1. Reflection coefficient

The input return loss of the *Berber -Z* patch antenna obtained using FDTD method and HFSS is shown in figure 3.26. The figure shows that the structure can be regarded as a tri-frequency band antenna. The three antenna resonant frequencies based on FDTD method are respectively 9.34 GHz, 13.44 GHz and 16.25 GHz. However, the resonant frequencies using HFSS are 9.35 GHz, 13.50 GHz and 16.30 GHz respectively. These results show good agreement and the small differences are due to the discretization, stair-casing used in semi-rings of *Berber-Z* in the FDTD simulation as well as the approximations assumed in the HFSS. Further, it can be observed that a parametric study will certainly increase the radiation efficiency of the lower and the outer resonant frequencies of the tri frequency band structure.

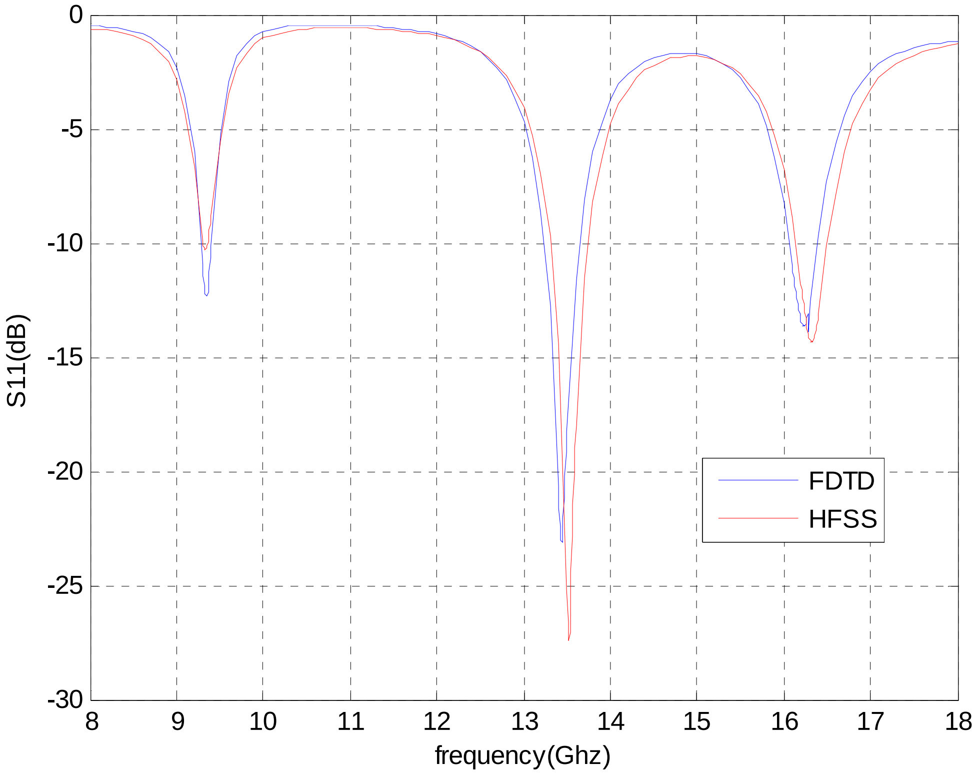

Fig.3.26 The return loss of Berber-Z patch antenna.

a = 14 mm, b = 21mm, h = 1.59 mm, $\varepsilon_r = 2.2$,the loss tangent $tg(\delta) = 0.0009$.

3.5.2. Voltage standing wave ratios (VSWR)

The *Berber-Z* patch antenna voltage standing wave ratios obtained using FDTD method is shown in figure 3. The three resonant frequencies are clearly apparent in this figure.

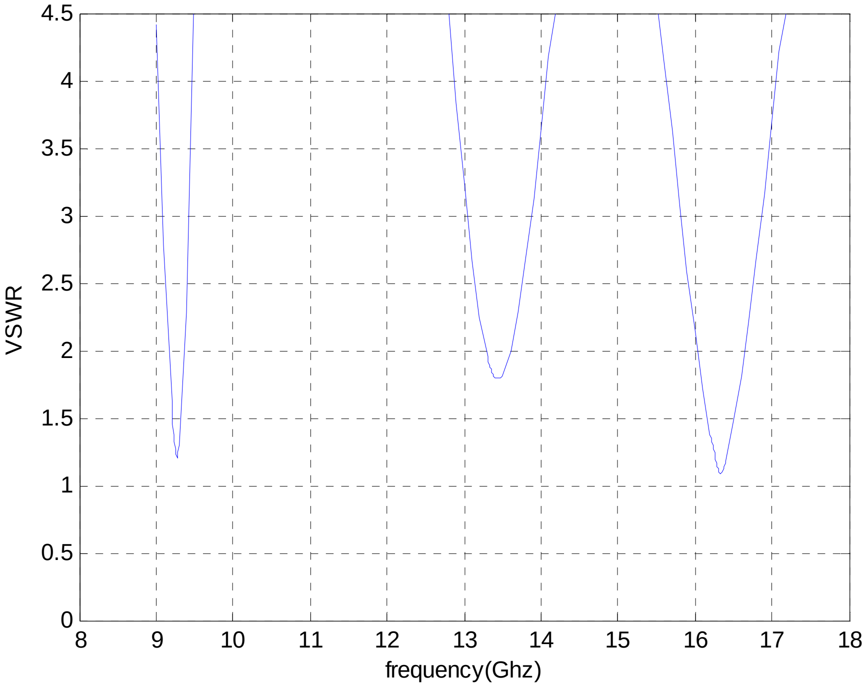

Fig.3.27 The voltage standing wave ratios of semi-ring with FDTD

The frequency band for which the VSWR is less than 2 with respect to the first resonant frequency $\left(f_r = 9.34\,\text{GHZ}\right)$ ranges from 9.19 GHz to 9.40 GHz (i.e. 2.23 %) and, for the second resonant frequency $\left(f_r = 13.44\,\text{GHZ}\right)$ the range is from 13.25 GHz to 13.64 GHz (i.e. 2.9 %). Whereas, for the last resonant frequency $\left(f_r = 16.25\,\text{GHZ}\right)$, the range extends from 16.04 GHz to 16.55GHz (i.e. 3.13 %). Furthermore, it can be observed that the three bands are comparable.

3.5.3. Far fields

Figures 3.28 , 3.29 and 3.30 show far field components (cross and co-polarizations) of the 'Berber-Z' patch antenna radiation pattern in E and H-planes obtained using FDTD method and compare them with those obtained using HFSS simulator at the three resonant frequencies which are;

$f_r = 9.34GHz$, $f_r = 13.44GHz$ and $f_r = 16.25GHz$.

The E-plane co-polarization patterns (figures 3.28(a), 3.29(a) and 3.30(a)) present at the three resonant frequencies main and secondary lobes. The FDTD radiation pattern results agree with those obtained using HFSS. As expected, it is observed that the main lobes broadening decreases from first resonance frequency to the third frequency. Also, the secondary lobes levels increase as the resonant frequency increases for both FDTD method and HFSS.

The E-plane cross polarizations patterns (figures 328(b),3.29(b) and 3.30(b)) present similar shapes at the three frequencies with slight difference in levels. For the first frequency $(f_r = 9.34\,\text{GHZ})$ the field level is at 26 dB below the main lobe of the co-polar field; for the two other frequencies ($f_r = 13.44\,\text{GHZ}$ and $f_r = 16.25\,\text{GHZ}$), the levels are respectively at 29 dB and 23 dB under the main lobes of the copular components. These levels are highly satisfactory for practical requirements. Again, the patterns are similar to those obtained using HFSS.

The H-plane co-polarization fields are shown in figures 3.28(c), 3.29(c) and 3.30(c) for the three resonant frequencies respectively. The shape of the pattern obtained using FDTD and HFSS simulator at $f_r = 9.34\,\text{GHZ}$ and $f_r = 13.44\,\text{GHZ}$ are similar. However, the pattern obtained at $f_r = 16.25\,\text{GHZ}$ has a main lobe and lateral lobes which are 33dB below the main lobe maximum.

The H-plane cross polarization field patterns are shown in figures 3.28(d), 3.29(d) and 3.30(d). As expected, the patterns at the three frequencies are similar in shape. And it can be seen that the FDTD predicts better the radiation in the main radiation direction. However, the patterns based on HFSS show good results for the main radiation direction with relatively higher power level. But, this does not present any limitation for its practical use. Once getting away from mail direction, the patterns get relatively high (-20 dB).

To compare the power levels of the radiated fields at the three resonant frequencies, the co-polarization E-plane patterns are illustrated in figure 7. These patterns are normalized with respect to the maximum field which is found to occur at the resonant frequency $f_r = 13.44\,\text{GHZ}$. The superposition of the three patterns shown in figure 7 indicates clearly that the levels of the three patterns in the maximum radiation direction are very close to each other. Numerically, field levels at frequencies $f_r = 9.34\,\text{GHZ}$ and $f_r = 16.25\,\text{GHZ}$ are not lower than -1.14 dB with respect to the maximum level.

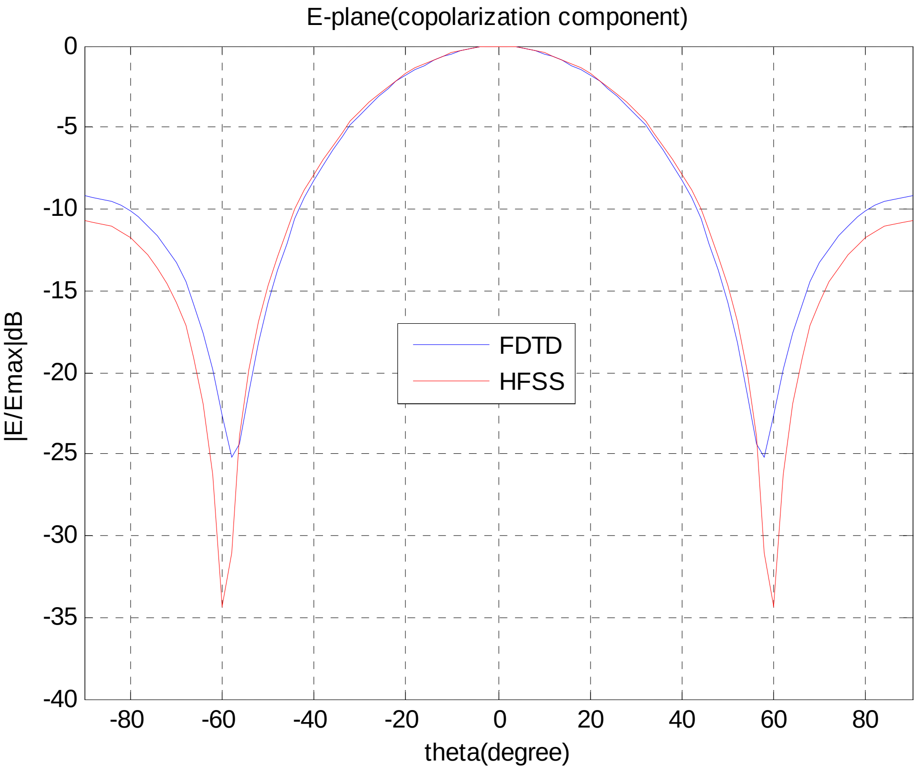
E-plane(copolarization component)
|E/Emax|dB
0
-5
-10
-15
-20
-25
-30
-35
-40
-80
-60
-40
-20
0
20
40
60
80
theta(degree)
FDTD
HFSS

(a)

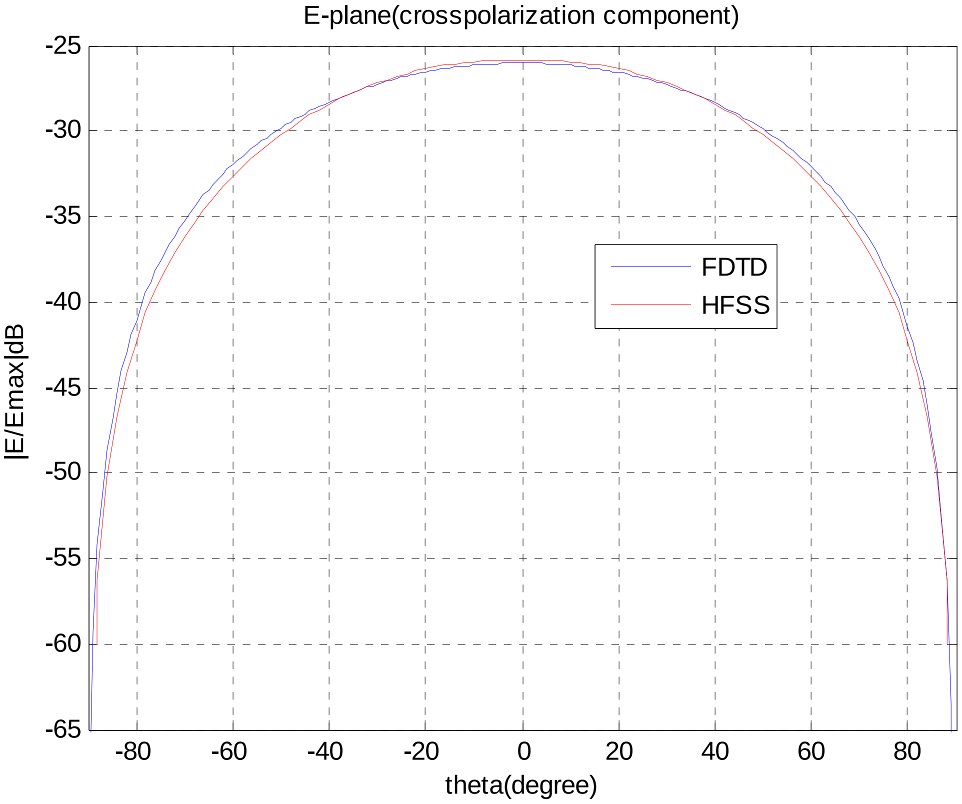
E-plane(crosspolarization component)
|E/Emax|dB
-25
-30
-35
-40
-45
-50
-55
-60
-65
-80
-60
-40
-20
0
20
40
60
80
theta(degree)
FDTD
HFSS

(b)

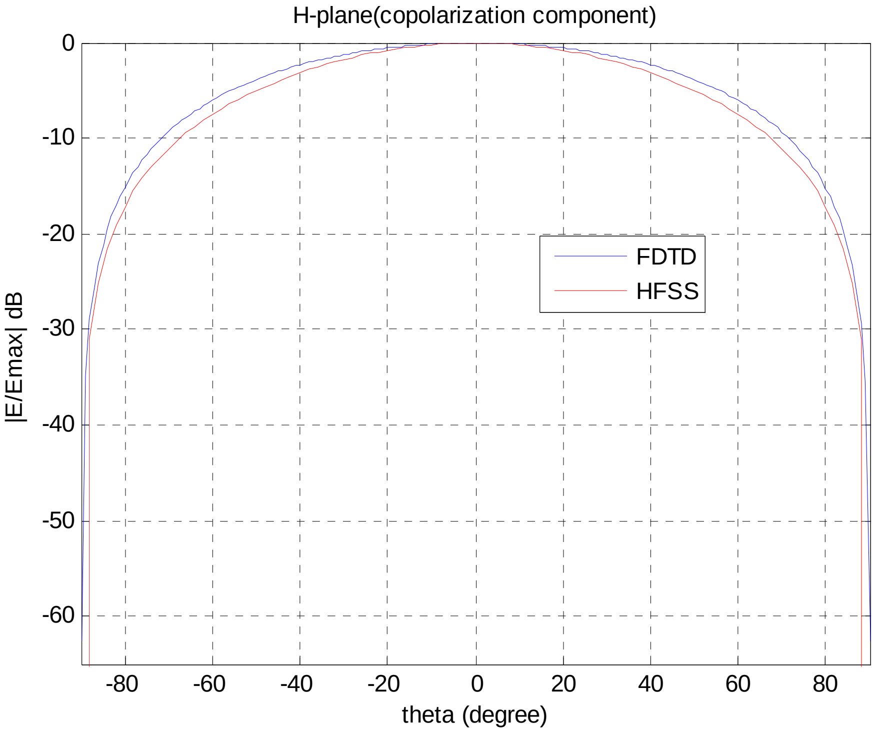

(c)

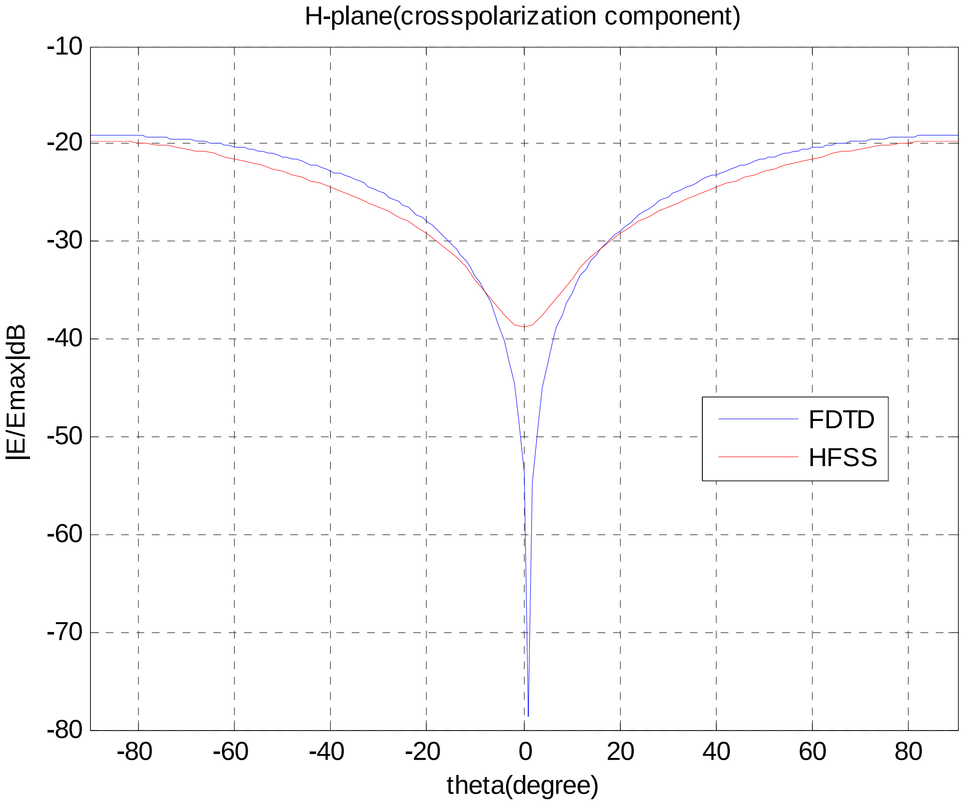

(d)

Fig.3.28 E-plane and H-plane of Berber-Z patch antenna at $f_r = 9.34GHz$

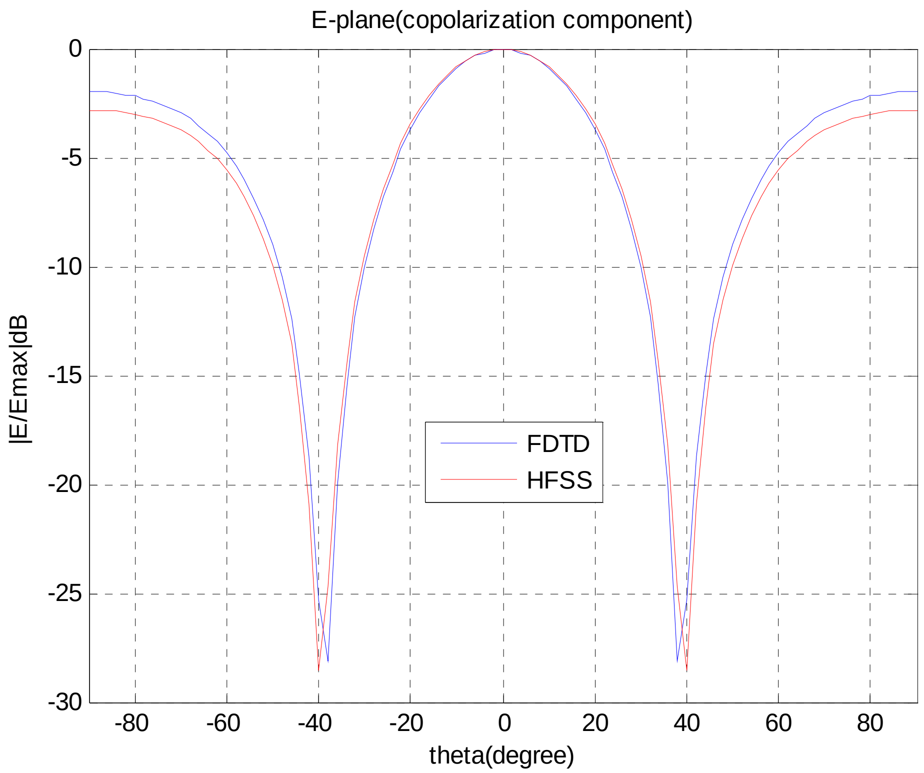
E-plane(copolarization component)
0
-5
-10
-15
-20
-25
-30
|E/Emax|dB
-80
-60
-40
-20
0
20
40
60
80
theta(degree)
FDTD
HFSS

(a)

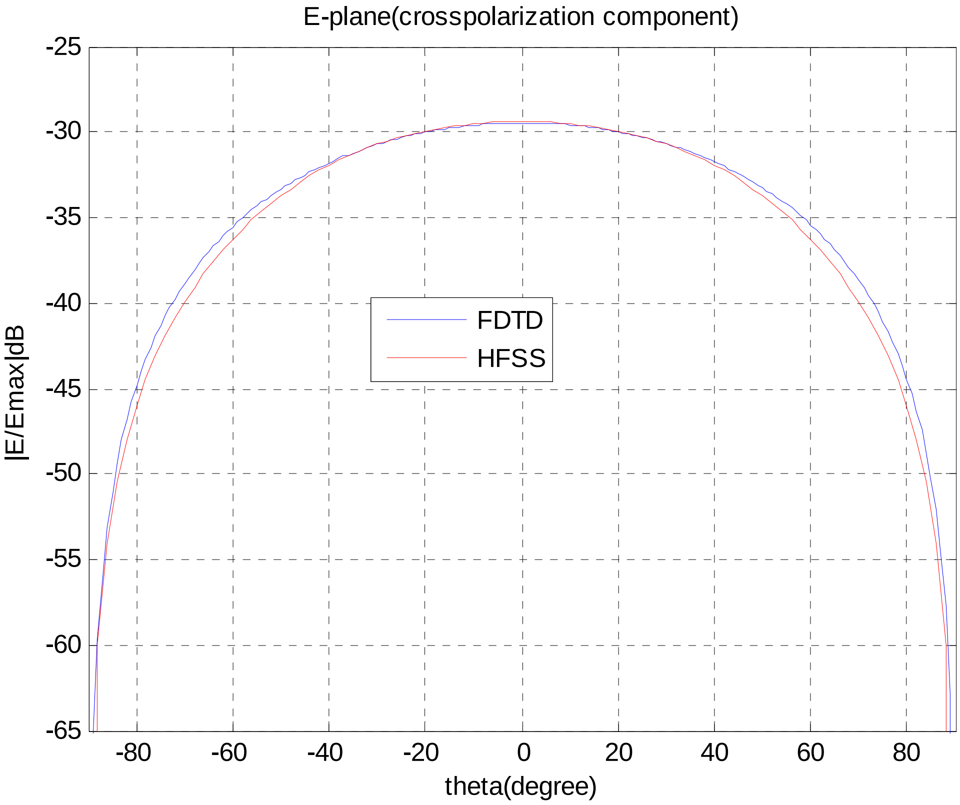
E-plane(crosspolarization component)
-25
-30
-35
-40
-45
-50
-55
-60
-65
|E/Emax|dB
-80
-60
-40
-20
0
20
40
60
80
theta(degree)
FDTD
HFSS

(b)

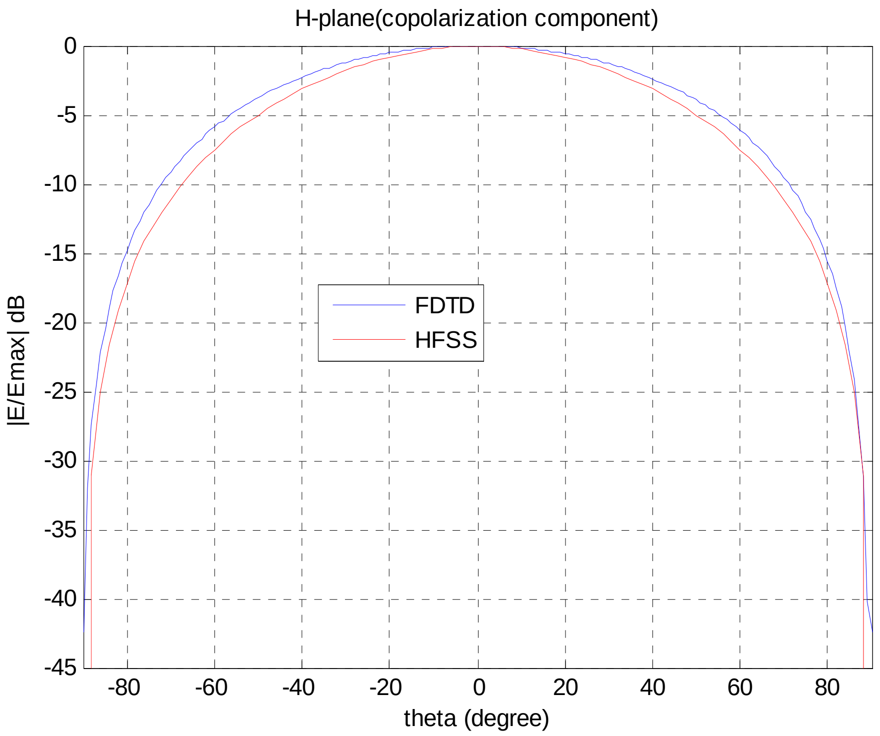

(c)

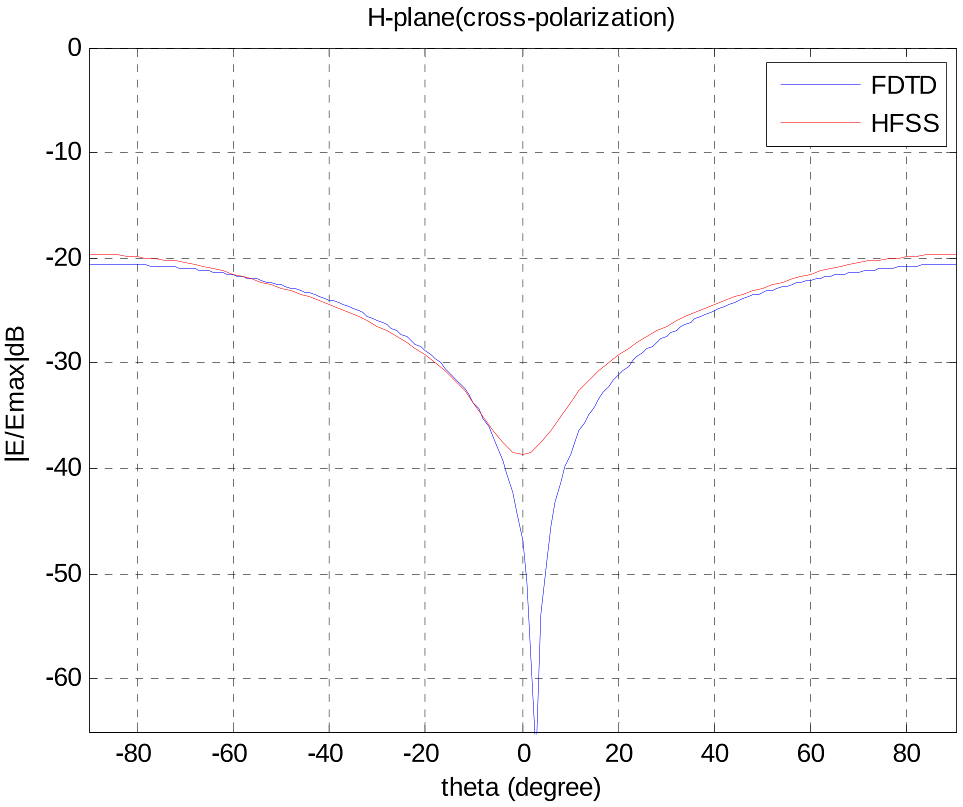

(d)

Fig.3.29 E-plane and H-plane of Berber-Z patch antenna at $f_r = 13.44GHz$

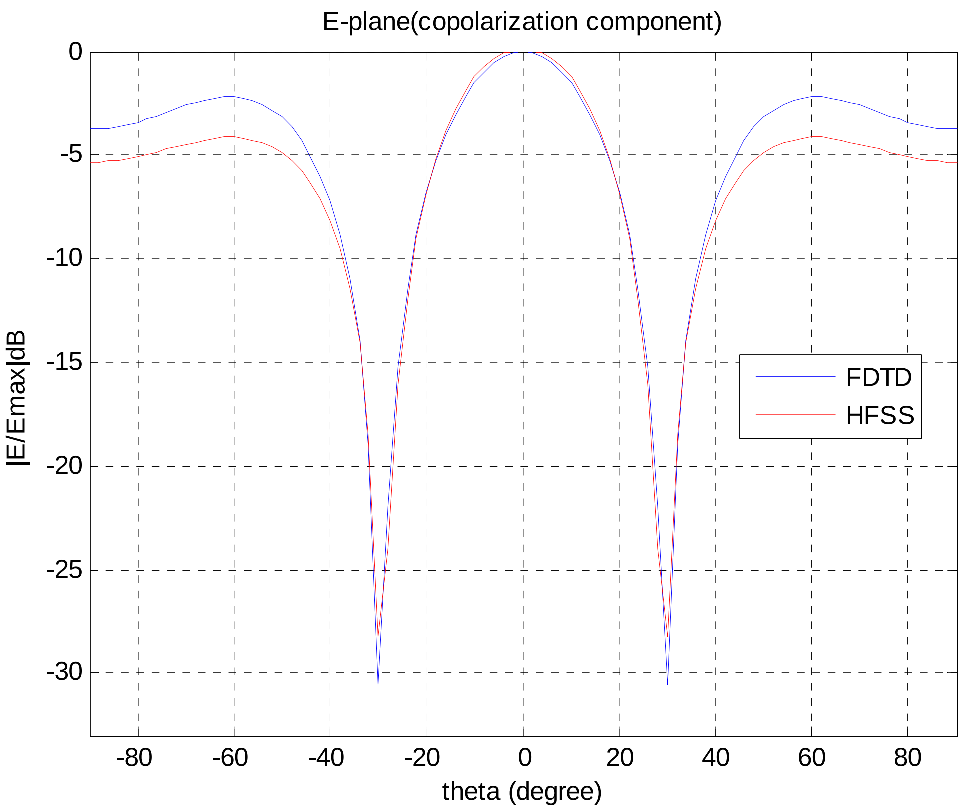
E-plane(copolarization component)
0
-5
-10
-15
-20
-25
-30
|E/Emax|dB
-80
-60
-40
-20
0
20
40
60
80
theta (degree)
FDTD
HFSS

(a)

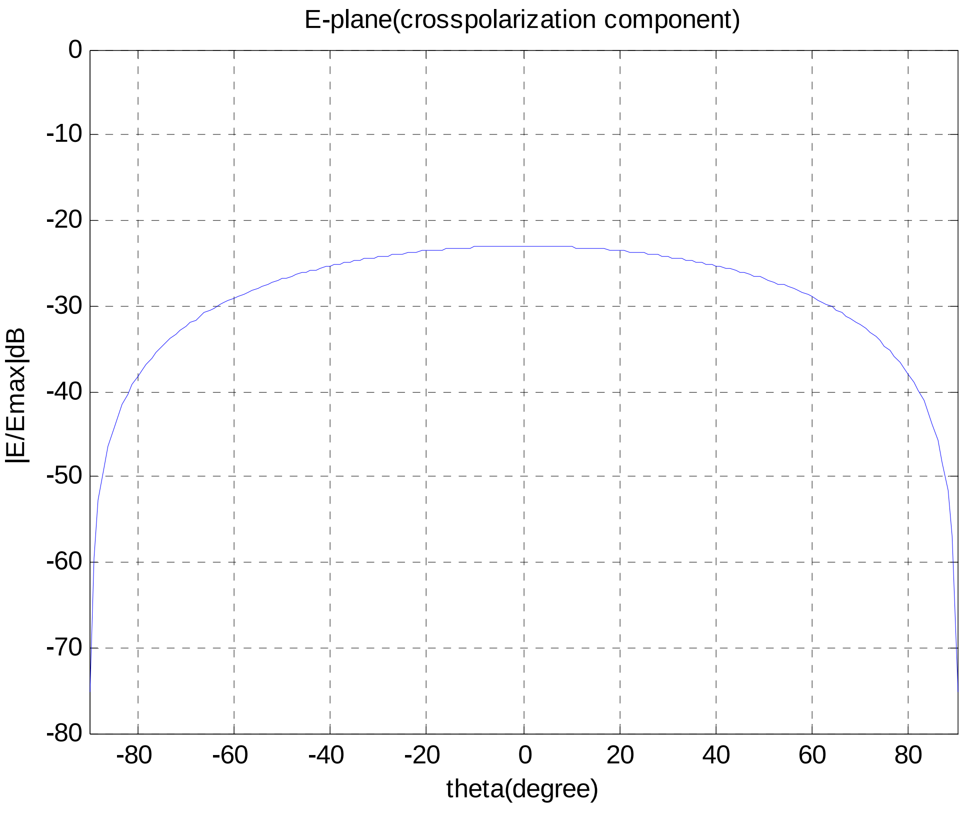
E-plane(crosspolarization component)
0
-10
-20
-30
-40
-50
-60
-70
-80
|E/Emax|dB
-80
-60
-40
-20
0
20
40
60
80
theta(degree)

(b)

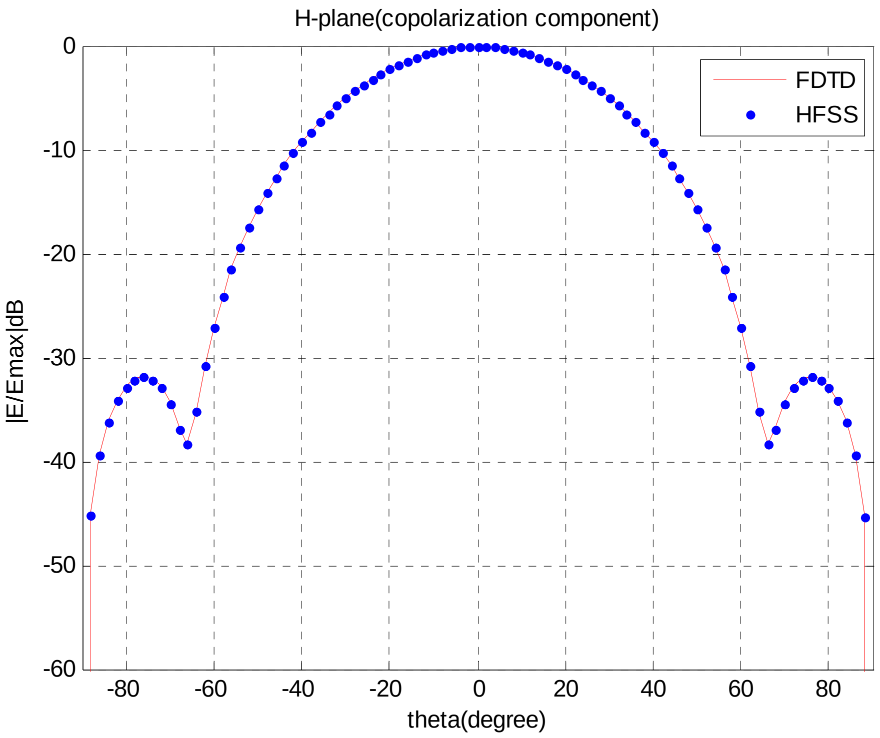

(c)

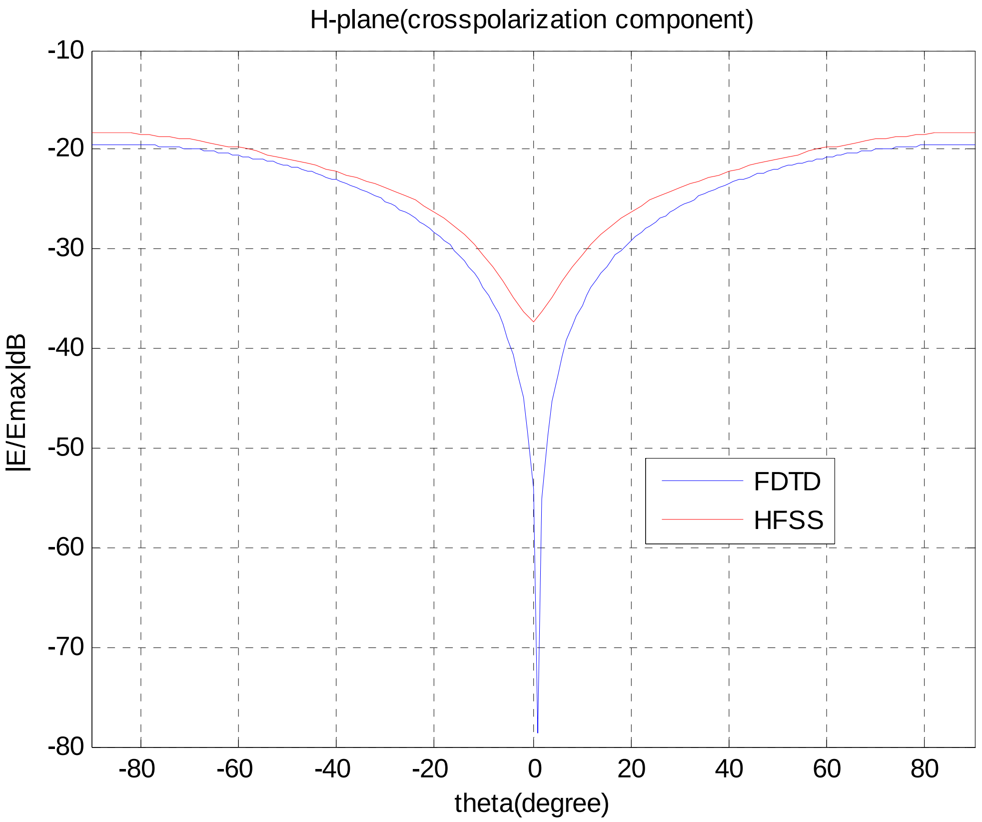

(d)

g.3.30 E-plane and H-plane of Z-Berber patch antenna at at $f_r = 16.25GHz$

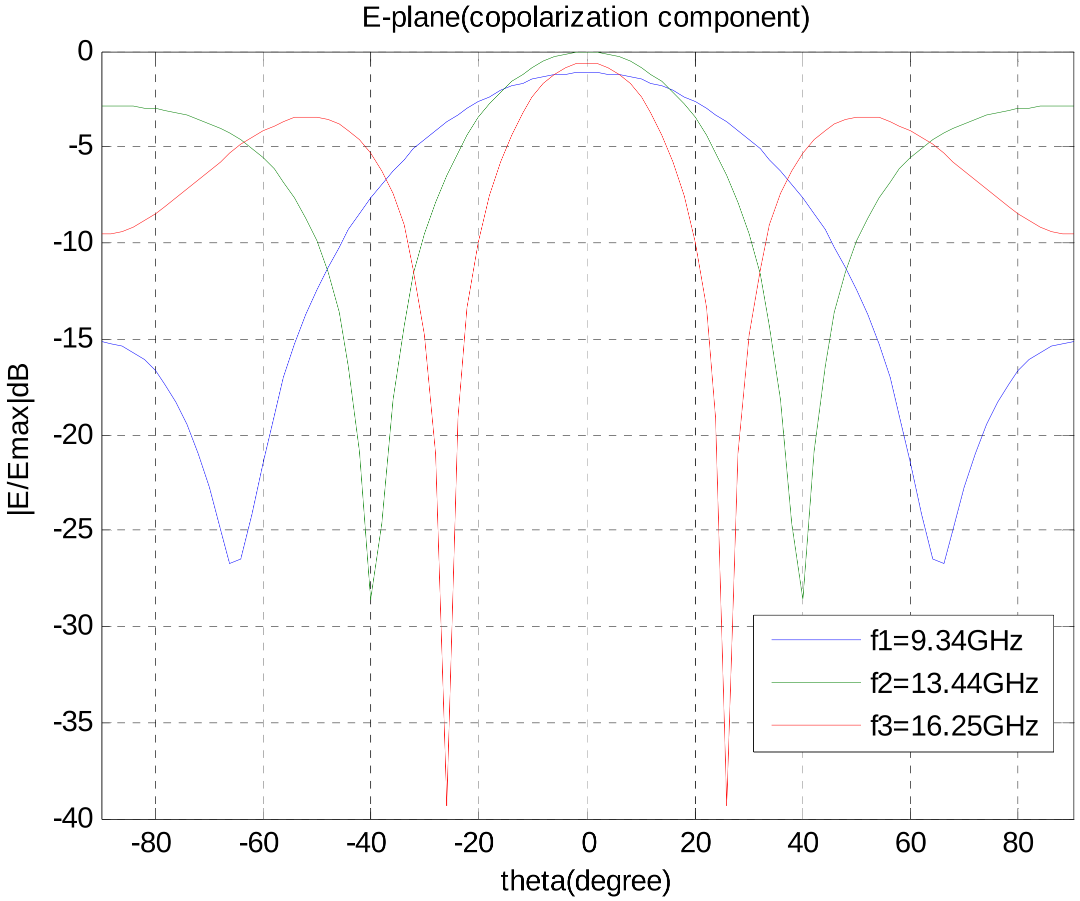

Fig.3.31 The E-plane (co- polarization) at three frequencies of Berber-Z patch antenna

Figure 3.32 shows the total directivity of the Berber-Z antenna at the three frequencies using HFSS simulator and infinite ground plane assumption. At $f_r = 9.34GHz$, the pattern has a main lobe and two side lobes for $\emptyset = 90°$; the main lobe is broaden for first frequency and the broadening decreases at the two other frequencies and, side lobe is narrower than those at the two other frequencies. For $\emptyset = 0°$, the main lobe is broaden when working at the first frequency ($f_r = 9.34GHz$) and the broadening decreases when considering the frequencies $f_r = 13.44GHz$ and $f_r = 13.44GHz$.

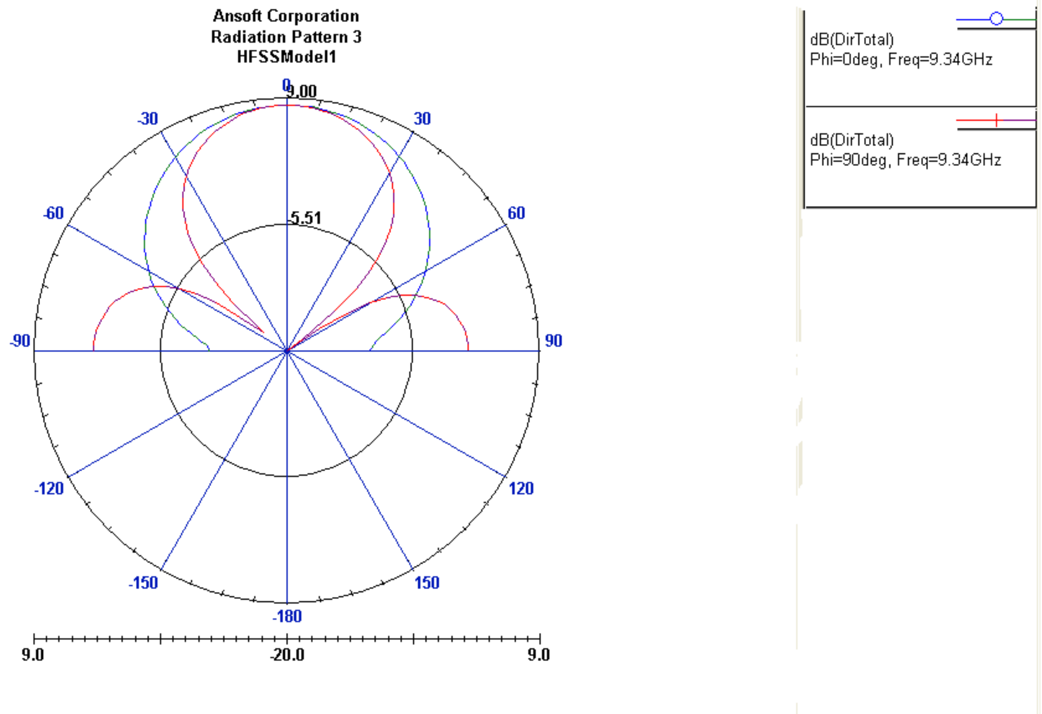

At $f_r = 9.34GHz$

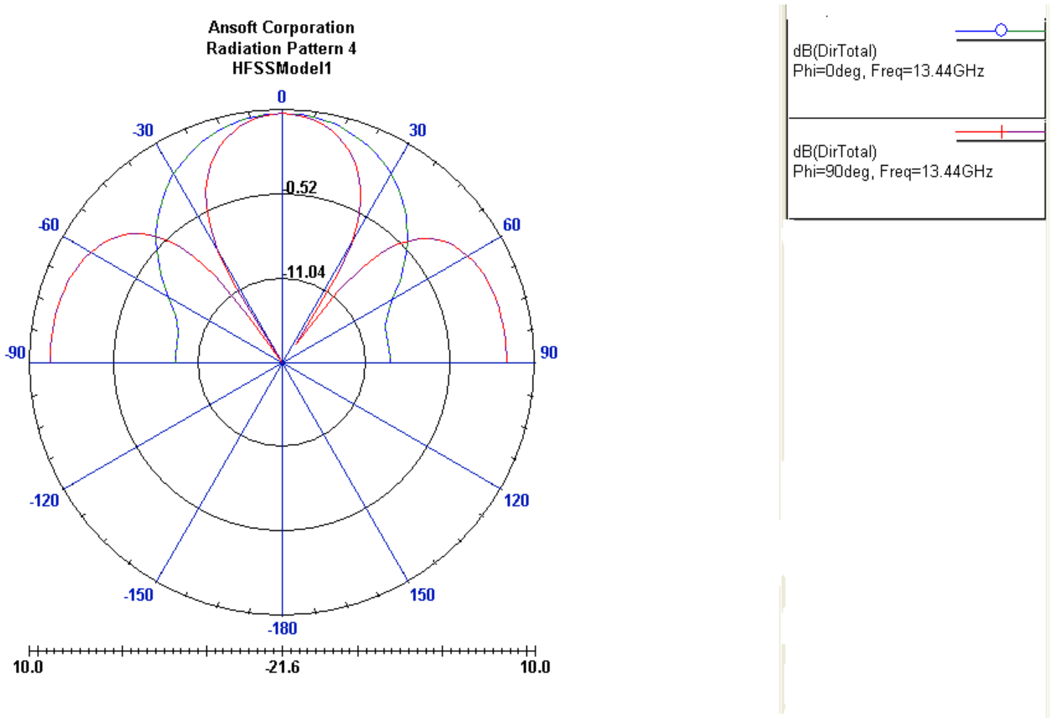

At $f_r = 13.44GHz$

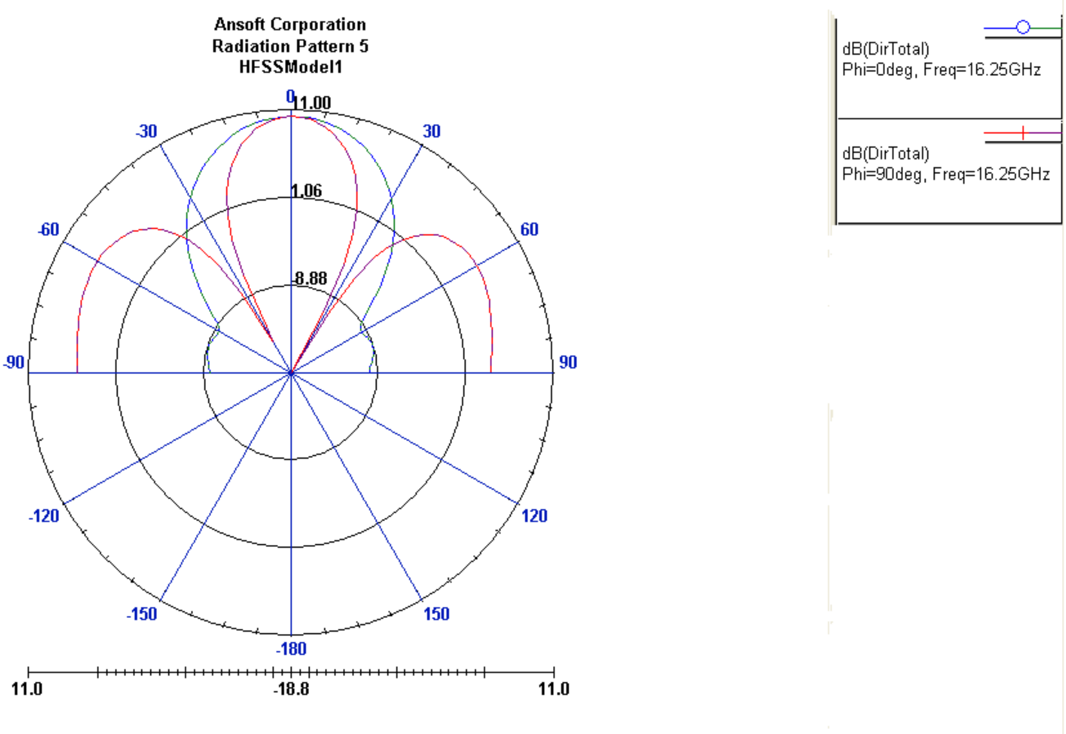

At $f_r = 16.25GHz$

Fig 3.32 The total directivity of Berber-Z patch antenna

Conclusion

In this work, microstrip patch antenna structures are analyzed and designed using the Finite-Difference Time-Domain (FDTD) Method. This method is used in this work because it is an efficient and relatively new method in electromagnetic compared to other conventional methods. Further, this method presents significant advantages which are mainly:

- Simplicity in concept and coding
- Can be used for the analysis of structures with of arbitrary geometries and boundary conditions and no matter on the material isotropy and feeding technique.
- No frequency limitation so that it can predict structure characteristics for an unlimited range of frequency.

Various microstrip antennas shapes with different feeding techniques are investigated in this work including: line fed rectangular antenna, line fed annular-ring, probe fed semi-ring antenna and a combination of a rectangular (dipole) and two semi-ring patches to form a probe fed new patch antenna having the Berber-Z shape.

The Return loss, the input impedance, the Standing wave Ratio, the Radiation pattern, and the total gain of the considered are obtained for each considered structure. The obtained results with the used method are in good agreement with those obtained with HFSS simulator.

Furthermore, the obtained characteristics of the considered antenna shapes – annular-ring, semi-ring and rectangular -obtained using this method verify the predicted ones which are largely reported by literature. These characteristics may be summarized as linear polarization and its purity, single resonant frequency, bandwidth etc.

Its may be noticed the large bandwidths that are associated with the isolated patches is simply due to the fact that the substrate thickness is relatively high. This practically reduces the overall gain of the antennas and, of course, the losses in terms of surface waves should not be ignored.

The analysis using FDTD method is further extended to design a new configuration obtained by combining two semi rings and dipole patches. The proposed form is named Berber-Z patch antenna.

The results obtained with the proposed structure show clearly the *tri-frequency* behavior of the Berber-Z antenna. It has been verified that the radiation at the three frequencies are comparable in terms of power and shapes of the patterns. The only problem that is to mention is the relative level of the lateral lobes which are little bit high. These results are also verified by simulation with the HFSS.

From the presented sample results, the FDTD method proves to be a very flexible and powerful simulation tool not only for the analysis and design of this class of antennas but also for many other practical applications. This work does not cover all the details of the FDTD technique, but concentrates on the main topics related to the analysis and the design of patch antennas.

As a further work, the optimization of the physical dimensions of the Berber-Z antenna may be done to reduce the secondary lobes and to increase the radiation efficiency at the relevant frequencies. Furthermore, the proposed shape for the Berber-Z may be modified by adding another dipole that crosses the main one and drawing to the center the two semi-rings. The new form may have more interesting properties. Also, the proposed structures may be analyzed in the neighborhood of the practical frequencies to study their practical uses.

References

[1]. R. Garg, P. Bhartia, I. Bahl, A.Ittipiboon, “Microstrip Antenna Design Handbook “, Artech House, INC, 2000.

[2]. J. James, P.S. Hall,” Handbook microstrip antenna”, Peter Peregrinus, London, UK, 1989.

[3]. Ehsan G. Doust,”An aperture - Coupled Stacked Microstrip Antenna for GPS Frequency Bands L1, L2 and L5”, master thesis, Carleton University, Dept. of Electronics canada, august 2007.

[4]. Constantine, A.balanis,”Antenna Theory: Analysis and Design “, 2nd edition, John Wiley & Sons, Inc, 1997.

[5].Chin Liong Yeo,”Active microstrip array antenna”, master thesis, University of Queensland, October, 2000.

[6].Dr R.B.Waterhouse,”Microstrip patch antennas, a designer’s guide”, by: RMIT University, Kluwer Academic Publishers, 2003.

[7]. Lal Chand Godara, “Handbook of Antennas in Wireless Communications”, CRC Press; 1 edition (August 16, 2001).

[8].Girish Kumar K. P. Ray,” Broadband Microstrip Antennas”: Artech House, **INC**, 2003.

[9]. Stutzman, W. L. and Thiele, G. A.,”Antenna Theory and Design” 2nd edition, John Wiley

& Sons Inc. 1998.

[10]. KAI FONG LEE, WE1 CHEN, “Advances in Microstrip and Printed Antennas”, John Wiley & Sons, INC.1997.

[11]. Yu, Zbu and Andreas Cangellaris,”Multigrain finite element methods for electromagnetic field modeling”, IEEE Press Series on Electromagnetic Wave Theory ,2006.

[12]. A. Taflove and S. C. Hagness, ‘Computational Electrodynamics: The Finite-Difference Time-Domain Method ‘, 2nd ed. Artech House, 2000.

[13]. Atef Elsherbeni and Veysel Demir, “The Finite Difference Time Domain Method for Electromagnetics: With MATLAB Simulations”, SciTech Publishing, Inc, chapter expert, 2009.

[14].Jaakko juntunen,“Selected developments in computational electrotromagnetics for radio engineering”, phd thesis , Helsinki University of Technology ,may 2001.

[15]. Seppo Aukusti Saario.,” FDTD modelling for wireless communications: antenna and materials”, by master thesis, Griffith university, september, 2002

[16]. Yuyuan Lu, “Novel low loss microwave & millimetre-wave planar transmission lines”, master thesis, University of Manitoba Winnipeg, Manitoba, Canada, 1999.

[17]. A. Reinek and B. Jecko,"Analysis of Microstrip Patch Antennas Using Finite Difference Time Domain Method”, IEEE Transactions on Antennas & Propagation, vol. 3730. 11,pp. 1361-1369,Nov. 2989

[18]. D. M. Sheen, S. M. Ali, M. D. Abouzahra and J. A. Kong , "Application of the Three-Dimensional Finite-Difference Tirne-Domain Method to the Analysis of Planar Microstrip Circuits", *IEEE* Transactions on Microwave Theory & Techniques,vol. 38, No. 7, pp. 849-857, July 1990

[19]. Henrique Manuel Lindgr´en Amaral Fernandes “Development of Software for Antenna Analysis and Design using FDTD”; university of Lisboa,September 2007

[20]. Bharatha Yajaman,B.E ,“FDTD modeling of RF and microwave circuits with active and lumped components”. Master thesis. University of Texas,2004

[21]. “user’s guide-High Frequency Structure Simulator(HFSS)”, Ansoft Corporation,2005.

[22]. Adrian Muscat; “The Design of Low Gain, Wideband and Multi-band Antennas Employing Optimisation Techniques”; Queen Mary University of London, PhD thesis, August 2001

[23]. Paul Wang, “Analysis of Planar Antennas using FDTD”, master thesis, University of Toronto,Canada,1997.

[24]. C. A. Balanis, “Advanced Engineering Electromagnetics”. John Wiley & Sons, 1989.

[25].AZRAR.A.course handout of “antennas and propagation”; dept.of electrical and Electronics Engineering ,university of boumerdes;Algeria.

[26]. AZRAR.A, “Full-Wave Analysis of Microstrip Antennas Employing Coplanar Parasitic elements Based on Moment Method Solution in Spectral Domain”.university of boumerde, June 1998

[27]. S. Gao, J. Li, “FDTD analysis of a sized-reduced, dual-frequency patch antenna”, Progress In Electromagnetics Research, PIER 23, 59–77, 1999

[28]. Elena Semouchkina, Wenwu Cao, and Raj Mittra3, “Modeling of microwave ring resonators using the finite-difference time-domaine method (FDTD)”, microwave and optical technology letters/vol.24,no.6,march 20 200.

[29]. S.-C. Gao, L.-W. Li, M.-S. Leong, and T.-S. Yeo “Analysis of an H-shaped patch antenna by using the FDTD method”, Progress In Electromagnetics Research, PIER 34, 165–187, 2001

[30]. Ansoft HFSS^{TM} v9.2 user guide, available at: www.ansoft.com.

[31]. Ansoft HFSS^{TM} v11 user guide, available at: www.ansoft.com.

Appendix A

Annular-ring microstrip patch antenna

1 .Introduction:

Ring microstrip antennas of various shapes, such as annular, rectangular, square, and triangular, have been studied as alternatives to standard rectangular and circular disk. These antennas are geometrically an intermediate configuration between a printed loop and a patch. Several interesting properties are associated with ring antennas. The primary advantage over other MSA geometries is that for operation at a given frequency in the fundamental mode, the annular ring antenna will occupy the smallest physical area. This characteristic makes the annular ring very attractive as the element for MSA arrays.

The annular ring has been analyzed extensively using the cavity model, generalized transmission line model, analysis in the Fourier- hankel transform domain, and the method of matched asymptotic expansion. The cavity model analysis which is found to be simple and useful in the design for the structure.

2. Fields and currents:

Consider a circular ring microstrip antenna with the coordinate system as shown in fig 1

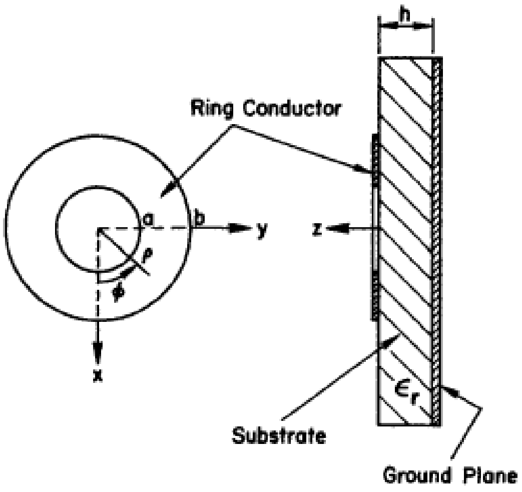

Fig 1: geometry of a circular ring microstrip antenna

It comprises a ring-shaped conductor on one side of a dielectric substrate with a round plane on the other side. The cavity model of the ring is obtained by replacing its peripheries with magnetic walls. Because there is no variation of the fields along the z direction for thin substrates, the modes are designed as TM_{mn} modes [1].

The general solution for the wave equation (1) in cylindrical coordinates is given as

$$\left(\nabla^2 + k^2\right)\vec{E} = 0 \qquad k = 2\pi\sqrt{\varepsilon_r}\,/\,\lambda_o \tag{A.1}$$

We have:

$$E_z = E_0[J_n(k\rho)Y^{'}(ka) - J_n^{'}(ka)Y_n(k\rho)]\cos n\phi \tag{A.2}$$

$$H_\rho = \frac{j}{\varpi\mu\rho}\frac{\partial E_z}{\partial\phi},\; H_\phi = -\frac{j}{\omega\mu}\frac{\partial E_z}{\partial\rho} \tag{A.3}$$

Where $J_n(.)$ and $Y_n(.)$ are the Bessel function of the first and second kind, and of order n, respectively. The other field components are zero inside the cavity. The surface current on the lower surface of ring metallization is given by

$$\vec{J}_s = -\hat{z}\times\vec{H} = -\hat{\phi}H_\rho + \hat{\rho}H_\phi \tag{A.4}$$

$$J_\phi = \frac{jnE_0}{\omega\mu\rho}[J_n(k\rho)Y_n^{'}(ka) - J_n^{'}(ka)Y_n(k\rho)]\sin n\,\phi \tag{A.5}$$

$$J_\rho = \frac{-jkE_0}{\omega\mu}[J^{'}{}_n(k\rho)Y_n^{'}(ka) - J_n^{'}(ka)Y_n(k\rho)]\cos n\phi \tag{A.6}$$

The radial component of the surface current must vanish along the edges at $\rho = a$ and ρ=b to satisfy the magnetic wall boundary conditions. This leads to

$$J_\rho(\rho = b) = H_\phi(\rho = b) = 0 \tag{A.7}$$

Application of this boundary condition leads to the well known characteristic equation for the resonant modes:

$$J^{'}{}_n(kb)Y_n^{'}(ka) - J_n^{'}(ka)Y_n(kb) = 0 \tag{A.8}$$

For the given values of a, b, ε_r and n, the frequency is varied and the roots of (A.8) are determined .let us denote these roots by K_{nm} for the resonant TM_{nm} modes and form X_{nm} such that $X_{nm} = K_{nm}$ a

.the integer n denotes the azimuthal variation as per cosnϕ,while the integer m represents the mth zero of (A.8) and denotes the variation of fields across the width of the ring. The model field patterns and current distributions for some of the modes on the microstrip ring are shown in figure 2:

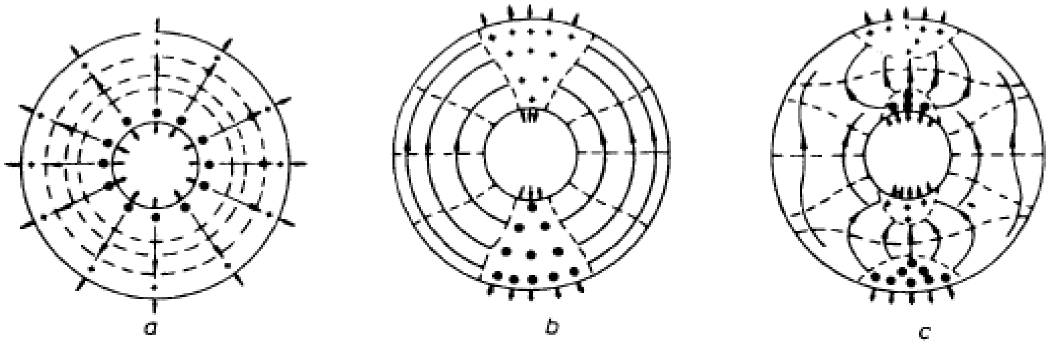

Fig 2: field pattern and current distributions for some of the resonant modes of microstrip ring

For m=1, the field across the strip width is constant. For any given frequency, the mode

corresponding to n=m=1(TM_{11}mode) has the minimum mean radius of the ring, and is known as the dominant mode. This mode is also sustained when a linear full-wave microstrip resonator is bent to form a circular resonator.

The TM_{0m} modes (m even would have no field variation in the ϕ direction, but would vary across the width of the strip; the TM_{0m} mode is the lowest mode of this nature. An approximate value of kn1a can also be obtained using:

$$k_{n/a} = 2an \; /(a + b) \tag{A.9}$$

This expression gives a reasonably accurate value of kn 1 for n≤5 and (b-a)/ (b+a) < 0.35. For more accurate calculations the roots, X_{nm} of the characteristic equation are given in table for b/a=2.

For the general case, the solutions of (A.8) are presented in the form of a mode chart. It can be pointed out that for the microstrip ring antenna, (A.8) should be solved after replacing the radii a and b with their effective values. Calculations of the effective radii terms of physical dimensions are discussed next.

For the case *C* = *2*, the roots of eqn. (3) are given in Table 1

m n	1	2	3	4	5
0	-	3.1966	6.1323	9.4445	12.5812
1	0.6773	3.2825	6.3532	9.4713	12.6012
2	1.3406	3.5313	6.4747	9.5516	12.6612
3	1.9789	3.9201	6.6738	9.6842	12.7607
4	2.5876	4.4182	6.9461	9.8677	12.8989
5	3.1694	1.9929	7.2868	10.1000	13.0750

Table 1: roots of the characteristic equation $J'_n(CX_{nm})Y'_n(X_{nm}) - J'_n(X_{nm})Y'_n(CX_{nm})$ =0, where $C = b/a = 2$ [2]

2.1. Resonant frequency:

Several numerical techniques have been used for calculating the resonant frequencies of the circular ring. Approximate value of the resonant frequency can be obtained by the following approaches used for other patch antennas. To the zeroth-order approximation, the resonant frequency is obtained by setting

$$k = X_{nm}/a \qquad\qquad f_{nm} = \frac{X_{nm}c}{2\pi\sqrt{\varepsilon_r}} \tag{A.10}$$

c is the velocity of light in free space. So far the effect of fringing fields has not been accounted for. As a result, the frequency calculated using (3.10) is lower than the measured value. The accuracy can be improved if the effective dielectric constant ε_{re} is used in place of ε_r in (3.10) that is:

$$f_{nm} = \frac{X_{nm}c}{2\pi\sqrt{\varepsilon_{re}}} \tag{A.11}$$

To determine the value of ε_{re}, the ring resonator is modelled as a microstrip line bent in a circular shape. the effect of curvature on the resonant frequency is expected to be small provided the radius of curvature is large compared with ring can be taken to be the same as that of an equivalent microstrip line with strip width equal to W=b-a.

A parallel plate model of circular ring is shown in fig (3).in this model, the microstrip line is replaced by an equivalent parallel plate waveguide with identical ε_{re} and Z_0 .the parallel plate ring resonator is assumed to have the same arithmetic mean radius as the microstrip ring [1]. The modified values of the inner and outer radii are given by

$$a_e = a - (W_e(f) - W)/2 \tag{A.12.a}$$

$$b_e = b + (W_e(f) - W)/2 \tag{A.12.b}$$

W_e is the effective width of the ring conductor:

$$W_e(f) = W + \frac{W_e(0) - W}{1 + (f/f_p)^2} \tag{A.13}$$

$$W_e(0) = 120\pi / Z_0\sqrt{\varepsilon_e} \tag{A.14}$$

a pair of empirical formulas for the modified radii is given below:

$$a \quad = a - 3h/4 \qquad\qquad b_e = b + 3h/4 \tag{A.15}$$

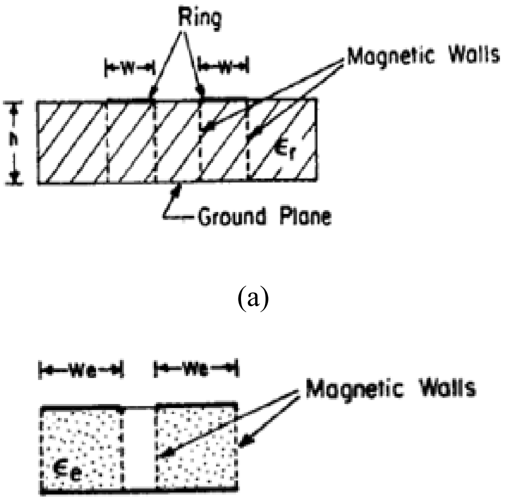

(a)

(b)

Fig3: parallel plate model of a microstrip ring, (a) cross section view of microstrip line and (b) parallel plate model of a part (a)

2.2. Effective Permittivity:

To account for the fringing field which exists outside of the dielectric the concept of an effective permittivity is utilized. Schneider's formula [4] is given in equation (A.10).This empirical formula was developed to take into account the portion of the fields which exist in the air outside of the dielectric and its use improves the accuracy of the cavity model.

$$\varepsilon_e = \frac{1}{2}(\varepsilon_r + 1) + \frac{1}{2}(\varepsilon_r - 1)(1 + \frac{10t}{W})^{-1/2} \qquad \text{(A.15)}$$

The effective permittivity is used in place of the relative permittivity in equation (A.8).The letter t refers to the thickness of the substrate defined while W is the width of the conductor (b-a).

$$k_{nm} = 2\pi\sqrt{\varepsilon_r} / \lambda_0 \qquad \text{(A.16)}$$

2.3. Radiation fields:

The radiation fields of a circular ring antenna can be either from the magnetic current approach or the electric current distribution on the surface of the ring. We shall use the equivalent magnetic current formulation because of its simplicity. Calculations for the radiation fields of the ring are a straight forward extension of the approach used for the circular disk antenna. The only difference between the two cases is that in a circular ring there are two magnetic current sources compared to one for the circular disk. Radiation fields from the magnetic currents at ρ =a and ρ=b are calculated independently and added vectorially to

obtain the radiation patterns for the ring antenna. The radiation fields due to the magnetic ring source at ρ=a [1]:

$$E_\vartheta^a = j^n \frac{e^{-jk_0 r}}{r} a k_0 h E_{zn}(a) J_n^{'}(k_0 a \sin\theta)\cos n\phi \qquad \text{(A.17)}$$

$$E_\phi^a = -nj^n \frac{e^{-jk_0 r}}{r} a k_0 h E_{zn}(a) \frac{J_n^{'}(k_0 a \sin\theta)}{k_0 a \sin\theta} \sin n\phi \cos\phi \qquad \text{(A.18)}$$

Where for the TM_{nm} mode gives:

$E_{zn}(a) = E_0[J_n(k_{nm}a)Y_n^{'}(k_{nm}a) - J_n^{'}(k_{nm}a)Y_n(k_{nm}a)] = \dfrac{2E_0}{\pi k_{nm} a}$ (Using the wronskian for the Bessel equation)

The effect of ground plane is included in derivations of (A.3) and (A.4), but it has assumed that the magnetic current is constant along g the radial direction .the radiation field due to the current source at ρ=b is obtained by replacing a and b in (A.3) and (A.4) and $E_{zn}(a)$ with $-E_{zn}(b)$. The radiation Patterns for the ring antenna are then given by:

$$E_\theta = j^n \frac{e^{-jk_0 r}}{r} k_0 h\left[aE_{zn}(a)J_n'(k_0 a\sin\theta) - bE_{zn}(b)J_n'(k_0 b\sin\theta)\right]\cos n\phi \tag{A.19}$$

$$E_\phi = -nj^n \frac{e^{-jk_0 r}}{r} k_0 h\left[aE_{zn}(a)\frac{J_n(k_0 a\sin\theta)}{k_0 a\sin\theta} - bE_{zn}(b)\frac{J_n(k_0 b\sin\theta)}{k_0 a\sin\theta}\right]\sin n\phi\cos\theta \tag{A.20}$$

where

$$E_{zn}(b) = E_0[J_n(k_{nm}b)Y_n^{'}(k_{nm}a) - J_n^{'}(k_{nm}a)Y_n(k_{nm}b)] \tag{A.21}$$

Use of the characteristic equation and the property of the wronskian simplifies $E_{zn}(b)$ to

$$E_{zn}(a) = \frac{a}{b}\frac{2E_0}{\pi k_{nm}a}\frac{J_n'(k_{nm}a)}{J_n'(k_{nm}a)} \tag{A.22}$$

Substituting for $E_{zn}(a)$ and $E_{zn}(b)$ in gives:

$$E_\theta = j^n \frac{2E_0}{\pi k_{nm}}\frac{e^{-jk_0 r}}{r} k_0 h\left[J_n'(k_0 a\sin\theta) - \frac{J_n'(k_{nm}a)}{J_n'(k_{nm}b)}J_n'(k_0 b\sin\theta)\right]\cos n\phi \tag{A.23}$$

$$E_\phi = -nj^n \frac{2E_0}{\pi k_{nm}}\frac{e^{-jk_0 r}}{r} k_0 h\left[\frac{J_n(k_0 a\sin\theta)}{k_0 a\sin\theta} - \frac{J_n'(k_{nm}a)}{J_n'(k_{nm}b)}\frac{J_n(k_0 a\sin\theta)}{k_0 a\sin\theta}\right]\cos\theta\sin n\phi \tag{A.24}$$

Where:

$$k_{nm}a = \chi_{nm}$$

3. Input impedance:

Input impedance of a ring antenna can be determined by extending the techniques used for the circular disk. Here we use the cavity model.

Consider a circular ring microstrip antenna fed by a coaxial probe at $\rho = \rho_0$ from the center .the effect of the finite diameter of the probe is included by modelling it as a uniform current ribbon of angular width $2\omega f$. The electric field in the ring cavity due to this excitation is obtained by the superposition of all the cavity modes with appropriate excitation coefficient and is given by:

$$E_z = j\omega\mu_0 I\left\{\sum_{n=0}^{\infty}\sum_{m=1}^{\infty} A_{nm}\left[J_n(k_{nm}\rho)Y_n^{'}(k_{nm}a_e) - J_n^{'}(k_{nm}a_e)Y_n^{'}(k_{nm}\rho)\right]\right\}\cos n\phi \tag{A.25}$$

Where

$$A_{nm} = \frac{k_{nm}^2 \pi \sin(2n\omega f)\cos n\pi\left[J_n(k_{nm}\rho_0)Y_n'(k_{nm}a_e) - J_n'(k_{nm}a_e)Y_n(k_{nm}\rho_0)\right]}{\varepsilon_0 n\left(k^2 - k_{nm}^2\right)\left[\frac{J_n'^2(k_{nm}a_e)}{J_n'^2(k_{nm}b_e)}\left(1 - \frac{n^2}{k_{nm}^2 b_e^2}\right) - \left(1 - \frac{n^2}{k_{nm}^2 a_e^2}\right)\right]} \qquad \text{(A.26)}$$

The input impedance is now calculated by averaging over the feed annular width $2\omega f$ and using the approach of (35) to (40) one obtains

$$Z_{in} = j\omega\mu_0 h\left\{\sum_{n=0}^{\infty}\sum_{m=1}^{\infty} \frac{\pi \mathrm{k}_{\mathrm{nm}}^2 \left(\frac{\sin 2n\omega f}{2n\omega f}\right)^2 \left[J_n(k_{nm}\rho)Y_n'(k_{nm}a_e) - J_n'(k_{nm}a_e)Y_n'(k_{nm}\rho)\right]}{2\varepsilon_{0\mathrm{n}}\left(k_{eff}^2 - k_{nm}^2\right)\left[\frac{J_n'^2(k_{nm}a_e)}{J_n'^2(k_{nm}b_e)}\left(1 - \frac{n^2}{k_{nm}^2 a^2}\right) - \left(1 - \frac{n^2}{k_{nm}^2 b^2}\right)\right]}\right\}\cos^2 n\phi_0$$

(A.26)

Where a_e and b_e are the effective radii defined by (1) and

$$k_{eff} = k_0\sqrt{\varepsilon_{re}\left(1 - j\delta_{eff}\right)} \qquad \text{(A.27)}$$

4. Losses, Q, and resonant resistance:

The dielectric loss, copper loss, radiated power, and total energy stored at resonance are given by the following expressions:

$$P_d = \frac{\omega E_0^2 \varepsilon t\delta}{\pi k_{nm}^2}\left[\frac{J_n'^2(k_{nm}a)}{J_n'^2(k_{nm}b)}\left(1 - \frac{n^2}{k_{nm}^2 b^2}\right) - \left(1 - \frac{n^2}{k_{nm}^2 a^2}\right)\right] \qquad \text{(A.28)}$$

$$P_C = \frac{2}{\pi}R_s\frac{E_0^2}{\omega^2\mu_0^2}\left[\frac{J_n'^2(k_{nm}a)}{J_n'^2(k_{nm}b)}\left(1 - \frac{n^2}{k_{nm}^2 b^2}\right) - \left(1 - \frac{n^2}{k_{nm}^2 a^2}\right)\right] \qquad \text{(A.29)}$$

$$P_r = \frac{2\omega k_0^2 t E_0^2}{\xi_0 k_{nm}^2} I_1 \qquad \text{(A.30)}$$

$$W_T = \frac{E_0^2 \varepsilon t}{4\pi k_{nm}^2}\left[\frac{J_n'^2(k_{nm}a)}{J_n'^2(k_{nm}b)}\left(1 - \frac{n^2}{k_{nm}^2 b^2}\right) - \left(1 - \frac{n^2}{k_{nm}^2 a^2}\right)\right] \qquad \text{(A.31)}$$

$$I_1 = \int_0^{\pi/2} \left[\frac{n^2 \cos^2\theta}{k_0^2 \sin\theta} \left\{ \frac{J_n(k_0 a \sin\theta)}{a} - \frac{J_n(k_0 b \sin\theta)}{b} \frac{J_n'(k_{nm} a)}{J_n'(k_{nm} b)} \right\}^2 + \right. \\ \left. \sin\theta \left\{ J_n'(k_0 a \sin\theta) - J_n'(k_0 b \sin\theta) \frac{J_n'(k_0 a)}{J_n'(k_0 b)} \right\}^2 \right] d\theta \tag{A.32}$$

The effective loss tangent is then given by

$$\delta_{eff} = \tan\delta + \frac{1}{h\sqrt{\sigma\mu_0 \pi f}} + \frac{2\omega\mu_0 h}{\eta_0 \varepsilon_r} I_1 \tag{A.33}$$

$$Q_T = 1/\delta_{eff} \tag{A.34}$$

The radiation resistance a resonance can be calculated as

$$R_r = \frac{V_0^2}{2P_T} \tag{A.35}$$

$$P_T = P_r + P_c + P_d \tag{A.36}$$

Where V_0 is the voltage at ρ=b, ϕ=0

Appendix B

Calculation resonant frequencies with analytical method

1. Rectangular patch antenna:

The microstrip antenna simulated in chapter 3 is designed to resonate at 7.5GHz .its width is 12.45mm and its length is 16 mm. The substrate used has a dielectric of 2.2 and has a thickness of 1.59mm.the feed width is 2.46 mm, which is design to give a characteristic impedance of 50Ω.

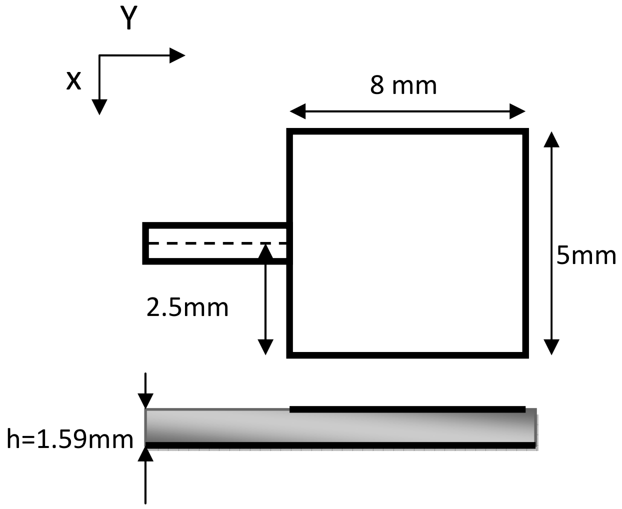

Fig 1: Line fed rectangular patch antenna

$$\varepsilon_{eff} = \frac{\varepsilon_r + 1}{2} + \frac{\varepsilon_r - 1}{2}\left[1 + 12\frac{h}{W}\right]^{\frac{1}{2}}$$

$$\Delta L = 0.412h\frac{(\varepsilon_e + 0.3).(\frac{W}{h} + 0.264)}{(\varepsilon_e - 0.258).(\frac{W}{h} + 0.8)}$$

$$L_{eff} = L + 2\Delta L$$

Calculation of resonance frequency of rectangular patch antenna:

$$f_r = 11.44\text{GHz}$$

2. Annular-ring microstrip patch antenna:

Consider an annular ring patch with outer radius *b* and inner radius *a*, as shown in figure 2.

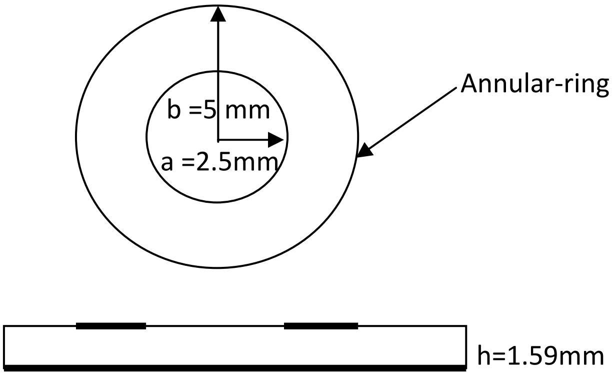

Fig 2.annular-ring patch antenna

The annular-ring microstrip antenna simulated in chapter 3 section 3.2 is designed to resonate at 9.375GHz .its inner radius is 2.5mm and its outer radius is 5 mm. the substrate used has a dielectric of 2.33 and has a thickness of 1.59mm.the feed width is 2.46mm ,which is design to give a characteristic impedance of 50Ω.

$$\varepsilon_{eff} = \frac{\varepsilon_r + 1}{2} + \frac{\varepsilon_r - 1}{2}(1 + \frac{h\,10}{a})^{-1/2}$$

$$f_r = \frac{c\, x_{nm}}{2\, a\, \pi(\varepsilon_{eff})^{1/2}}$$

$$f_r = \frac{3 \times 0.6773}{2\ \times 2.5\ \times \pi(\varepsilon_{eff})^{1/2}} = 9.40GHz$$

3. Semi-ring patch antenna:

The semi-ring patch antenna is shown in figure 3, its inner radius is 3.5mm and its outer radius is 7 mm. the substrate used has a dielectric of 2.2 and has a thickness of 1.59mm.the probe diameter is 2.46mm ,which is design to give a characteristic impedance of 50Ω.

$$f_r = \frac{c\, x_{nm}}{a\, \pi(\varepsilon_{eff})^{1/2}}\text{b}$$

$$f_r = \frac{3 \times .6773}{3.5\,\pi(\varepsilon_{eff})^{1/2}} = 13.56\ GHz$$

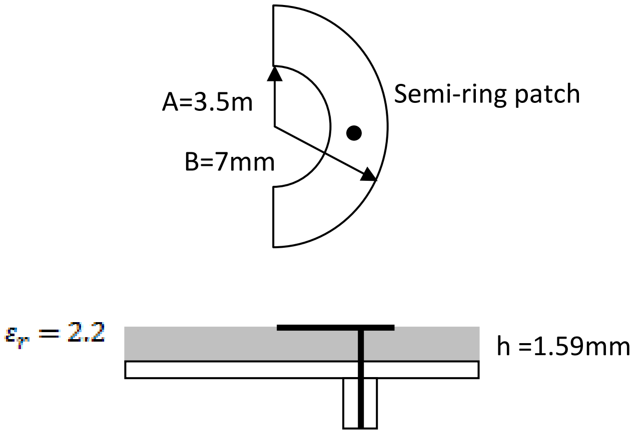

Fig 3.semi-ring patch antenna

Appendix C

Ansoft's high frequency structure simulator (HFSS) antenna Design software

The software used for the designing and simulating the antenna model is High Frequency Simulation Software (HFSS v9.0). This part provides a general insight into the various aspects involved in the process of setting up and running a simulation in HFSS. The version used is Ansoft version 9.0. HFSS is a software package for electromagnetic modeling and analysis of passive, three dimensional structures. In order to calculate the full three-dimensional electromagnetic field inside a structure and the corresponding S-parameters, HFSS employs the finite element method (FEM) [47].

FEM is a powerful tool for solving complex engineering problems, the mathematical formulation of which is not only challenging but also tedious. The basic approach is to divide a complex structure into smaller sections of finite dimensions known as elements. These elements are connected to each other via joints called nodes. Each unique element is then solved independently of the others thereby drastically reducing the solution complexity. The final solution is then computed by reconnecting all the elements and combining their solutions. These processes are named assembly and solution, respectively in the FEM [57]. FEM finds applications not only in electromagnetic but also in other branches of engineering such as plane stress problems in mechanical engineering, vehicle aerodynamics and heat transfer.

FEM is the basis of simulation in HFSS. HFSS divides the geometric model into a large number of tetrahedral elements. Each tetrahedron is composed of four equilateral triangles and the collection of tetrahedron forms what is known as the finite element mesh. Each vertex of the tetrahedron is the place where components of the field tangential to the three edges meeting at the vertex are stored. The stored component is the vector field at the midpoint of the selected edges, which is also tangential to a face and normal to the edge. Using these stored values, the vector field quantity such as the H-field or the E-field inside each tetrahedron is estimated. A first-order tangential element basis function is used for performing the interpolation. Maxwell's equations are then formulated from the field quantities and are later transformed into matrix equations that can be solved using the traditional numerical techniques [57].

PROCESS OVERVIEW

The first step is to draw the geometric model of the structure that is to be realized. The next step is to select the materials that the various drawn objects are made of. An accurate definition of boundaries for the structure, such as perfect electric, radiation etc, follows next.

In HFSS, a port or a voltage source needs to be defined to excite the structure. This is done as part of the excitation definition. Once the structure is completely modeled the solution is set up. This includes definition of various parameters such as the frequency at which the adaptive mesh refinement takes place and the convergence criterion. Finally, after the completion of the simulation, the solution data is post processed which may include display of far-field plots, plots and tables of S-parameters, smith chart graphs etc. the figure below is summarized flow-chart depiction of the above mentioned theory.

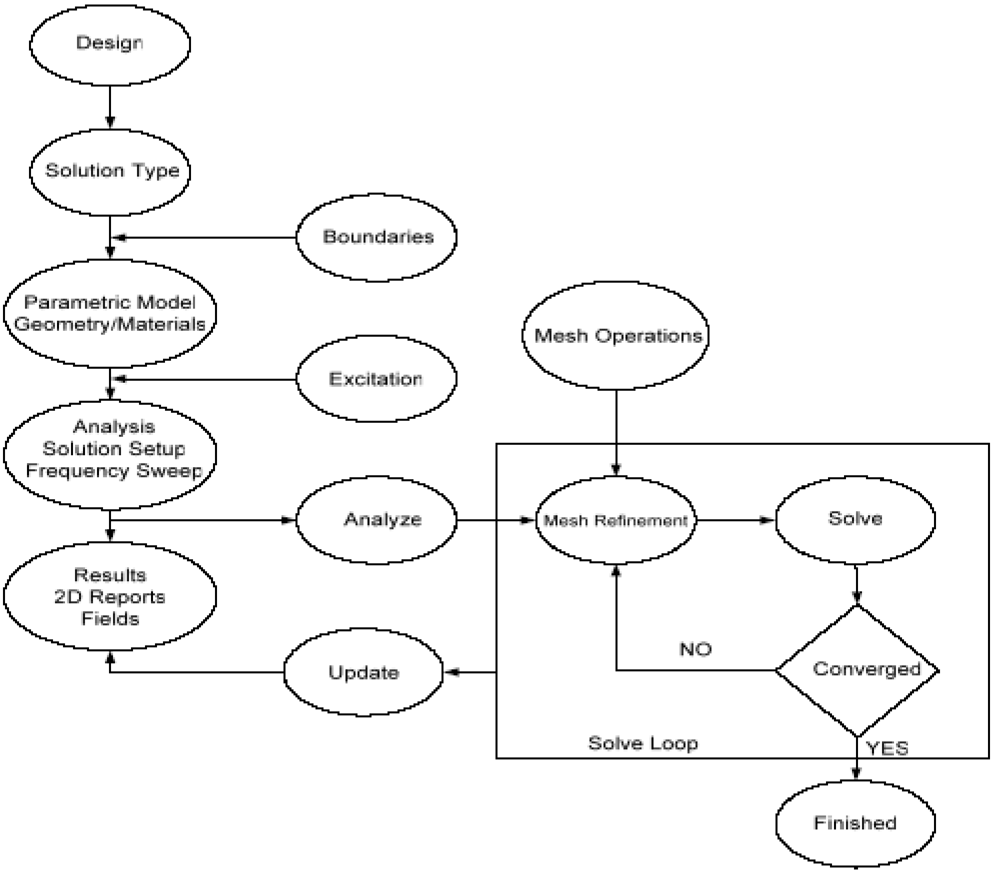

Fig 1: Process overview flow chart of the HFSS v9.0 Simulation module [47].